
Characterization of Fluorophores for Two-Photon and STED Microscopy in Tissue

MASTER'S THESIS
MSc IN NANOBIOSCIENCE AND INTERDISCIPLINARY SCIENCE STUDIES

Authored by
BJARNE THORSTED*

SUPERVISOR

Jonathan R. Brewer

Memphys - Center for Biomembrane Physics
Department of Physics, Chemistry & Pharmacy
University of Southern Denmark



February 2015

*bjtho08@student.sdu.dk

Abstract

Two-Photon Excitation Microscopy (TPEM) uses high-intensity long-wavelength laser light to excite fluorophores and provide resolution comparable to confocal microscopy with an inherent optical sectioning and deep tissue imaging ability. Stimulated Emission Depletion (STED) use a deexcitation laser to reduce the area of excited fluorophores, which practically results in an increased resolution of down to 20 nm. These two microscopy techniques have a large potential if combined, because of their individual advantages. Characterizing fluorophores for use in these systems is therefore of great interest to the scientific community. In this thesis, I present the results of my efforts to successfully build a two-photon spectrofluorometer capable of automatic acquisition of spectral data of commercial and novel dyes, in the form of two-photon absorption cross sections. I also show that it is possible to use the two commercial dyes Abberior Star 440SX and Abberior Star 488 to image specimens in TPEM by exciting them at 860 nm and 1010 nm, respectively. I elaborate on the suitability of the dyes in regards to TPEM and provide data from *in situ* experiments with some of the dyes in human skin tissue imaged by confocal, TPE and STED microscopy that support earlier reports of the spatial differentiation between two proteins, claudin-1 and desmoglein-1, involved in maintaining the skin barrier, showing that claudin-1 is virtually non-present in the stratum corneum and mainly located in the stratum granulosum, whereas desmoglein-1 is found throughout the epidermis.

Acknowledgments

This project has been part of my everyday life for more than a year now. Through the ups and downs, I have always been deeply grateful for the opportunity to work on this project, which has given me so many great experiences. My supervisor, Jonathan Brewer, has been both a mentor and a friend to me during this project. I have truly learned a lot from him. He has been invaluable to me in many ways, and I cannot thank him enough for his support and high spirits in even the bleakest of situations.

I would also like to thank Jes Dreier for helping me use the Huygens image software and Till Leißner for helping maintain and improve upon the microscope setup.

To all my friends, I owe a great thanks. I could not have made it through without you. Henrik Thoke, in particular, has always been great at asking the right questions when my own mind got stuck in a rut, and Anne Zebitz has never failed to help me get out of my cave and relax a little on a Saturday night.

Finally, I would like to thank my family for always being supportive of my life decisions, and my lovely niece, Sarah, who means the world to me and to whom I dedicate this work.

Contents

Glossary	vii
1 Introduction	1
2 Theory	5
2.1 Fluorescence	5
2.2 Two-Photon Absorption	8
2.2.1 One-Photon Absorption Cross Section	11
2.2.2 Two-Photon Absorption Cross Section	14
2.3 Stimulated Emission	19
2.4 Confocal Microscopy	20
2.4.1 Optical Resolution	23
2.5 STED Microscopy	25
2.6 Cell Junctions	30
2.6.1 Desmosomes	31
2.6.2 Tight Junctions	32
3 Materials and Methods	33
3.1 Materials	33
3.2 Software and Equipment	35
3.2.1 Automation Scripts	37
autoAOTF.bsh	37
auto.VBS	37
3.3 2-photon Absorption Cross-section Measurements	38
3.3.1 Data Acquisition	38
3.3.2 Data Analysis	39
twopa.m	39
3.4 Sample Preparation	39

3.5	STED Microscopy	40
4	Results and Discussion	41
4.1	Two-Photon Absorption Cross Sections	41
4.2	STED Microscopy	45
4.2.1	Photostability	52
5	Conclusion and Perspective	55
	Bibliography	59
A	Appendix	A-1
A.1	Mowiol Recipe	A-1
B	2PA Cross Sectional Data	B-1
C	Lab Automation and Matlab Scripts	C-1
C.1	Automation Control for the Equipment	C-1
C.1.1	autoAOTF.bsh	C-1
C.1.2	auto.VBS	C-10
C.1.3	background.VBS	C-12
C.1.4	Free-run.VBS	C-13
C.1.5	settings.VBS	C-14
C.2	MATLAB® Scripts	C-15
C.2.1	concentration.m	C-15
C.2.2	twopa.m	C-16
C.2.3	twopacollect.m	C-23

Glossary

c.c

The complex conjugate of a number or expression. A complex conjugate is identical to its partner except with opposite sign of the imaginary part. The complex conjugate of $z = a + ib$ is $\bar{z} = a - ib$

CLSM

Confocal Laser Scanning Microscope.

Dirac delta function

A function defined such that it is has a value of zero at all point except zero, and the area under the line is equal to 1. It is mathematically defined as

$$\delta(x) = \begin{cases} \infty & \text{if } x = 0 \\ 0 & \text{if } x \neq 0 \end{cases} \quad \int_{-\infty}^{\infty} \delta(x) = 1.$$

It is related to the Kronecker delta.

\hbar

The reduced Plank's constant, equal to Planck's constant h divided by 2π , or $1.054571726(47) \times 10^{-34}$ Js

i

The imaginary unit, defined such that $i^2 = -1$. Complex numbers have a real and imaginary part and can be represented in the complex plane as a number $z = a + ib$, where a is the real part and b is the imaginary part with the unit i

Kronecker delta

Is a function of two (or more) variables. If the variables are equal, the function is 1 and otherwise 0. Mathematically, this is expressed as

$$\delta_{ij} = \begin{cases} 1 & \text{if } i = j \\ 0 & \text{if } i \neq j \end{cases}.$$

An identity matrix has the same properties as the Kronecker delta

 λ

- 1) The wavelength of light, usually measured in nanometer (nm).
- 2) An expansion parameter used in perturbation theory.

NA

Numerical aperture of a lens or objective. It is defined as $NA = n \sin \alpha$, where n is the refractive index and α is the angular aperture

NIR

Near-infrared; a range in the electromagnetic field starting at 700 nm and extending up to about 1400 nm, depending on the standard definition used

 ν

Frequency of a photon. Often used to denote the energy since this is proportional to the frequency by $E = h\nu$.

 ω

Angular frequency.

Point spread function

A response function, that describes the spatial distribution of light from a point-like source or object. The ideal description being an Airy function

 \vec{r}

The position vector of an object. In a cartesian coordinate system, the vector consists of the three scalars (x, y, z) .

 $\sigma_{if}^{(N)}$

The Nth order absorption cross section of a material from state i to f . The order indicates the number of simultaneous photons involved in the absorption process

STED

A technique for resolving objects smaller than the diffraction limit typically allows for..

t

A variable denoting time.

TEM

Transmission Electron Microscopy.

TPE

Two-Photon Excitation.

TPEM

Two-Photon Excitation Microscopy.

CHAPTER 1

Introduction

Bioimaging has been a fundamental tool for several decades in the fields of histology, and cell and molecular biology. Especially, the ability to do specific labeling and imaging of different proteins, membranes, and organelles with the fluorescence-based microscopy technique has advanced the knowledge in these fields tremendously [1].

Optical microscopy has enjoyed many advances since its invention. Fluorescence microscopy enabled researches to view specific structures and proteins that are normally not visible with plain white light by staining samples with anti-body linked fluorophores that selectively adhere to the sample. Confocal fluorescence microscopy greatly enhanced the definition of micrographs, by filtering out-of-focus light from the sample, albeit at the expense of contrast [2]. This was a small sacrifice, though, since researchers were now able to precisely control in which particular depth they wanted to examine their samples by moving the focal plane up and down in the sample. This also made it possible to build 3D models of the samples by combining images taken at various depths, giving easier access to spatial information.

Two-Photon Excitation (TPE) is similar to confocal microscopy, in that both have an inherent ability to image only limited sections of the sample in the plane of focus, enabling researchers to create 3D images of the samples. Where the latter rely on insertion of pinholes in the light path to control the light entering and leaving the sample, the former uses the physical properties of a material response to high intensity laser light [3]. Two-Photon Excitation Microscopy (TPEM) utilize longer wavelength light to excite the fluorophores in a sample, which results in a decrease in resolution, but offers other advantages to make up for it. Because thick tissue samples scatters light more than a thin cell culture sample, the high intensity light used in TPEM generally provides better contrast than does its confocal counterpart. TPEM also offers superior depth penetration over confocal microscopy, in part because the longer wavelengths are less prone to scattering in biological tissue, but

also because of the high intensity used to illuminate the sample. Where confocal microscopy is ineffective beyond a few hundred micrometers, its two-photon cousin can image up to one millimeter into a sample [4].

Optical microscopy, the main pillar of fluorescence-based imaging, has always been limited by the diffraction of light. The lowest theoretical limit being around 200 nm [5] is quite low compared to the size of the intracellular constituents typically investigated. Several emerging techniques, that promise to alleviate this constraint [6–9], are actively being developed, and in 2014 the Nobel prize in chemistry was awarded to the developers of super-resolution fluorescence microscopy.

Stimulated Emission Depletion (STED) microscopy builds upon the technology used in confocal (or TPE) microscopy. A deactivating laser is used in conjunction with the primary illuminating laser source of the microscope to reduce the area from which fluorophores occurs [9]. This allows for much higher resolution imaging, enabling researchers to image ultrastructural features of the samples which were previously out of reach when relying on optical microscopy. Like confocal microscopy suffered a decrease in contrast because of the filtering of light, so does STED also result in a lower contrast and signal to noise ratio. This can be compensated by either using fluorophores with a higher quantum yield or by increasing the output of the illuminating laser source. The latter increases the risk of bleaching the samples while the former is not always a possibility since the quantum yield has an upper theoretical limit of 1 and many dyes are already around 0.8 to 0.9 and above.

The combination of TPEM and STED, although still rare, will require a wider range of suited fluorophores to choose from. Therefore, the need for reliable characterization of newly developed, as well as already commercialized, fluorophores will become increasingly important [10]. This is also the case for testing the fluorophores *in situ*, because their physical properties can be significantly dependent on both their surroundings [11], and upon whether or not they are covalently linked to other molecules.

The human skin has the very important function of forming a barrier that separates the inside from the outside and prevents foreign substances, such as pathogens, from entering the body, and protects it against mechanical stress as well as loss of water through evaporation. This function is maintained by a group of multi-protein complexes known as tight junctions [12]. These complexes stitch the cells together in layered sheets that form a very effective barrier capable of restricting paracellular diffusion of potentially dangerous particles while still allowing selective passage of other molecules. Stratum corneum, the outermost layer of the skin, consists of thin sheets of flattened, keratinized, and denucleated cells called corneocytes. Several proteins involved in maintaining the cell-cell contacts in the human epidermis have been identified, such as occludin and several cadherins and claudins [13–15]. Deficiencies of either of these proteins show abnormalities in the formation of tight junctions that are linked to several skin-related diseases [16], and abnormal distribution of these tight junction proteins have been observed in diseases such as ichthyosis vulgaris, lichen planus, and psoriasis vulgaris [17, 18]. Gaining a deeper

understanding of the dynamics involved in the forming of the epidermal barrier could potentially lead to effective treatments for several skin-related diseases.

My thesis is focused primarily on two specific optical microscopy techniques, TPE, and STED microscopy, both of which are dependent on the samples under investigation being fluorescent. Since TPE fluorescence has a more complex interaction with the fluorophores than does regular fluorescence, it is important to understand how well they respond in TPEM. Two-photon absorption cross section spectra gives researchers the opportunity to find the best suited fluorophores as well as the optimal excitation wavelength for the specific fluorophores, but this type of information is scarce and often the researchers themselves will have to approximate these spectra beforehand [19].

To prepare for these requirements, a large part of my thesis revolved around constructing a system that could acquire TPE fluorescence spectra more or less autonomously, and put together the analytical tools necessary for calculating the two-photon absorption cross section spectra. This enabled me to characterize the efficacy of commercial and newly developed novel fluorophores. Where feasible, the dyes were also tested *in situ* using TPEM and STED microscopy for the purpose of imaging biological tissue samples and to ascertain the efficacy of the dyes in tissue. In particular, the spectral separation and photostability of fluorophores in comparison with confocal microscopy are of great importance in this regard because it is often necessary to view how different proteins, such as those found in the epidermal cell junctions, are co-localized which is only possible using several spectrally distinct dyes that do not bleach before proper image acquisition has completed.

This document represents the culmination of my Master's thesis, and it has been written so as to display the different aspects of the work I have done over this past year or so. Chapter 2 will present all the theory needed to understand the work presented herein starting with a brief introduction to fluorescence before moving on to one- and two-photon absorption, stimulated emission, and confocal and STED microscopy before rounding off with an overview of cell junctions. Chapter 3 will proceed to inform the reader about the materials and equipment used throughout this thesis as well as delve into some of the more technical aspects of assembling the setups used and the code needed. It will also provide the reader with the necessary protocols to re-create my work. The purpose of Chapter 4 is to give a thorough presentation of the results I have gathered in my work on this project as well as what these results mean and indicates. Finally, Chapter 5 will conclude my work by reiterating the most important conclusions that could be drawn from my results as well as give the reader an outlook to what future projects could become of my work.

CHAPTER 2

Theory

In this chapter, I will discuss the various topics relating to this thesis: fluorescence, one- and two-photon absorption, stimulated emission, optical resolution, and confocal and STED microscopy as well as some of the proteins involved in maintaining the skin barrier.

The two main subjects, two-photon absorption and stimulated emission, including STED microscopy, will make up the main part of this chapter. The sections about fluorescence, resolution, and confocal microscopy will provide an introduction to these fields while the section about cell junctions is meant to give a brief overview of the subject.

2.1 Fluorescence

All the fifty years of conscious brooding have brought me no closer to answer the question, “What are light quanta?” Of course today every rascal thinks he knows the answer, but he is deluding himself.

Albert Einstein (1951)

Light is the principal source of information for most humans. Everything we see is due to light interacting with objects around us before entering our eyes and being interpreted by our brain to form images that we can analyze and respond to.

On the smallest scale possible, light can be described as small energy “packets”, or quanta, called photons. A photon is a massless elementary particle with zero electrical charge and described by its polarization and its wave vector which specifies the wavelength and direction of propagation of the photon.

When a photon with energy ν hits an atom or molecule an interaction between the two will occur. Fundamentally, there are four types of interactions between light and matter: reflection, refraction, absorption, and emission. Depending on the properties of the molecule and photon, one or more of these interactions are

possible. In Figure 2.1 a few examples of absorption interactions between photons and matter are presented. Rayleigh and Raman scattering are examples of inelastic (emitted photon is identical to absorbed) and elastic scattering (energy of emitted photon is not equal to that of absorbed), respectively. Second-harmonic generation (SHG) is a frequency-doubling phenomena where two identical photons are “combined” to form a new photon with twice the energy and half the wavelength.

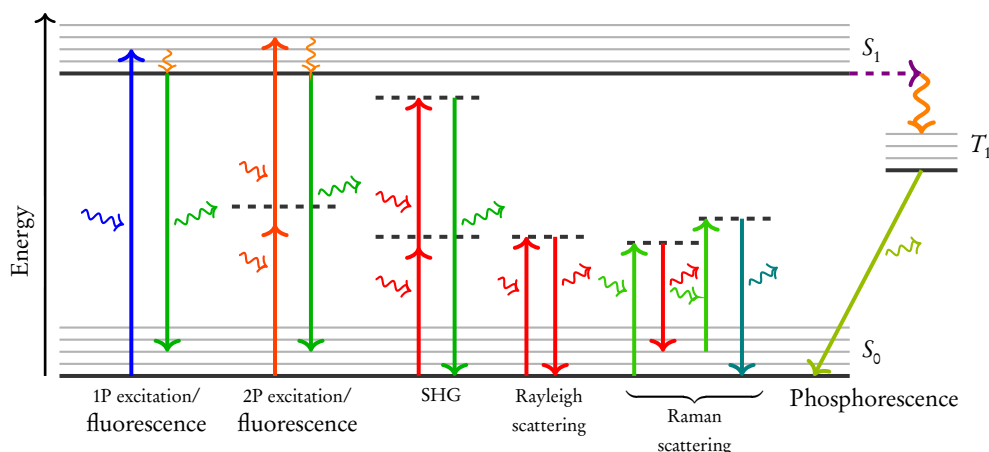


Figure 2.1: Jablonski diagram of different photon-matter interactions. Downwards slanting wavy arrows are absorbed photons; upwards slanting wavy arrows are emitted photons. Dashed lines signify virtual states. Gray lines are vibronic levels of the electronic state.

One- and two-photon excitation fluorescence are processes in which one (or two) photon(s) is/are absorbed by the molecule, exciting one of its valence electrons from a lower state (often the ground state S_0) to a higher electronic state. This is usually the first excited electronic state S_1 .

In most cases, this is not a stable state for the electron to be in. Therefore it will follow one of a number of different energetic pathways to return itself to its ground state (see Figure 2.2):

- Vibronic relaxation (non-radiative; lifetime: $10^{-14} - 10^{-13}$ s [20])
- Internal conversion (non-radiative; lifetime: $\sim 10^{-12}$ s [21])
- Intersystem crossing (non-radiative; lifetime: $10^{-8} - 10^{-6}$ s [22])
- Fluorescence (radiative; lifetime: $10^9 - 10^8$ s [20])
- Phosphorescence (radiative; lifetime: $10^{-3} - 10^1$ s [20])

If the absorbed photon carries enough energy, the electron will be excited up to one of the rovibronic¹ sublevels in the S_2 electronic state. From there, the electron will undergo vibronic relaxation until it arrives at the lowest rovibrational sublevel

¹a ROtational sublevel of a VIBrational level of an electRONIC state

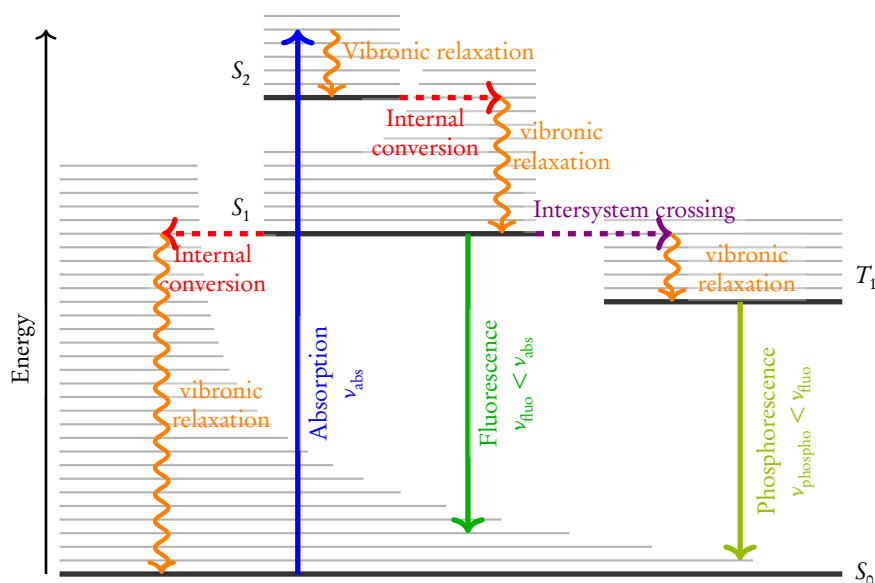


Figure 2.2: Jablonski Diagram showing different conversion pathways for energy obtained through absorption of a single photon. Rovibrational sublevels of the vibrational levels are not shown.

in the S_2 state. Here, it will undergo an internal conversion from the S_2 state to a vibrational state in the S_1 electronic state and relax to the lowest energy level in the S_1 state. During the vibronic relaxations excess energy is released to the system in the form of heat.

If the absorbed photon carries just enough energy to excite an electron to the S_1 , but not the S_2 electronic state, it will not undergo the internal conversion, but still relax down to the lowest energy level in this electronic state.

At the S_1 electronic state, there are three possible outcomes: It can undergo internal conversion yet again and relax back down to its ground state (S_0) thereby releasing the energy to its surroundings in the form of heat; it can undergo intersystem crossing to a "forbidden" state, T_1 ; it can relax to S_0 by interacting with another molecule (a process known as quenching), or; it can decay directly to its ground state by emitting a photon with energy equal to the energy difference between the excited state S_1 and the ground state S_0 . The decay rate for this transition follows first-order kinetics giving an exponential decay and is typically around 0.5 ns to 20 ns.

Since some of the energy absorbed from the incident photon has been lost in the system due to relaxation the emitted photon will be of lower energy and thus of a longer wavelength than the incident photon. When a volume of fluorophores in a solvent is excited the electrons can decay into a range of different rovibronic sublevels in the ground state which results in photons with different wavelengths. Since the rovibronic sublevels of the dissolved fluorophores are nearly infinitesimally

close in energy the many photons will form a continuous spectrum of wavelengths (see Figure 2.3). Likewise, there are a great number of different photon energies that are able to excite the electron. These energy ranges are called the excitation and absorption spectra.

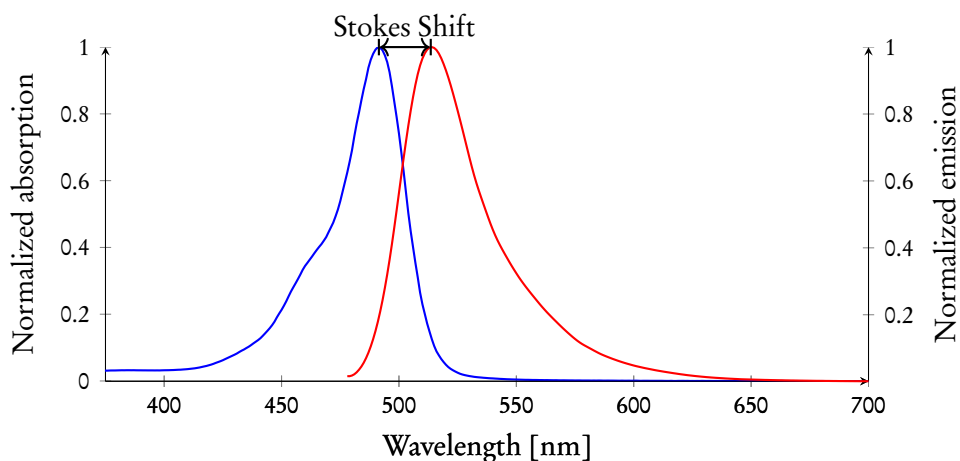


Figure 2.3: The absorption (blue) and emission (red) spectra of the fluorescent dye fluorescein.

As it can be seen from Figure 2.3 there is a distinct optimum wavelength of absorption and of maximum emission. The distance between these two maxima is called the Stokes shift. In microscopy and spectroscopy it is preferable to have a large Stokes shift since this makes it easier to distinguish and filter out incident light from emitted light.

2.2 Two-Photon Absorption

So far, we have only considered the case where a single photon is absorbed by a fluorophore exciting it to a higher electronic state in a single quantum event. In 1931, Göppert-Mayer [23] provided the theoretical basis for a different method of excitation: two-photon absorption. In her paper, she explains how two photons can act together on a molecule in a single quantum step to excite the molecule (see Figure 2.4).

The basic principle is that when the first photon is absorbed by the fluorophore it excites the fluorophore into a so-called “virtual” state. The second photon then further excites the fluorophore into one of the excited electronic states. It is important to notice that the virtual state depicted in Figure 2.4 is not an actual molecular state, but rather a superposition of wave functions of all the different states in the molecule. An electron will never be found in the virtual state at any time, even though the virtual state has a defined lifetime (a time-scale of about 0.1 fs).

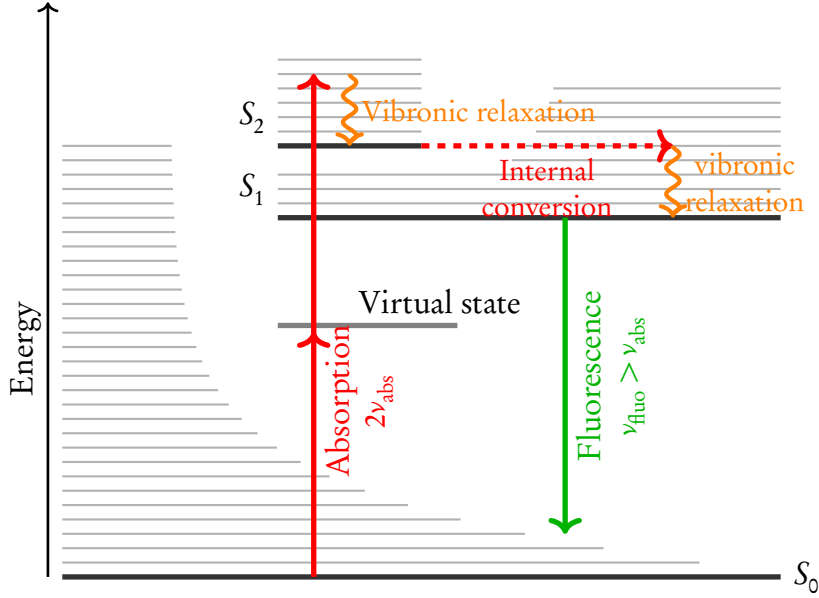


Figure 2.4: Simplified Jablonski Diagram showing selected conversion pathways for energy obtained through absorption of two photons.

The two-photon absorption rate can be calculated using quantum mechanics and perturbation theory. The derivation is based on the relevant chapters in [24], [25] and [26].

In quantum mechanics, the atomic wave function $\psi(\vec{r}, t)$ is assumed to be a solution to the time-dependent Schrödinger equation

$$i\hbar \frac{\partial \psi(\vec{r}, t)}{\partial t} = \hat{\mathcal{H}} \psi(\vec{r}, t), \quad \hat{\mathcal{H}} = \hat{\mathcal{H}}_0 + \hat{V}(t), \quad (2.1)$$

where $\hat{\mathcal{H}}_0$ is the Hamiltonian for a free atom and

$$\hat{V}(t) = -\hat{\mu} \tilde{E}(t) \quad (2.2)$$

is the interaction energy with the incident electromagnetic field $\tilde{E}(t)$ ² and $\hat{\mu} = -e\hat{r}$ is the electric dipole moment operator of electron charge e with displacement vector \vec{r} . The field is chosen to be a monochromatic plane wave, with an angular frequency ω and electric field magnitude E , defined by the following equation:

$$\hat{E}(t) = E \exp(i\omega t) + c.c. \quad (2.3)$$

which is applied at $t = 0$. Next, it is assumed that the solutions to Schrödinger's equation are known for a free atom, and that the associated wavefunctions with the

²The tilde denotes a quantity that changes rapidly in time

energy eigenstates $u_n(\vec{r})$ and eigenvalues ω_n can be expressed as

$$\psi_n(\vec{r}, t) = u_n(\vec{r}) \exp(-i\omega_n t), \quad \omega_n = \frac{E_n}{\hbar} \quad (2.4)$$

where the subscript n denotes various solutions. The solutions are assumed to form a complete, orthonormal set that satisfies the condition

$$\int u_m^* u_n d^3 r = \delta_{mn}, \quad (2.5)$$

where δ_{mn} is the Kronecker delta.

If $\hat{\mathcal{H}} = \hat{\mathcal{H}}_0$ and $u_n(\vec{r})$ satisfies the time-independent Schrödinger equation

$$\hat{\mathcal{H}}_0 u_n(\vec{r}) = E_n u_n(\vec{r}) \quad (2.6)$$

then Equation 2.4 satisfies Equation 2.1 at $t = 0$. Now the Hamiltonian $\hat{\mathcal{H}}$ is expanded to the original form shown in Equation 2.1 where a time-dependent perturbation is present:

$$i\hbar \frac{\partial \psi(\vec{r}, t)}{\partial t} = (\hat{\mathcal{H}}_0 + \hat{V}(t))\psi(\vec{r}, t), \quad \hat{\mathcal{H}} = \hat{\mathcal{H}}_0 + \hat{V}(t). \quad (2.7)$$

Because the energy eigenstates of $\hat{\mathcal{H}}_0$ form a complete set the solutions to Equation 2.7 can be expressed as a linear combination of the eigenstates:

$$\psi(\vec{r}, t) = \sum_l a_l(t) u_l(\vec{r}) \exp(-i\omega_l t), \quad (2.8)$$

where $a_l(t)$ is the probability amplitude that, at time t , the atom is in energy eigenstate l .

Inserting Equation 2.8 into Equation 2.7 the following result is obtained:

$$\begin{aligned} i\hbar \sum_l \frac{da_l}{dt} u_l(\vec{r}) \exp(-i\omega_l t) + i\hbar \sum_l (-i\omega_l) a_l(t) u_l(\vec{r}) \exp(-i\omega_l t) \\ = \sum_l E_l a_l(t) u_l(\vec{r}) \exp(-i\omega_l t) + \sum_l a_l(t) \hat{V} u_l(\vec{r}) \exp(-i\omega_l t). \end{aligned} \quad (2.9)$$

It is evident that the second and third term in the above expression cancel out completely, leading to the following equation:

$$i\hbar \sum_l \frac{da_l}{dt} u_l(\vec{r}) \exp(-i\omega_l t) = \sum_l a_l(t) \hat{V} u_l(\vec{r}) \exp(-i\omega_l t) \quad (2.10)$$

This expression is then multiplied by $u_m^*(\vec{r})$ (from the left) and integrated over all space. By using the orthonormality condition (Equation 2.5) we can remove all terms of the sum over l on the left-hand side, except for the case $l = m$, and obtain

$$i\hbar \frac{da_m}{dt} = \sum_l a_l(t) V_{ml} \exp(i\omega_{ml} t). \quad (2.11)$$

Here $\omega_{ml} = \omega_l - \omega_m$ is the energy difference between the eigenstates m and l in units of angular frequency and

$$V_{ml} = \langle u_m | \hat{V} | u_l \rangle = \int u_m^*(\vec{r}) \hat{V} u_l(\vec{r}) d^3 r \quad (2.12)$$

are the matrix elements of the interaction Hamiltonian \hat{V} .

Equation 2.11 cannot be solved exactly, and this is where perturbation theory comes into the picture. An expansion parameter λ , which is assumed to vary continuously in the range $[0; 1]$, is introduced to the equation. The value $\lambda = 1$ corresponds to the current physical situation in this problem. By substituting V_{ml} with λV_{ml} and expanding $a_m(t)$ in powers of the interaction parameter λ , we get

$$a_m(t) = a_m^{(0)}(t) + \lambda a_m^{(1)}(t) + \lambda^2 a_m^{(2)}(t) + \dots + \lambda^N a_m^{(N)}(t) \quad (2.13)$$

where (N) is the order of the interaction. From here, it is possible to equate the powers of λ on each side of the resulting form of Equation 2.11 and obtain the following set of equations

$$\frac{da_m^{(N)}}{dt} = (i\hbar)^{-1} \sum_l a_l^{(N-1)}(t) V_{ml} \exp(i\omega_{ml}t), \quad N = 1, 2, 3, \dots \quad (2.14)$$

An important feature of this equation is the fact that the probability amplitude of order N is related to the amplitude of order $N-1$. Because two-photon absorption has a second-order probability amplitude this simplifies the calculations involved in finding the transition rate because we only need to solve the equation for $N = 0, 1$ and 2 before calculating the transition rate from the probability amplitude.

2.2.1 One-Photon Absorption Cross Section

First, we need to find the expression for linear (one-photon) absorption. By using Equation 2.14 and setting $N = 1$, which corresponds to a first-order interaction in the electromagnetic field, and assuming that, in the absence of the field, the atom is in the lowest state l (usually the ground state) we have the following starting conditions:

$$a_l^{(0)}(t) = 1, \quad a_m^{(0)}(t) = 0 \quad \text{for } m \neq l \quad (2.15)$$

for all times t . By using Equation 2.2 and 2.3, V_{ml} can be written as

$$V_{ml} = -\mu_{ml} (E \exp(-i\omega t) + E^* \exp(i\omega t)). \quad (2.16)$$

Inserting all this into Equation 2.14 gives

$$\frac{da_m^{(1)}}{dt} = -(i\hbar)^{-1} \mu_{ml} (E \exp(i(\omega_{ml} - \omega)t) + E^* \exp(i(\omega_{ml} + \omega)t)). \quad (2.17)$$

By time integrating Equation 2.17, we get

$$\begin{aligned}
 a_m^{(1)}(t) &= -(i\hbar)^{-1} \mu_{ml} \int_0^t dt' \left[E e^{i(\omega_{ml}-\omega)t'} + E^* e^{i(\omega_{ml}+\omega)t'} \right] \\
 &= \frac{\mu_{ml} E}{\hbar(\omega_{ml}-\omega)} \left[e^{i(\omega_{ml}-\omega)t} - 1 \right] + \frac{\mu_{ml} E^*}{\hbar(\omega_{ml}+\omega)} \left[e^{i(\omega_{ml}+\omega)t} - 1 \right] \quad (2.18)
 \end{aligned}$$

The two terms in Equation 2.18 represent one-photon absorption and stimulated emission, respectively. The first term in the expression can become resonant for the one-photon absorption process and the second term can, if state m lies below state l , become resonant with the process of stimulated emission. Since we are only interested in the case of one-photon absorption we can simply drop the second term (this maneuver is called the rotating wave approximation). Now that we have the probability amplitude $a_m^{(1)}(t)$ we can use this to find the probability $p_m^{(1)}(t)$ that the atom is in the state m at time t

$$\begin{aligned}
 p_m^{(1)}(t) &= \left| a_m^{(1)}(t) \right|^2 = \frac{|\mu_{ml} E|^2}{\hbar^2} \left| \frac{e^{i(\omega_{ml}-\omega)t} - 1}{\omega_{ml} - \omega} \right|^2 \\
 &= \frac{|\mu_{ml} E|^2}{\hbar^2} \frac{4 \sin^2[(\omega_{ml} - \omega)t/2]}{(\omega_{ml} - \omega)^2} \equiv \frac{|\mu_{ml} E|^2}{\hbar^2} f(t), \quad (2.19)
 \end{aligned}$$

where

$$f(t) = \frac{4 \sin^2[(\omega_{ml} - \omega)t/2]}{(\omega_{ml} - \omega)^2} \quad (2.20)$$

By simplifying $f(t)$ using the substitution $x = (\omega_{ml} - \omega)t/2$, which gives us

$$f(t) = t^2 \left(\frac{\sin^2 x}{x^2} \right), \quad (2.21)$$

we can now easily examine the time-dependence of $f(t)$ for large values of time t by plotting the function for varying x with an arbitrary constant value of t .

Figure 2.5 shows the results of this plot, and from there we can see that the central peak has a value of t^2 while the full width at half maximum is of the order of $2\pi/t$. The area under the peak is then of the order of $2\pi t$, and as t increases the function becomes more highly peaked. From these features, we can approximate $f(t)$ as being proportional to t times a Dirac delta function. Since our variable x is still dependent on t it is straightforward to show that

$$\lim_{t \rightarrow \infty} f(t) = 2\pi t \delta(\omega_{ml} - \omega). \quad (2.22)$$

Applying this limit to Equation 2.19, we now get

$$p_m^{(1)}(t) = \frac{|\mu_{ml} E|^2 t}{\hbar^2} 2\pi \delta(\omega_{ml} - \omega). \quad (2.23)$$

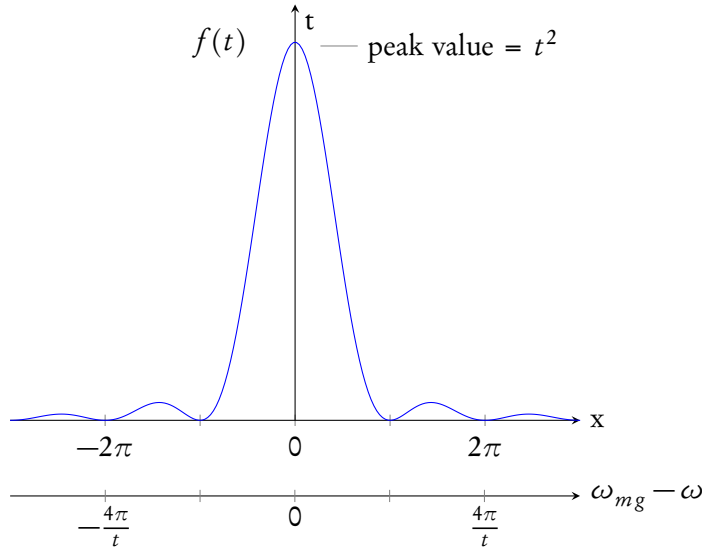


Figure 2.5: Plot of $f(t)$ of Equation 2.21. It is clear how the function resembles a Dirac delta function.

This result, however, does not conform with experimental observations because the frequency ω_{ml} is not truly monochromatic, as the above equation suggests, but rather spread over a continuous distribution. This is a result of various line-broadening mechanisms. This distribution is usually called the density of final states $\rho_f(\omega_{ml})$, which is defined in such a way, that $\rho_f(\omega_{ml})d\omega_{ml}$ is the probability that the transition frequency lies between ω_{ml} and $\omega_{ml} + d\omega_{ml}$. The density of final states is normalized according to the following expression

$$\int_0^{\infty} \rho_f(\omega_{ml}) d\omega_{ml} = 1. \quad (2.24)$$

The Lorentz distribution provides a good description of the broadening of excited states due to the uncertainty principle stating that the lifetime of an excited state is related to the uncertainty of its energy. The Lorentz distribution is defined by the following expression

$$\rho_f(\omega_{ml}) = \frac{1}{\pi} \frac{\Gamma/2}{(\bar{\omega}_{ml} - \omega_{ml})^2 + (\Gamma/2)^2} \quad (2.25)$$

where $\bar{\omega}_{ml}$ is the line-center transition frequency, and Γ is the full-width at half maximum of the distribution in angular frequency units. For an excited state Γ is the lifetime of the excited state.

Taking Equation 2.25 as an expression for the transition frequency we can apply this to Equation 2.23. The expression, however, must be averaged over all possible

values of the transition frequency, leading to

$$\begin{aligned} p_m^{(1)}(t) &= \frac{|\mu_{ml}E|^2 t}{\hbar^2} \int_0^\infty \rho_f(\omega_{ml}) 2\pi \delta(\omega_{ml}) d\omega_{ml} \\ &= \frac{2\pi |\mu_{ml}E|^2 t}{\hbar^2} \rho_f(\omega_{ml} = \omega) \end{aligned} \quad (2.26)$$

where $\rho_f(\omega_{ml} = \omega)$ simply means that the density of final states should be evaluated at the frequency ω of the incident laser light.

It is clear that the probability for the atom to be in the excited state increases linearly with time which allows us to define a transition rate for one-photon absorption by dividing the probability with the time t

$$R_{ml}^{(1)}(t) = \frac{p_m^{(1)}(t)}{t} = \frac{2\pi |\mu_{ml}E|^2}{\hbar^2} \rho_f(\omega_{ml} = \omega). \quad (2.27)$$

This equation can also be expressed in terms of the light intensity and the absorption cross section $\sigma_{ml}^{(1)}(\omega)$ in the following way

$$R_{ml}^{(1)}(t) = \sigma_{ml}^{(1)}(\omega) I, \quad (2.28)$$

where the light intensity $I = 2n\epsilon_0 c |E|^2$. From this we can define the absorption cross section as

$$\sigma_{ml}^{(1)}(\omega) = \frac{\pi}{n\epsilon_0 c} \frac{|\mu_{ml}E|^2}{\hbar^2} \rho_f(\omega_{ml} = \omega). \quad (2.29)$$

2.2.2 Two-Photon Absorption Cross Section

With linear absorption done and accounted for we are ready to move on to two-photon absorption. To find the transition rate for a two-photon absorption we need to go back to Equation 2.14 and solve it for both $N = 1$ and $N = 2$ in order to get the probability amplitude $a_n^{(2)}$ for the atom to be in the excited state n at time t . Following the naming scheme used so far, the lower level is still called l and the excited state is n with m corresponding to an intermediate state between the former two.

The expression for $a_m^{(1)}(t)$ found in Equation 2.18 can be used directly on the right-hand side of Equation 2.14 to solve it for the case of $N = 2$. Again, we neglect the second term, since this does not contribute to the absorption process. For the transition from m to n , we define

$$\begin{aligned} V_{mn} &= -\mu_{mn} (E e^{-i\omega t} + E^* e^{i\omega t}) \\ &\simeq -\mu_{mn} E e^{-i\omega t}. \end{aligned} \quad (2.30)$$

Again, the negative-frequency contribution is dropped because it does not contribute to the absorption process. From this, we get

$$\begin{aligned} \frac{da_n^{(2)}(t)}{dt} &= (i\hbar)^{-1} \sum_m a_m^{(1)}(t) V_{nm} e^{i\omega_{nm}t} \\ &= -(i\hbar)^{-1} \sum_m \frac{\mu_{nm}\mu_{ml}E^2}{\hbar(\omega_{ml}-\omega)} \left[e^{i(\omega_{nl}-2\omega)t} - e^{i(\omega_{nm}-\omega)t} \right]. \end{aligned} \quad (2.31)$$

The second term in the square brackets represents the transient response of the system, but does not contribute to two-photon absorption. This is evident from the fact that the band gap energy ω_{nm} signifies a transition from state m to n . Since the expression describes a transition from state l to n , no molecules will be found in state m at time $t = 0$. Therefore this term is dropped from the equation. By integrating the equation we get an expression for the two-photon probability amplitude

$$a_n^{(2)}(t) = \sum_m \frac{\mu_{nm}\mu_{ml}E^2}{\hbar^2(\omega_{ml}-\omega)} \left[\frac{e^{i(\omega_{nl}-2\omega)t} - 1}{\omega_{nl}-2\omega} \right]. \quad (2.32)$$

From here on, the calculations are basically the same as for one-photon absorption. We proceed to find the probability for the atom to be in state n

$$p_n^{(2)}(t) = \left| a_n^{(2)}(t) \right|^2 = \left| \sum_m \frac{\mu_{nm}\mu_{ml}E^2}{\hbar^2(\omega_{ml}-\omega)} \right|^2 \left| \frac{e^{i(\omega_{nl}-2\omega)t} - 1}{\omega_{nl}-2\omega} \right|^2. \quad (2.33)$$

As before, for large t , the expression simplifies to

$$p_n^{(2)}(t) = \left| \sum_m \frac{\mu_{nm}\mu_{ml}E^2}{\hbar^2(\omega_{ml}-\omega)} \right|^2 2\pi\delta(\omega_{nl}-2\omega), \quad (2.34)$$

and assuming that state n is experiencing the same line broadening that we assumed before we get

$$p_n^{(2)}(t) = \left| \sum_m \frac{\mu_{nm}\mu_{ml}E^2}{\hbar^2(\omega_{ml}-\omega)} \right|^2 2\pi\rho_f(\omega_{nl}=2\omega). \quad (2.35)$$

Again, we see that the probability for the atom to be in state n increases linearly with time, and so we can define a transition rate as follows

$$R_{nl}^{(2)} = \frac{p_n^{(2)}(t)}{t} \quad (2.36)$$

which can be rewritten in terms of a two-photon absorption cross section by the following definition

$$R_{nl}^{(2)} = \sigma_{nl}^{(2)}(\omega)I^2 \quad (2.37)$$

where I , the intensity of the light beam, is defined as before. The two-photon absorption cross section is then shown to be

$$\sigma_{nl}^{(2)}(\omega) = \frac{1}{4n^2\epsilon_0^2c^2} \left| \sum_m \frac{\mu_{nm}\mu_{ml}}{\hbar^2(\omega_{ml} - \omega)} \right|^2 2\pi\rho_f(\omega_{nl} = 2\omega). \quad (2.38)$$

Most often, the intensity of the light beam is measured as a photon flux density with SI units of $\text{photon m}^{-2} \text{s}^{-1}$ (photon irradiance). With these units, the absorption rate and cross section needs to be expressed as

$$R_{nl}^{(2)} = \sigma_{nl}^{(2)}(\omega)E_q^2, \quad \text{where } E_q = \frac{2n\epsilon_0c}{\hbar\omega}|E|^2 \quad (2.39)$$

and

$$\sigma_{nl}^{(2)}(\omega) = \frac{\omega}{4n^2\epsilon_0^2c^2} \left| \sum_m \frac{\mu_{nm}\mu_{ml}}{\hbar(\omega_{ml} - \omega)} \right|^2 2\pi\rho_f(\omega_{nl} = 2\omega). \quad (2.40)$$

The units of $\sigma_{nl}^{(2)}(\omega)$ are then $\text{photon}^{-1} \text{m}^4 \text{s}$. Often, however, it is expressed in units of GM (After Maria Göppert-Mayer), which is defined as

$$1 \text{ GM} = 1 \times 10^{-58} \text{ photon}^{-1} \text{m}^4 \text{s}. \quad (2.41)$$

Because two-photon absorption depends on two photons exciting a fluorophore simultaneously a high photon flux density is required. Specifically, the fluorescence photon flux is proportional to the square of the incident light making two-photon absorption a third-order non-linear optical process. As is evident from the above evaluation, the photons involved in the process have an energy about half of the band gap between the lower (ground) state and the higher (excited) state.

Measuring the two-photon absorption cross section can be achieved using the two-photon induced fluorescence intensity. This was first done by Kaiser and Garrett [27] in 1961. If the quantum yield of the material is known it is possible to use this method to calculate the two-photon absorption cross section by using a reference material with a known 2PA cross section and quantum yield.

For a TPE process the number of photons absorbed per molecule per unit time is proportional to the two-photon absorption cross section as well as the square of the intensity of the incident light.³ The total number of photons absorbed per unit time N_{abs} is also dependent on the molecule concentration C and the volume of the sample being illuminated V

$$N_{\text{abs}} = \int_V d\vec{r} \sigma^{(2)} C(\vec{r}, t) I^2(\vec{r}, t). \quad (2.42)$$

³For the remainder of this thesis, the subscript indices on the absorption cross sections will be omitted.

For cases, where we can disregard photobleaching and ground-state depletion, which we generally would like to avoid, the concentration can be assumed a constant. If the properties of the incident light permits us to separate it into a temporal and spatial part the expression then rewrites to

$$N_{\text{abs}} = \sigma^{(2)} C I_0^2(t) \int_V d\vec{r} S^2(\vec{r}). \quad (2.43)$$

Here $I_0^2(t)$ is the time-dependent part of the light beam and $S^2(\vec{r})$ is the dimensionless spatial distribution defined by $I^2(\vec{r}, t) = I_0^2(t) S^2(\vec{r})$. The time-dependent part describes the intensity at the geometric focal point.

The number of emitted photons from the TPE process can then be expressed as

$$F(t) = \frac{1}{2} \phi \eta N_{\text{abs}} \quad (2.44)$$

where the factor of $1/2$ simply stems from the need for two photons to excite the fuophore to emit one photon. ϕ is the collection efficiency of the measurement system and η is the fluorescence quantum yield.

In practice, the measured quantity is always the time-averaged fluorescence photon flux

$$\langle F(t) \rangle = \frac{1}{2} \phi \eta \sigma^{(2)} C \langle I_0^2(t) \rangle \int_V d\vec{r} S^2(\vec{r}). \quad (2.45)$$

Since most power meters measure $\langle I_0(t) \rangle$ and not $\langle I_0^2(t) \rangle$ it is necessary to rewrite Equation 2.45 as

$$\langle F(t) \rangle = \frac{1}{2} g^{(2)} \phi \eta \sigma^{(2)} C \langle I_0(t) \rangle^2 \int_V d\vec{r} S^2(\vec{r}) \quad (2.46)$$

where $g^{(2)}$ is the 2nd-order temporal coherence of the excitation source given by

$$g^{(2)} = \frac{\langle I_0^2(t) \rangle}{\langle I_0(t) \rangle^2}. \quad (2.47)$$

Most lasers, including ours, operate in TEM₀₀ mode which gives a Gaussian-Lorentzian spatial profile for which the intensity distribution is given by

$$I(\rho, z, t) = \frac{2P(t)}{\pi W^2(z)} \exp\left[-\frac{2\rho^2}{W^2(z)}\right] \quad (2.48)$$

where z is the distance along the optical axis, ρ is the distance away from the optical axis, $P(t)$ is the incident power,

$$W(z) = W_0 \left[1 + \left(\frac{z}{z_R} \right)^2 \right]^{1/2}, \quad (2.49)$$

and

$$z_R = \frac{n_0 \pi W_0^2}{\lambda}. \quad (2.50)$$

Here, z_R is the Rayleigh length of the beam [28, pp. 664-668], λ is the excitation light wavelength, and n_0 is the refractive index of the medium. From Equations 2.48–2.50 it is trivial to obtain the expressions for $I_0(t)$ and $S(\vec{r})$

$$I_0(t) = \frac{2P(t)}{\pi W_0^2} \quad (2.51)$$

$$S(\vec{r}) = \frac{W_0^2 \exp\left[-\frac{2\rho^2}{W^2(z)}\right]}{W^2(z)}. \quad (2.52)$$

If the sample thickness is much larger than z_R the expression for $S(\vec{r})$ can be solved analytically and the equation obtained is

$$\int_{V \rightarrow \infty} S^2(\vec{r}) = \frac{1}{4} \frac{n_0 \pi^3 W_0^4}{W^2(z)}. \quad (2.53)$$

Thus, from Equations 2.46, 2.51 and 2.53 we arrive at an expression for the experimentally detected fluorescence

$$\langle F(t) \rangle = \frac{1}{2} g^{(2)} \phi \eta C \sigma^{(2)} n_0 \frac{\pi \langle P(t) \rangle^2}{\lambda}. \quad (2.54)$$

To calculate the two-photon absorption cross section of a fluorophore we can use an already documented fluorophore with a well-defined cross section and measure the fluorescence photon flux of the two under identical (or precisely controlled) conditions. By isolating $\sigma^{(2)}$ in Equation 2.54 for a sample ($\langle F_S(t) \rangle$) and reference ($\langle F_R(t) \rangle$), respectively, and dividing the two resulting expressions we obtain the following equation:

$$\sigma_S^{(2)} = \frac{\langle F_S(t) \rangle \langle P_R(t) \rangle^2 g_R^{(2)} \phi_R n_{0,R} \eta_R C_R}{\langle F_R(t) \rangle \langle P_S(t) \rangle^2 g_S^{(2)} \phi_S n_{0,S} \eta_S C_S} \sigma_R^{(2)}. \quad (2.55)$$

The subscripts R and S refer to the reference and sample, respectively. Under identical experimental conditions this expression simplifies to the following equation

$$\sigma_S^{(2)} = \frac{\langle F_S(t) \rangle \langle P_R(t) \rangle^2 \eta_R C_R}{\langle F_R(t) \rangle \langle P_S(t) \rangle^2 \eta_S C_S} \sigma_R^{(2)}. \quad (2.56)$$

Equation 2.56 is very powerful since it simplifies the process of calculating the two-photon absorption cross section of a novel fluorophore significantly as long as a fluorophore with a well-defined cross section is available.

2.3 Stimulated Emission

In 1916, Einstein [29] described his theoretical discovery of stimulated emission of photons from molecules by interaction with an electromagnetic radiation field. The theory was further elaborated on in [30]. If the molecules have the two electronic states S_n and S_m , whose energies are ϵ_n and ϵ_m , respectively, we state that these energies satisfy the inequality $\epsilon_m > \epsilon_n$. Individual photons of an electromagnetic field are able to interact with the molecules in the field. Thus it is possible for a molecule to transition from state S_n to S_m by absorbing radiation energy $\nu = \epsilon_m - \epsilon_n$ from the field.

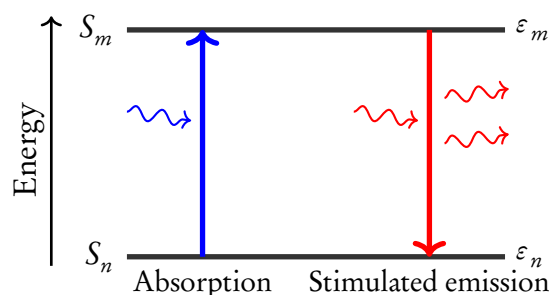


Figure 2.6: Simplified two-level Jablonski Diagram of stimulated emission. Downward slanted wavy arrows represent absorbed photons; upwards slanted wavy arrows represent emitted photons. A photon with energy $\nu = \epsilon_m - \epsilon_n$ is absorbed and induces the transition from S_n to S_m . A photon with energy $\nu = \epsilon_m - \epsilon_n$ interacts with the molecule and stimulates the emission of a photon of identical energy resulting in two photons leaving the molecule as it decays from S_m to S_n .

Conversely, a molecule in state S_m may transition to state S_n by emitting radiation with an energy $\epsilon_m - \epsilon_n$. This process can happen both spontaneously and by interaction with a photon of equal energy (the latter is sometimes referred to as “negative absorption”). The probability for each of these processes occurring are given by

$$dW = A_m^n dt \quad \text{spontaneous emission} \quad (2.57)$$

$$dW = B_n^m \rho(\nu) dt \quad \text{absorption} \quad (2.58)$$

$$dW = B_m^n \rho(\nu) dt \quad \text{stimulated emission} \quad (2.59)$$

where $\rho(\nu)$ is the radiation flux density of the electromagnetic field. The coefficients A_m^n , B_n^m and B_m^n are the Einstein coefficients for these specific transitions. The process of stimulated emission is actually the main principle behind laser operation [31].

The probability amplitude for the process of stimulated emission can be isolated from Equation 2.18 where the second term in the expression represents the transition from S_m to S_n influenced by a photon with angular frequency ω .

2.4 Confocal Microscopy

The first compound microscope was invented sometime in the 17th century [32]. It worked by illuminating a sample from below and collecting the transmitted light through two magnifying lenses (see Figure 2.7). The technique, which is termed bright-field microscopy, gave researchers the first look into the microscopic world. The image obtained from this microscope is a contrast image where details of the sample arise through absorbance of light in the sample. The name bright-field is derived from the fact that the microscope collects light from a wide field of view at once (wide-field) by illuminating the sample with bright white light.

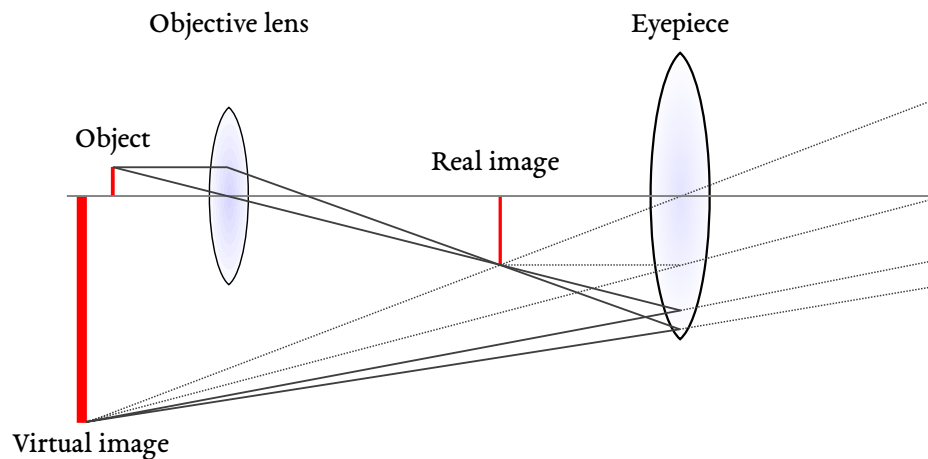


Figure 2.7: Ray diagram of a simple compound microscope. Light from the object in focus travels through the objective lens and is focused into a *real image* inside the microscope. The real image is magnified by the eyepiece which gives an inverted *virtual image*.

Because many biological samples only provide low and unspecific contrast the brightfield microscope has largely been superseded by newer techniques. One of the most important advances in microscopy is the introduction of fluorescence microscopy.

In Section 2.1, I explained how fluorescence microscopy utilizes the fact that some molecules, when irradiated with intense light, will emit light at a higher wavelength. This enables researchers to obtain a greater contrast in their images since they can filter out the incident light and only observe that which is emitted from the sample. By developing antibodies that target specific molecules in a sample and coupling them with a fluorescent dye it is thus possible to get very detailed

micrographs of specific cellular structures in a biological sample. It is even possible to utilize the inherent autofluorescence, which some tissue types exhibit.

Fluorescence wide-field, as well as bright-field, microscopy suffers from a serious disadvantage. If the sample is too thick, light from the out-of-focus parts of the sample create a uniform glow in the background, which blurs the image and obscures details in the sample. To overcome this limitation it is necessary to find a way to filter out all the unwanted light. In 1961, Minsky [2] filed a patent for an invention he designed in 1955: the confocal microscope.

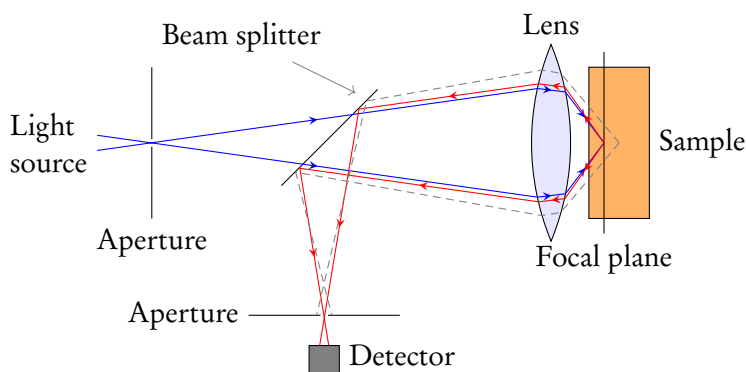


Figure 2.8: Diagram of the operating principle behind confocal microscopy. The blue rays are the incident light; the red rays are the emitted light and the grey rays are out of focus emitted light (Adapted from [2]).

In confocal microscopy an aperture is inserted in front of a focused light source with the pinhole centered at the focal point. Light enters the pinhole before going through a beam splitter and series of lenses and gets focused at a small point in the sample (see Figure 2.8).

The light emitted from the sample will travel back through the series of lenses and be reflected by the beam splitter down to a detector. In front of the detector, at the focal length is another aperture. This aperture will only allow light emitted by a specific point in the sample to go through and hit the detector, while the rest will be filtered away, because it will be diffracted differently through the lenses before hitting the beam splitter.

This technique ensures that the detector only picks up light emitted from the small volume of the sample that is situated in the focal plane essentially increasing the level of detail available. It is worth noting that this technique improves resolution at the cost of light intensity from the sample, which results in a lower signal-to-noise ratio. This limitation can be overcome by increasing the incident light intensity or using more sensitive photodetectors. Greater light power comes with the increased risk of bleaching the fluorophores or damaging the sample so great care must be taken.

The confocal microscope offered the improvements needed for researchers to advance knowledge in the bioimaging field. It took more than twenty years before

the technique found its way into laboratories around the world because the method came with an inherent obstacle, that needed to be overcome: since light is only gathered from one small point in the sample it is necessary to scan point-to-point in a raster-scan fashion to obtain an image of the sample. This requirement meant that the confocal microscope did not gain much recognition in its early years.

In the early 1980's, the first commercial confocal microscopes had become available. These systems were designed such that the sample would be illuminated by a laser source because the monochromatic nature of lasers makes it much easier to filter away incident light from emitted light. The sample was scanned by having the stage move in two directions in a raster-like approach to obtain a two-dimensional image [33]. These systems were very slow (close to 1 frame per second with a raster size of $256 \cdot 256$ pixels) and highly sensitive to vibrations and thus not convenient.

In 1985, Wilke [34] described a new approach to image acquisition from a confocal microscope. By moving the laser spot across the sample using mirrors that could scan a raster it would be possible to obtain images at a much higher rate and without having to physically move the sample stage, thus minimizing image defects from vibrations in the stage. In 1986, White [35] had a working prototype of a laser scanning microscope based on the moving mirrors principle, and in 1987 White [35] published the first promising results of the setup which boasted a scan speed of 4 frames per second with a raster size of $520 \cdot 576$ pixels. Since then, the Confocal Laser Scanning Microscope (CLSM) has been pretty much standard in every bio-imaging researchers laboratory line-up, and it also formed the basis for TPEM [3].

TPEM is a non-linear optical microscopy technique, in which the fluorescence intensity is proportional to the square of the incident light intensity, whereas in one-photon microscopy the fluorescence is linearly proportional to the incident light intensity. To put this into perspective, in broad daylight, a one-photon absorption will occur about once every second, whereas a two-photon absorption will only occur once every billion years [36]. However, this non-linear dependence also means that two-photon excitation microscopy has an inherent optical sectioning ability because the focal volume is confined to about 1 femtoliter (1 fL) which gives it a resolution comparable to confocal microscopy without the need for pinholes. The schematic differences between confocal and TPEM is shown in Figure 2.9.

Since TPEM does not rely on pinholes it is not necessary to descanned the fluorescence signal before collection [37]. The inherent optical sectioning also means that there is not any fluorescence signal originating from out-of-focus areas of the sample, which means that collecting the scattered light from the sample does not result in a blurred image, but instead gives a higher signal to noise ratio and thus an increased contrast compared to regular confocal microscopy. Penetration depth of confocal microscopy is limited because of scattering. Scattering of light is proportional to the size of the scattering particles and inversely proportional to the wavelength of the light meaning that the shorter wavelengths used in confocal microscopy will scatter more than TPEM. Penetration depth of TPEM is also not only dependent on the wavelength, but depends to a high degree on the surface power P_0 of the laser

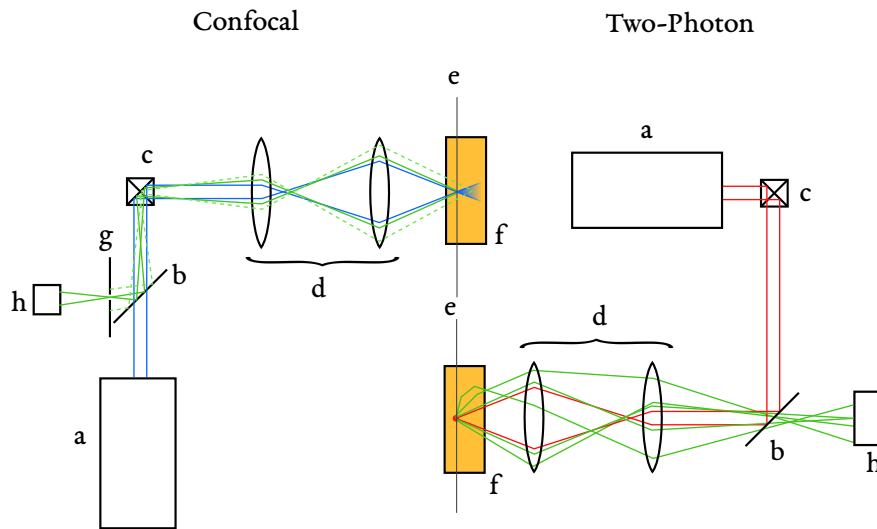


Figure 2.9: Schematic of the differences and similarities between confocal and two-photon excited microscopy. *a*) laser; *b*) dichroic mirror; *c*) x-y scanner head; *d*) microscope; *e*) focal plane; *f*) sample; *g*) pinhole; *h*) photomultiplier detector.

light and the “mean free path” l_s of the sample because only ballistic (non-scattered) photons contribute to the absorption process [4, box 1]. These properties enable TPEM to image deep within the tissue (up to a mm) where confocal microscopy is generally limited to $\sim 100 \mu\text{m}$. Furthermore, the longer wavelengths are much less phototoxic to the sample, thus resulting in decreased bleaching of the sample. The increased wavelength does, however, come with the price of lowered resolution. An explanation for this phenomena is presented in the following section.

2.4.1 Optical Resolution

In its most basic form, resolution is the measure of information available in an image. In a digital image, this is measured by the number of individual pixels present. In microscopy, however, the number of pixels alone is not enough. It is true that each pixel holds a value that describes the light intensity at that particular spatial point, but just like four identical images does not give more information of the scene depicted, so does pixels that show the exact same detail not provide more information of that detail.

In microscopy, the light collected from a sample will be diffracted by the lenses in the optical path and this diffraction limits how small objects we are able to detail. For a perfect lens with a circular aperture the diffraction pattern is known as an Airy pattern or Airy disk (see Figure 2.10). In 1873, Abbe [5] derived his famous

formula defining the diffraction limit of optical microscopes

$$d = \frac{\lambda}{2NA} \quad (2.60)$$

where d is the radius of the central disk in the Airy pattern of a point-like light source or object, λ is wavelength of the light, and NA is the numerical aperture of the objective which is defined as the refractive index n times the sine of the angular aperture α ⁴. This equation states that the resolution of an optical microscope is physically limited by the numerical aperture of the objective and proportional to the wavelength of the light collected from the sample.

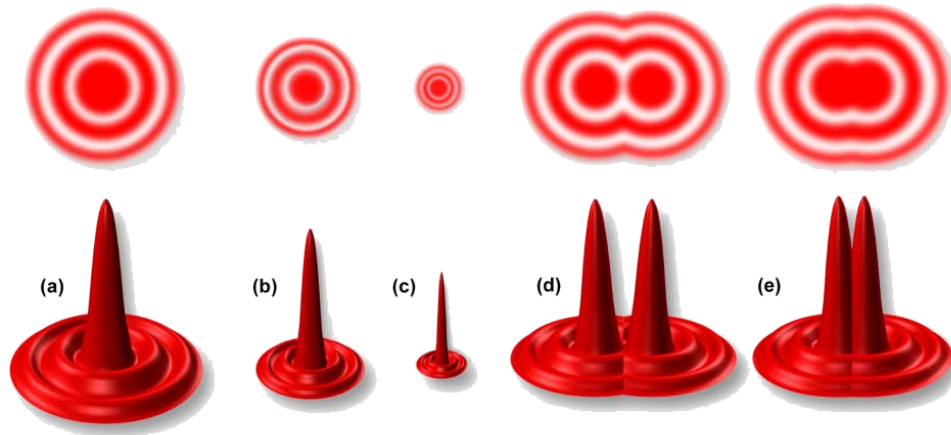


Figure 2.10: (a-c) Airy disk size and correlating intensity profile (or lateral Point spread function). The disk size is inversely proportional to the numerical aperture of the objective. (d) Two Airy disks with clear distinction. (e) Two barely distinguishable Airy disks. From [38].

To be able to distinguish between two objects a minimum distance between them is needed. One of the classic definitions for this, known as the Rayleigh criterion [38], is based on Equation 2.60:

$$d = 1.22 \frac{\lambda}{2NA}. \quad (2.61)$$

The factor of 1.22 was chosen somewhat arbitrarily from a calculation of the position of the first dark ring in an Airy pattern. Thus, if the light collected from the sample is 500 nm, and the objective has an NA = 1.4, the minimum distance between two objects in the sample needs to be 218 nm.

⁴the half-angle of the cone spanned by the diameter of the lens with height equal to the focal length of the lens

To resolve these objects the pixel sampling distance⁵ should necessarily be smaller than the smallest features resolvable by the microscope. In order to determine how much smaller we can use the Nyquist-Shannon theorem which is used in digital signal processing to determine the minimum sample rate needed to make a perfect reconstruction of an analog signal [39]. Even though this theorem was originally presented in the context of audio processing in telecommunication it is readily applicable in image acquisition and processing.

If a point-like object has a spatial intensity distribution $f(r)$ approximated as a symmetrical continuous function of position r then $F(Q)$ is the Fourier transformation of $f(r)$. We now say that $f(r)$ does not contain any signal above a cut-off N . By performing an inverse transformation of $F(Q)$ it can be shown that a sample rate of $1/(2N)$ is enough for perfect fidelity to $f(r)$:

$$f\left(\frac{n}{2N}\right) = \frac{1}{2\pi} \int_{-2\pi N}^{2\pi N} F(\omega) e^{i\omega \frac{n}{2N}} dN. \quad (2.62)$$

The left-hand side of Equation 2.62 are the values of $f(r)$ at the sampling points while the right-hand side corresponds to the n th coefficient of the Fourier-series expansion of $F(Q)$. Since this is zero for $|Q| > W$ it is completely determined with the values of the samples $f(n/(2N))$, and by extension we also completely determine $f(r)$. Combining this result with Equation 2.60, we get a minimum sample rate

$$\Delta r = \frac{\lambda}{4NA} \quad (2.63)$$

corresponding to half the radius of an Airy disk. This definition is also known as the Nyquist Criterion. Axial resolution is considerably lower (~ 500 nm) so a higher sampling distance in the z axis can be afforded.

2.5 STED Microscopy

In the preceding section we stated how the resolution of optical microscopes are limited by the diffraction of light through the system of lenses and apertures. So far, the highest resolution achieved with confocal microscopy is 180 nm in the lateral direction and 500 nm in the axial direction [40]. The lateral resolution is large enough to image microscopic cells including the larger cellular structures and organelles. However, many details that exists on length scales below the resolving limit are either hidden from our view or obscured such that it appears much larger than it is.

Transmission Electron Microscopy (TEM) is able to probe the samples at length scales much closer to atomic resolution. Low-voltage electron microscopy shows spatial resolutions of 2.5 nm [41]. The image formation mechanism here is analogous to the bright-field microscope (indeed, the standard operational mode of

⁵The distance between two pixel edges in the collected image.

TEM is referred to as bright-field) where the contrast is due to interactions between the ray of electrons with the sample. Areas that are thicker or have a higher atomic number will appear darker and areas with no sample will appear bright. Electron microscopy has some drawbacks, however. Very thin sections of sample are required (at most a few hundred nanometers), and the imaging process has to be performed in a vacuum chamber. These limitations make electron microscopy less than ideal, even though it represents a major advancement in terms of resolution and is actively used in imaging of nanometer-sized proteins and protein complexes.

Since optical microscopy is still the most convenient approach the perfecting of confocal microscopy has prompted research into increasing the numerical aperture as well as bypassing the diffraction limit. One such technology, termed stimulated emission depletion microscopy, was awarded one third of the 2014 Nobel prize in chemistry “for the development of super-resolved fluorescence microscopy”.

STED microscopy was first developed in 1994 by Hell and Wichmann [9]. The technique promised to vastly improve upon the resolving ability of fluorescence microscopy, enabling researchers to visualize details as small as ~ 30 nm [42], essentially filling the gap between conventional optical microscopy and electron microscopy. In 2005, Westphal and Hell [43] reported a focal spot size of 16 nm. Briefly, the concept of STED microscopy is to suppress the spontaneous emission around the periphery of the fluorescence focal spot by stimulating emission of photons using a laser pulse that is red-shifted with respect to the excitation laser.

Both lasers are still diffraction-limited, but the STED laser has a modified beam profile with a central zero intensity, e.g. like a doughnut. If the STED pulse intensity is greater than the molecular emission depletion threshold then the fluorescence area will be limited to a small region around the STED zero intensity center. Increasing the intensity of the STED laser will further decrease the fluorescence around the central zero. The resolution achievable with STED can be calculated from the normalized excitation probability $h_{\text{exc}}(r)$ and the STED laser intensity at the focal spot I_{STED} with $r = 0$ denoting the beam center. As mentioned in Section 2.1 the typical fluorescence lifetime is between 0.5 ns and 20 ns with a typical lifetime of 3 ns [43]. The vibrational lifetime is typically around 0.5 ps. A STED pulse duration τ of ~ 1 ns thus ensures complete fluorescence quenching by stimulated emission.

After the STED pulse has been fired the fluorescence probability $\eta(r)$ of a molecule at position r is given by

$$\eta(r) = \exp(-\sigma \tau I_{\text{STED}}(r)) \quad (2.64)$$

where $\sigma_{\text{STED}}^{(1)}$ is the cross section for stimulated emission. The probability to detect a photon at r is then proportional to

$$h(r) = h_{\text{exc}}(r)\eta(r). \quad (2.65)$$

The focal plane width maximum of the excitation laser is limited by Abbe’s diffraction limit and the same holds true for the STED laser minimum. For a lens

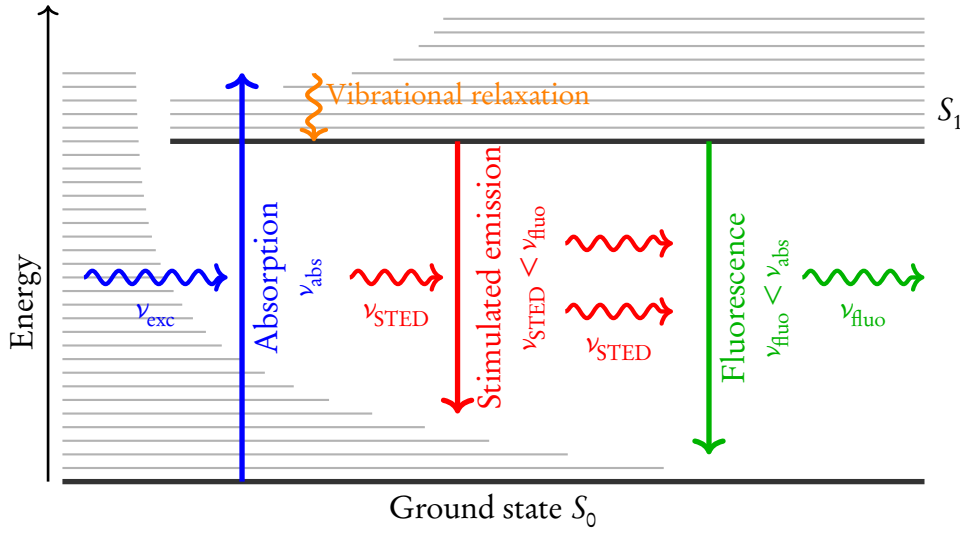


Figure 2.11: Jablonski Diagram showing possible electronic state pathways and associated photon events. Horizontal wave lines represent individual photons where color represents which transition the photon is linked to. A photon with energy ν_{exc} is absorbed and induces the transition from S_0 to S_1 . A photon with energy ν_{STED} interacts with the molecule and stimulates the emission of a photon of identical energy resulting in two photons leaving the molecule as it decays from S_1 to S_0 . A photon of energy ν_{fluo} is spontaneously emitted from the molecule during spontaneous decay from S_1 to S_0 .

with angular aperture α in a medium with refractive index n the spatial profiles of these can be expressed as a standing wave⁶

$$h_{\text{exc}}(r) = C \cos^2\left(\frac{\pi r n \sin(\alpha)}{\lambda_{\text{exc}}}\right) \quad (2.66)$$

$$I_{\text{STED}}(r) = \varsigma I_{\text{sat}} \sin^2\left(\frac{\pi r n \sin(\alpha)}{\lambda_{\text{STED}}}\right) \quad (2.67)$$

where C is a scaling constant for the point spread function, ς is the saturation level (which will be defined below), and $I_{\text{sat}} = 1/\sigma\tau$ is the STED laser intensity required to decrease the fluorescence to $1/e$ of the initial value. If we now define a new variable $I_{\text{STED}}^{\text{max}} = \max[I_{\text{STED}}]$ we can define the saturation level of STED in the following way

$$\varsigma = \frac{I_{\text{STED}}^{\text{max}}}{I_{\text{sat}}}. \quad (2.68)$$

⁶This profile is only chosen for simplicity. The calculations are valid for all possible beam profiles.

Inserting Equations 2.66 and 2.67 into Equation 2.65, with the approximation that $\lambda_{\text{exc}} \approx \lambda_{\text{STED}} \equiv \lambda$, gives the following

$$b(r) = C \cos^2 \left(\frac{\pi r n \sin(\alpha)}{\lambda} \right) \exp \left[-\zeta \sin^2 \left(\frac{\pi r n \sin(\alpha)}{\lambda} \right) \right]. \quad (2.69)$$

Because Equation 2.66 is normalized the factor of C is equal to 1. We then perform a Taylor expansion of the above around $r = 0$ to the 2nd order to get the expression

$$b(r) = 1 - \frac{\pi^2 n^2 \sin(\alpha)^2 (\zeta + 1) r^2}{\lambda^2}. \quad (2.70)$$

From here, we assume that $b(r) = 0.5$ at FWHM, since the expression is normalized, and then isolate r :

$$r = \frac{1}{2} \frac{\sqrt{2} \lambda}{\pi n \sin(\alpha) \sqrt{\zeta + 1}}. \quad (2.71)$$

Since the actual spot size in which fluorescence occurs (defined as Δr) is equal to FWHM we multiply Equation 2.71 by 2:

$$\Delta r = \frac{\sqrt{2}}{\pi \sqrt{1 + \frac{I_{\text{STED}}^{\text{max}}}{I_{\text{sat}}}}} \frac{\lambda}{n \sin(\alpha)} \approx 0.45 \frac{\lambda}{n \sin(\alpha) \sqrt{1 + \zeta}} = \frac{\lambda}{NA \sqrt{1 + \zeta}}. \quad (2.72)$$

This equation actually shows that going from confocal to STED microscopy in theory gives diffraction-unlimited resolution where the fluorescence spot size is determined by the STED laser power. Using Equation 2.72 to calculate the smallest spot size producible with a specific setup is straightforward: for an objective with an NA of 1.40, a saturation level $\zeta = 40$ and a STED wavelength $\lambda = 592$ nm we get a spot size $\Delta r \approx 35$ nm.

Figure 2.12 shows a schematic of a STED microscope setup. The depletion (STED) laser has a spectral line of 592 nm while the white light laser (WLL) is tunable to any and several (up to eight) wavelengths between 470 nm to 670 nm.

The WLL source is used to illuminate the sample. The working principle here is identical to a confocal microscope. The STED laser is sent through a vortex phase plate, where the gaussian-lorentzian beam is spatially polarized such that destructive interference occurs in the center of the beam, giving it a doughnut shape with a central zero intensity. The STED laser beam is sent through the same light path as the excitation laser beam and the two are aligned such that the beams overlap in the focal point.

The fluorophores in the sample are excited by the WLL laser giving a diffraction-limited fluorescent spot. The STED laser stimulates emission of photons from the excited molecules in the periphery of the diffraction-limited spot effectively decreasing the spot size to a sub-diffraction area size.

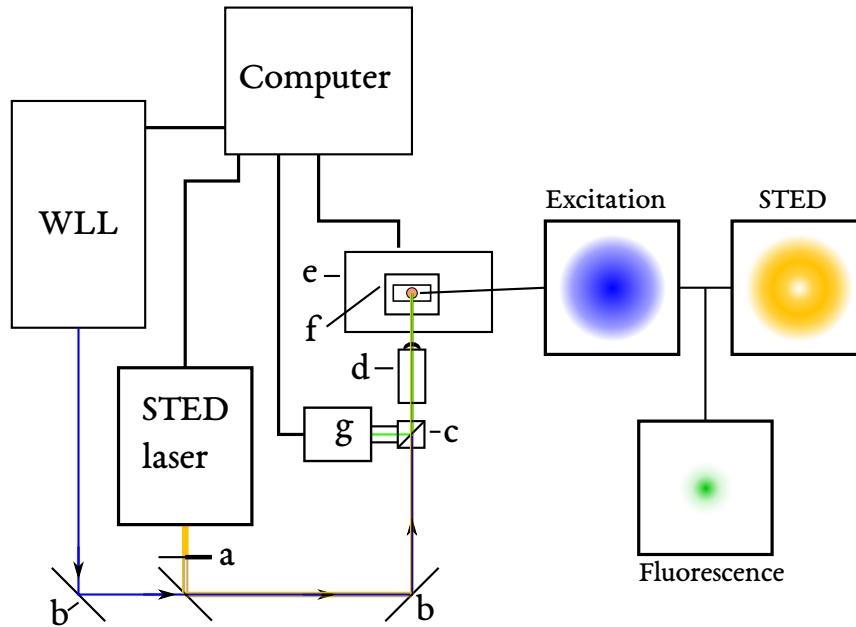


Figure 2.12: Schematic of a STED microscope. *a*) Vortex phase plate; *b*) mirrors; *c*) dichroic mirror; *d*) objective; *e*) microscope stage; *f*) sample; *g*) detector. Basic schematic of a STED microscopy system. The WLL and STED laser are aligned to overlap each other in the sample. The beam profiles of the excitation and STED laser as well as the resulting fluorescence profile is shown on the right.

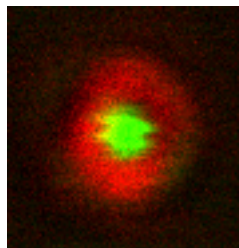


Figure 2.13: Point spread function of the WLL (green) and STED (red) laser imaged using gold nanobeads. It is clear that the STED beam profile is doughnut-shaped and overlaps the excitation laser, such that only the area corresponding with the center of the WLL beam will emit fluorescence.

2.6 Cell Junctions

Cell junctions are a type of cellular structure found in the tissue of many multicellular organisms (e.g. animals). Cell junctions are protein complexes that anchor neighboring cells to each other or to the extracellular matrix. In animal epithelial tissue, where cell junctions are plentiful, four main junction functions can be distinguished: *a*) anchoring junctions, *b*) occluding junctions, *c*) channel-forming junctions, *d*) signal-relaying junctions.

One example of signal-relaying junctions is the chemical synapse between neurons, but the other junction types can also aid in signal transmission in addition to their primary function. Because of the overlapping of functions the cell junctions are often categorized by their junctional type instead of their function. Here, there are also four categories [44, 45]:

- Tight Junctions
- Adherens Junctions
- Desmosomes
- Gap Junctions

These four types are illustrated in Figure 2.14. In epithelial tissue, a *gap junction* is an example of a channel-forming protein complex which provides direct contact between the cytoplasm of neighboring cells [46, 47].

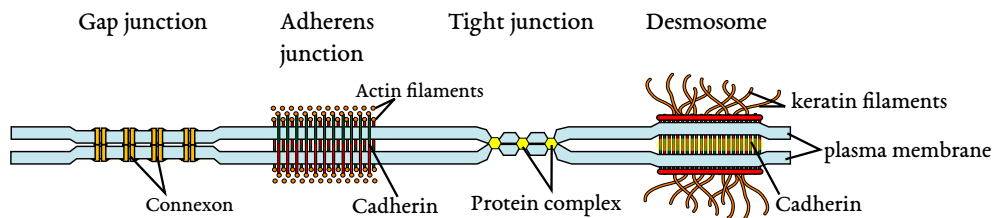


Figure 2.14: Schematic of different cell junction types: gap junction, tight junction, adherens junction, and desmosome. Figure was taken from wikipedia.org.

The epithelial cells are an example of polarized cells. Epithelial cells exhibit apical-basal polarity referring to the apical membrane facing the outside of the body (or the lumen of an internal cavity) and the basolateral membrane facing away from the lumen. The section of membrane, that faces adjacent cells (laterally) is part of the basolateral membrane.

Close to the apical side of the epithelial cells are a mesh of occluding junctions called *tight junctions*. Below these are two types of anchoring protein complexes. The *adherens junctions* in addition to facilitating cell-cell adhesion, function as anchoring sites for actin filaments in the cytoplasm. *Desmosomes* are much similar to adherens junctions, except that they are anchoring sites for intermediate filaments rather than actin.

2.6.1 Desmosomes

Adherens junctions in the epithelial cells often appear as a so-called adherens belt (or *zonula adherens*). In this belt, a family of transmembrane proteins called cadherins binds intercellularly with cadherins of apposing cells. The proteins are named for their calcium-dependent adhesive ability. Intracellularly they form complexes with several other proteins in order to link the adherens junction to the actin cytoskeleton [48] forming a strong network that allows the epithelial cell sheets to form invaginations in the membrane and other structures crucial during morphogenesis [49].

Desmosomes have a similar function of linking adjacent cells to each other. Desmoglein and desmocollin are specific members of the cadherin family which are only found in desmosome complexes. Despite being members of the cadherin family the desmosomal adhesion proteins are not calcium-dependent in their normal state [50]. This property means that desmosomes have a higher adhesive affinity and are thus able to withstand disintegration caused by mechanical forces. Intracellularly, the desmosomes function as anchoring sites for intermediate filaments. In epithelial tissue this consists of type I and II epithelial keratin [51]. Desmosomes are particularly abundant in epidermal and myocardium tissue that need to withstand a high degree of mechanical stress.

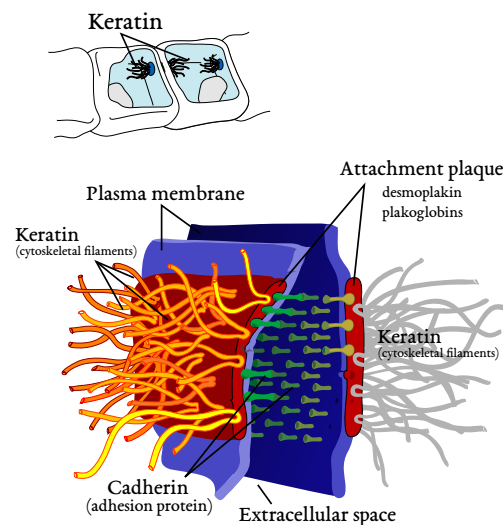


Figure 2.15: Schematic of a desmosome. The different cadherins, including desmoglein-1, connects intercellularly to apposing cadherins and anchor intracellularly to the attachment plaque made of the proteins desmoplakin and plakoglobin. The intermediate filaments of the cell also anchor to this plaque layer. Figure was taken from [wikipedia.org](https://en.wikipedia.org)

In the outermost layer of the epidermis, the *stratum corneum*, a special type of cell called corneocyte is found. Corneocytes are essentially dead cells since they do

not contain a nucleus or cytoplasmic organelles, but are instead filled with keratin and different types of lipids [12]. These corneocytes are held together primarily through corneodesmosomes (differentiated desmosomes that are only present in stratum corneum) [52].

2.6.2 Tight Junctions

Epithelial sheets cover and enclose the surface and internal cavities of the animal body, compartmentalizing the organism into specialized areas. To fulfill this purpose the epithelial sheets must be able to serve as selective permeability barriers that block diffusion of specific solutes through the paracellular pathway (between the cells). A major role in the barrier function is filled by *tight junctions*, a protein cluster consisting of claudin [16], occludin, and other occluding protein families [15]. As can be seen in Figure 2.14 these protein clusters bring the membranes of the neighboring cells into direct contact in order to form a seal such that solutes can not leak through gaps in the epithelium [15].

Tight junctions, analogous to adherens junctions, form *sealing strands* at the apical end of the epithelial cells, completely encircling the cell in an interwoven network. Different types of claudin confer permeability of specific solutes to the sheets in order to differentiate the specific permeability of different types of epithelial tissue [53].

Materials and Methods

3.1 Materials

Fixation was performed using a 4 % solution of formaldehyde in Dulbecco's PBS buffer (DPBS). *Sucrose infiltration* was performed in various concentrations of sucrose in DPBS. *Frozen sections* were prepared using 2-methylbutane (isopentane) (Sigma-Aldrich), Tissue-Tek O.C.T Compound (VWR), and liquid nitrogen. Sectioning was performed using a Cryotome FSE Cryostat (Thermo Scientific). *Paraffin embedding* was performed in a histokinette wherein different concentrations of ethanol was contained in alongside with Tissue-Tek Tissue-Clear and molten paraffin wax. Sectioning was performed on a microtome. *Immunostaining* involved several primary and secondary anti-bodies. The following were used in this thesis:

Primary antibodies

- Anti-Claudin 1 antibody [EPR9306] Rabbit monoclonal (Abcam[®])
- Anti-Desmoglein 1 antibody [27B2] Mouse monoclonal (Abcam[®])

Secondary antibodies

- Abberior 2C-Pack STED 590 VIS [2-0022-051-2] (Abberior GmbH)
Abberior STAR 488, goat anti-rabbit IgG
Abberior STAR 440SX, goat anti-mouse IgG

Coverslip coating, when performed, was done with a poly-L-lysine solution 0.1 % (w/v) in H₂O (Sigma-Aldrich). The coverslips are of type #1.5 (170(5) μm).

Sample mounting was done with three types of mounting media:

- Prolong[®] Gold Antifade Mountant [P36934] (Molecular Probes[®])

- Prolong[®] Diamond Antifade Mountant [P36961] (Molecular Probes[®])
- Mowiol Embedding Media (Recipe in appendix)

Additional fluorophores were tested as part of the calculations of 2-photon absorption cross-sections:

- (a) Fluorescein
- (b) Perylene
- (c) Rhodamine B
- (d) Rhodamine 6G
- (3) 2,5-Di(4-(4-cyano-2-fluorophenylethynyl)phenyl)-1,4-di(4-methylphenyl)-1,4-dihydropyrrolo[3,2-b]pyrrole
- (4) 2,5-Di(4-(4-cyanophenylethynyl)phenyl)-1,4-di(4-methylphenyl)-1,4-dihydropyrrolo[3,2-b]pyrrole
- (5) 2,5-Di(4-(4-pentafluorothiophenyl)ethynylphenyl)-1,4-di(4-methylphenyl)-1,4-dihydropyrrolo[3,2-b]pyrrole
- (6) 2,5-Di(4-(4-trifluoromethyl)ethynylphenyl)-1,4-di(4-methylphenyl)-1,4-dihydropyrrolo[3,2-b]pyrrole
- (7) 2,5-Di(4-(3,5-di(trifluoromethyl)ethynylphenyl)-1,4-di(4-methylphenyl)-1,4-dihydropyrrolo[3,2-b]pyrrole
- (8) 2,5-Di(4-(methoxy)ethynylphenyl)-1,4-di(4-methylphenyl)-1,4-dihydropyrrolo[3,2-b]pyrrole
- (9) 2,5-Di(4-(formylethynyl)phenyl)-1,4-di(4-methylphenyl)-1,4-dihydropyrrolo[3,2-b]pyrrole
- (10) 2,5-Di(4-cyanophenyl)-1,4-di(4-methylphenyl)-1,4-dihydropyrrolo[3,2-b]pyrrole
- (11) 2,5-Di(3-cyanophenyl)-1,4-di(4-methylphenyl)-1,4-dihydropyrrolo[3,2-b]pyrrole
- (25) 3-(9,9-Dioctyl-9H-fluoren-2-yl)-2,5-diphenyl-1,4-bis(4-methylphenyl)-dihydropyrrolo[3,2-b]pyrrole
- (26) 2,5-Bis(4-cyanophenyl)-3-(9,9-dioctyl-9H-fluoren-3-yl)-1,4-bis(4-methylphenyl)-dihydropyrrolo[3,2-b]pyrrole
- (35) 2,3,5-Tris(4-cyanophenyl)-1,4-bis(4-methylphenyl)-1,4-dihydropyrrolo[3,2-b]pyrrole
- (39) 2,5-Bis(4-cyanophenyl)-1,4-bis(4-methylphenyl)-3,6-bis(4-(pentafluoro- λ^6 -sulfanyl)phenyl)-1,4-dihydropyrrolo[3,2-b]pyrrole
- (41) 2,5-Bis(4-cyanophenyl)-1,4-bis(4-methylphenyl)-3,6-di(pyridin-3-yl)-1,4-dihydropyrrolo[3,2-b]pyrrole

Compounds 3 through 41 are not commercially available and thus were synthesized by Janiga et al. [54] and Krzeszewski et al. [55].

Human skin samples were acquired from the plastic surgical department at Odense Universitetshospital (Odense, Denmark). No informed consent from patients was obtained (Danish regulations consider human tissue left over from surgery as discarded material), and no personal data were collected.

3.2 Software and Equipment

For the two-photon absorption measurements a Spectra-Physics Mai-Tai DeepSee tunable laser, a Nikon TI Eclipse inverted microscope, and a Princeton Instruments SpectraPro 2150i monochromator with a Princeton Instruments Pixix 400 CCD camera were used for sample selection and recording of spectra. Control of the laser intensity was handled with a separate shutter, and an AA Optoelectronics MT110-B50A1.5-IR-HK infra-red acousto-optical tunable filter (AOTF) and MDS1C-B6-34-85.135 RF driver. The laser power was measured using a beamsplitter and a Thorlabs PM100D power meter.

Micro-Manager 1.4.15 [56] was used to control the microscope, laser, shutter and $1/2$ -wave plate. The data acquisition from the spectrofluorometer was done using Princeton Instruments Winspec/32 2.5.23, while MATLAB R2013a (Natick, Massachusetts, United States) was used for data analysis. The entire setup is illustrated schematically in Figure 3.1.

A large part of my project was to build an automated system capable of performing two-photon absorption measurements using an existing microscope setup described in [57]. The setup was initially build to be independent of a microscope. This setup, which involved an isolated cuvette sample holder incorporated in the light path of the Ti:Sapphire laser, worked very well for individual measurements at single wavelengths. Extended data acquisition from a range of over 30 wavelengths, however, would be too cumbersome to be feasible even for a single dye at a time. We therefore decided to upgrade the system to include a microscope with a motorized X-Y stage to allow rudimentary automation of data acquisition. The monochromator was connected to one of the output ports on the microscope via an optical fiber guide.

In order to more precisely control the incident laser power an AOTF was inserted in the light path. Since the response of the AOTF from changes in input acoustic amplitude can be described with a log function it is possible to obtain a high degree of control over the laser power entering the sample. In addition to the increased precision of power adjustment the AOTF also allowed for better filtering of the incident laser ensuring a highly monochromatic wave. The high degree of data reproducibility from this setup significantly reduced the absolute error of my measurements.

I wrote a script to automate the changing of well plate position, and, by using the Andor camera connected to the microscope and computer as a controller, I was

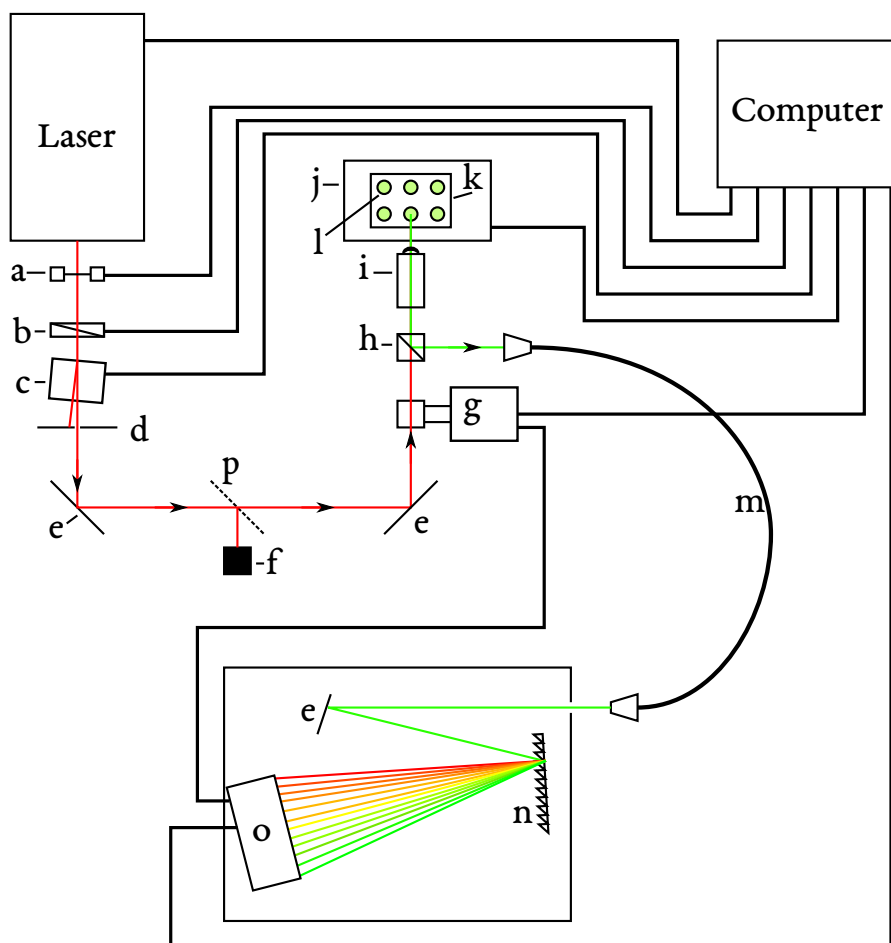


Figure 3.1: Schematic of our custom-made 2-photon spectrofluorometer. The red line is the tunable laser output. The green line is the fluorescence signal from the sample dye. *a*) shutter; *b*) $1/2$ -wave plate; *c*) AOTF; *d*) pinhole; *e*) mirrors; *f*) power meter; *g*) secondary camera; *h*) bandpass filter; *i*) objective; *j*) motorized X-Y stage; *k*) well plate; *l*) sample well; *m*) optical fiber guide; *n*) diffraction grating; *o*) primary camera; *p*) glass beam splitter.

able to both automate the cycling of well plate positions and acquisition of data from each position. In the end, I had created two scripts that could handle data collection and saving the data, changing wavelength of the laser, reconfiguring the AOTF, and moving the sample stage (see sections 3.2.1 and 3.2.1 for brief documentation and Appendix C.1 for source code). This allowed me to leave the system collection spectral data from up to 8 samples for 4 h to 10 h completely unsupervised and with a much reduced risk of human errors.

Because many of the dyes could only be dissolved in dichloromethane we in-

vested in a quartz 96-well plate and special fluorinated rubber sheets. Together with a custom-built well plate holder, with an aluminum lid, this enabled us to adequately seal the highly uniform wells and almost completely eliminate evaporation, further reducing sources of error.

3.2.1 Automation Scripts

To minimize uncertainties with respect to sample handling and measurements as well as simplifying the process of performing two-photon fluorescence spectrometry, I wrote several Beanshell-scripts in micro-manager as well as some VBScripts in Winspec/32. The following is a brief documentation of the most important scripts in this regard. All scripts can be found in Appendix C.1.

autoAOTF.bsh

The fundamental script is “autoAOTF.bsh”, which controls the laser, microscope stage (Figure 3.1 j), AOTF (c) and secondary camera (g). The script starts with a few dialogs that require user interaction. The purpose is to remind the user to check specific variable and to establish whether the system is to shut down automatically after the script is done. It will also make sure to turn on the laser if this has not been done previously.

When the initialization is complete the laser will be tuned to the first wavelength specified in the interval set by the user followed by tuning of the AOTF to control the laser power at the sample. The script reads sample positions from a pre-made list of sample coordinates and moves the microscope stage to the first position in the list. A command now opens the shutter (a) and triggers the secondary camera to capture an image causing it to send a fire signal to the primary camera (o) operated by the Princeton software. After a preset amount of time, the shutter will close, the stage moves to the next position in the position list, and another trigger-command is sent. After the protocol has been repeated at the last position the script will query the laser to tune to the next wavelength and adjust the AOTF accordingly. The laser is given a minute to stabilize at the new wavelength, and then the capturing process starts over for each sample position.

The script can operate with an arbitrary number of samples and any number of wavelengths within the physical capabilities of the laser and AOTF as long as the step size between the wavelengths are no smaller than 10 nm. This lower limit is not caused by neither the system nor the script, but merely stems from the fact that the reference values we are using has this step size.

auto.VBS

The Winspec/32 software was also automated in order to minimize the need for user interaction and awareness during spectral collection. This was accomplished using the script “auto.VBS.” It handles all data collection and storage of the spectral

data files. This script is more low-tech than the previous since it requires direct editing of variables inside the script for each execution.

When executed, the script will set a lot of data collection parameters such as integration time, spatial sensitivity, number of accumulations, and number of spectra to collect. It will also define the file path and name and set the primary camera to externally synced. The external sync allows the camera to be controlled by an external trigger which will be sent from the secondary camera once the laser, AOTF, and microscope are all at the appropriate positions/wavelengths. When the primary camera receives a trigger signal it will begin collection of light from the sample for the set integration time. Once done, the software saves the data and awaits a new trigger signal.

3.3 2-photon Absorption Cross-section Measurements

Absorbance measurements were conducted on a PerkinElmer (Waltham, Massachusetts, United States) Lambda 35 spectrophotometer using PerkinElmer UV Winlab 2.85.04 software for data acquisition. Fluorescence spectra for calculating quantum yield were obtained from an ISS ChronosFD (Champaign, Illinois, United States) spectrofluorometer controlled by ISS Vinci2 version 2.

3.3.1 Data Acquisition

Each dye was transferred to a spectrophotometer for absorbance measurements in order to determine maximum excitation wavelengths and calculate concentrations of the individual dye samples. Afterwards the dyes were transferred to a spectrofluorometer to obtain fluorescence spectra which would be used to determine maximum emission wavelengths and calculate quantum yield.

The dyes were then transferred to individual wells (Figure 3.1 l) in the well-plate (k) mounted on the motorized microscope stage (j). Each dye was exposed to laser radiation at different wavelengths in the range 700 nm to 1020 nm, and the fluorescence light was collected by the objective (i) and sent to a spectrofluorometer (n+o) through an optical fiber (m). The laser power was monitored using a power meter (f), which registers the fraction of the light diverted by the beam splitter (p), for each wavelength and the corresponding fluorescence spectrum recorded. The two-photon fluorescence spectra would be recorded between 3 and 5 times for each wavelength over the course of a few days.

When all data had been collected, it was converted to pure text files and read into MATLAB (see code in appendix C.2 and short explanation below) in order to calculate the 2-photon absorption cross-sections of each dye using the reference data supplied in [19].

3.3.2 Data Analysis

The data analysis was handled using two different Matlab scripts: “concentration.m” and “twopa.m”. *concentration.m* is a function that calculates the concentration of a sample by analyzing the one-photon absorption data to find the maximum absorption and then divides it with the molar extinction coefficient.

twopa.m

This script loads the one-photon and two-photon fluorescence spectra of each sample and a corresponding reference at a specific excitation wavelength. First, it plots the two-photon fluorescence spectra of the sample and reference together for comparison. Then it calculates the fractional quantum yield of the sample and reference at the wavelength where the two are to be compared (the wavelength is set manually). It then calls the *concentration.m*-function to calculate the concentration of the sample and reference and then uses all the above values to calculate the absolute two-photon absorption cross section of the sample at the specified excitation wavelength.

The script is set up to automatically load all sample and reference spectra, one excitation wavelength at a time, in order to concatenate the results into an absorption cross section spectrum. The results are plotted and saved to a text file for easy retrieval.

To collect the spectral results from different experimental runs, a script called “twopacollect.m” was designed to quickly load the results from “twopa.m” and produce plots and tabular data files for each dye.

3.4 Sample Preparation

Upon arrival in the lab, the skin was thoroughly cleaned with ethanol, and adipose tissue was carefully removed from the dermis layer. The adipectomied skin was cleaned with ethanol on the dermis side and cut into square pieces of ~8 mm side length before being further processed.

The individual skin samples were transferred to a petri dish filled with a 4 % formaldehyde solution and left overnight to fixate the tissue. After fixing, the samples were rinsed 2 · 15 min in PBS buffer.

Samples to be frozen were transferred to a container filled with Tissue-Tek O.C.T. Compound and, one at a time, immersed for 1 min into an isopentane bath cooled using liquid nitrogen. The frozen samples were stored in a -80°C freezer until use.

Skin samples would be cut into thin sections of $20\ \mu\text{m}$ in a cryotome. Sections were cut so that all layers of the skin would be present in each sections. The sample mount would be cooled to -20°C . Some skin samples would not be fixed prior to freezing. In that case, the frozen sections were fixed for 20 min at -20°C in

methanol and afterwards rinsed 3 · 5 min in PBS buffer with 1 % Bovine Serum Albumin which serves as a blocking agent.

After rinsing, samples were permeabilized with 0.5 % Triton X-100 in PBS buffer for 15 min and rinsed again as before. The primary anti-bodies were then applied to the sections for at least 1 h in a humid box at RT before being removed and the samples rinsed again.

The secondary anti-bodies were applied for the same amount of time in a dark, humid box and rinsed before excess fluid was carefully removed. 20 μ l to 40 μ l of mounting medium was applied to the sections and coverslips placed on the microscope slides to cure overnight in a dark environment.

3.5 STED Microscopy

The STED images were obtained on a Leica TCS SP8 (Manheim, Germany) inverted stage microscope fitted with a Leica STED module, a White Light Laser, and a HCX PL APO 100x/1.40 oil immersion objective. The entire setup is controlled by the LAS AF software which also handles image acquisition. Image post-processing was done in SVI Huygens Professional (Hilversum, The Netherlands) and Fiji [58].

A supercontinuum, or white light laser (WLL) produce a coherent light with a uniform and continuous spectrum spanning two hundred nanometers (470 nm to 670 nm) resulting in a white light. Coupled with an AOTF and an acousto-optical beam splitter (AOBS) it is possible to filter out several distinct wavelengths in this spectrum.

For optimal STED microscopy an objective with a refractive index of 1.518 is necessary. Different mounting media were used to determine the optimal compound for sample imaging and preservation

To obtain super-resolution images careful tuning of both excitation and depletion laser power, as well as detector gating, is important. Auto-fluorescence in the sample can sometimes be excited by the depletion laser, and the absorption of the depletion laser in the sample can lead to excessive heat generation and subsequent explosive expansion in the sample.

Results and Discussion

4.1 Two-Photon Absorption Cross Sections

From my measurements of the fluorescence spectral intensity of different fluorophores at various wavelengths, I was able to calculate the two-photon absorption cross section using fluorescein as a standard reference. Each data point is the average value from several measurements, and the error bars indicate the standard deviations for the associated data point. Numerical data for the spectra is located in Appendix B.

For the two commercial dyes, Abberior Star (AS) 440SX and 488, the results show a clear distinction, as can be seen in Figure 4.1.

The AS 440SX (blue) starts out with a low absorption up to about 750 nm, and then increases steadily until it reaches a relatively stable plateau at 820 nm to 910 nm before it declines to a complete zero. AS 488, on the other hand, has a very high absorption in the 700 nm to 800 nm range, drops off to a minimum at 860 nm, and reaches a local maximum 950 nm before steadily decreasing in absorption.

The very high absorption cross section of AS 488 at 700 nm combined with the sharp decline to a plateau at 720 nm indicates that the absorption cross section of the AS 488 is even higher below 700 nm. If the spectral profile is compared to that of Rhodamine 6G, however, it is evident that they are fairly similar in both profile and magnitude over the measured range [19]. This is true also for absorbance spectra of the two where the main difference is a 30 nm shift in absorption maximum [19]. Indeed the AS 488 is part of the rhodamine family of dyes [59]. These facts give a strong indication that 700 nm is actually the spectral location of the two-photon absorption peak. The AS 440SX seems very stable from 700 nm to 750 nm with a cross section of about 14 GM and has a spectral profile and absorption magnitude comparable Coumarin 540A and 485, with the notable difference that the absorption cross section of AS 440SX is shifted towards higher wavelengths when compared to

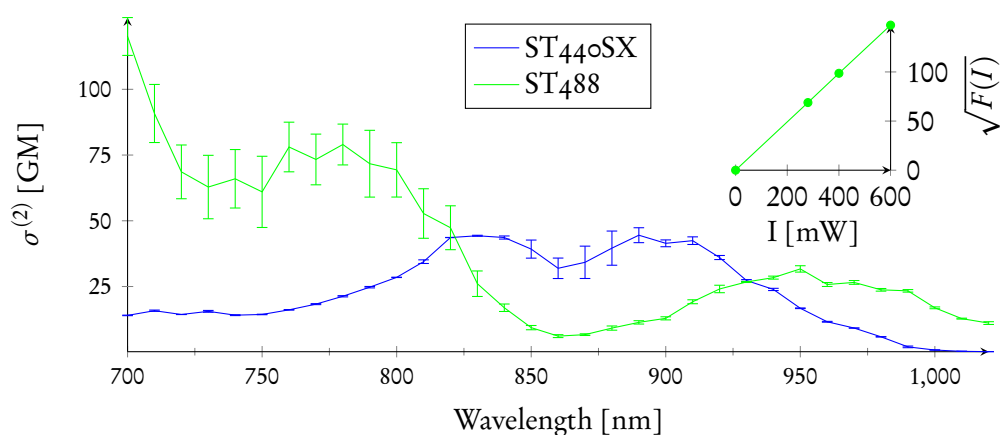


Figure 4.1: The calculated two-photon absorption cross section of Abberior Star 440SX and Abberior Star 488. Inset shows square root of the fluorescence signal of the AS 488 at 700 nm excitation as a function of the laser power measured. The quadratic relationship between F and I proves that we are in the two-photon regime.

either of the two Coumarins mentioned in [19]. Like for the AS 488, the AS 440SX is related to Coumarin dyes [60] which gives an indication that the cross sectional value at 700 nm is actually a local minimum.

It is important to note that the cross sectional values of AS 488 at 700 nm is not unreasonably high. Plotting the square root of the absolute fluorescence signal of AS 488, when excited at 700 nm, as a function of the laser power reveals that the signal scales with the square of the laser power as would be expected from pure two-photon absorption (Figure 4.1, inset).

These features of the absorption spectra make the two dyes very suitable for two-photon, two-color microscopy, since they are easily excited separately. More so than for one-photon excitation where it is necessary to excite below 450 nm and above 500 nm to properly separate the two as can be seen in Figure 4.2. The ideal excitation wavelengths for TPEM with these dyes would be either <760 nm and 870 nm or 870 nm and >1000 nm.

Indeed imaging a sample, stained with these two dyes, at 870 nm and 1010 nm gave a very clear distinction between the two dyes and a significant reduction in channel crosstalk as can be seen in Figure 4.3. However, just as I was not able to properly excite AS 440SX separately with the confocal microscope at 458 nm it was not possible to separately excite AS 488 at any wavelength between 700 nm and 760 nm. This reversed dye separation impediment between confocal and TPEM suggests that having both technologies integrated in the same setup with the ability to choose between both of them for each imaging channel would yield very high quality micrographs.

Moving on to the two-photon absorption cross sections of the novel compounds

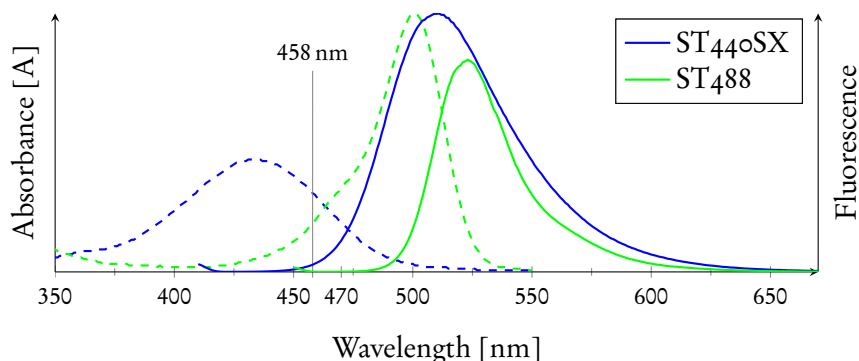


Figure 4.2: The measured one-photon absorption (dashed) and fluorescence (solid) of Abberior Star 440SX and Abberior Star 488.

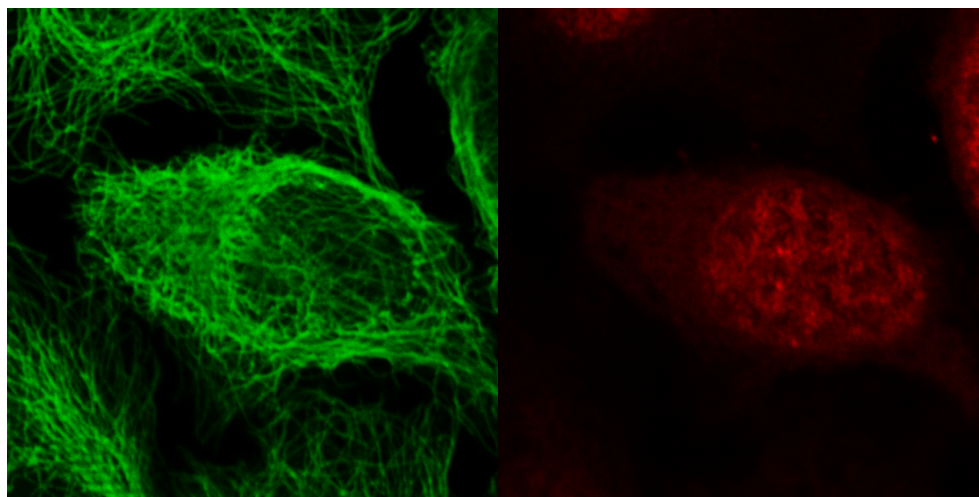


Figure 4.3: Two-color imaging of cell culture sample stained Abberior Star 440SX (actin filaments, green) excited at 860 nm and Abberior Star 488 (nucleus, red) at 1010 nm using TPTEM. Image size: $\sim 60 \mu\text{m} \cdot 60 \mu\text{m}$ ($1024 \cdot 1024$ pixels).

3–41 there is a clear tendency for the dyes to absorb better in the NIR range of light, especially at 700 nm to 750 nm. From Figure 4.4 it is clear that compound 6 has very high cross section in the 700 nm to 750 nm range. Compounds 4, 7, and 10 still has cross sections above 150 GM. In comparison, fluorescein has a maximum cross sectional value of ~ 65 GM [19]. However, compound 6 show a cross sectional value of about 1700 GM, several times larger than the other three compounds.

In Figure 4.5, compound 9 shows the highest absorption cross section with a maximum close to 500 GM, twice the magnitude of any of the compounds 5, 8, 11, and 3. Compound 5 has the lowest cross section of all the tested dyes with a

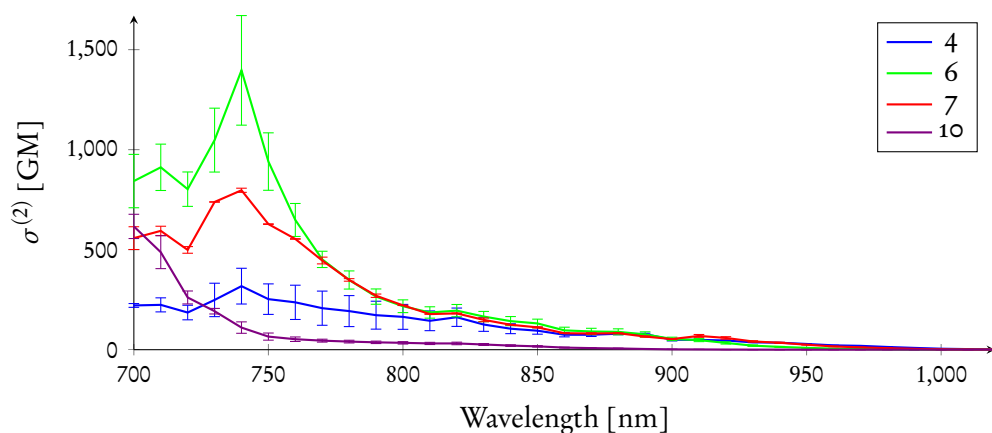


Figure 4.4: The calculated two-photon absorption cross sections of compounds 4, 6, 7 and 10.

maximum of 10 GM while the other three have maximum values between 40 GM and 200 GM.

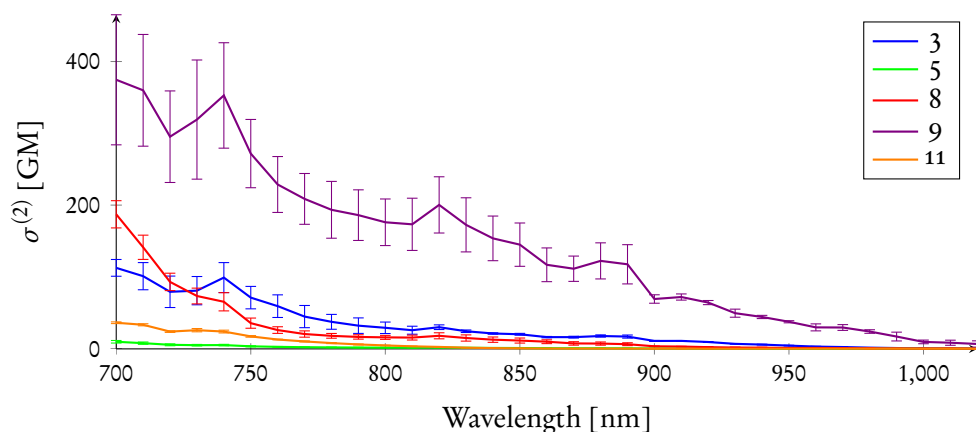


Figure 4.5: The calculated two-photon absorption cross sections of compounds 3, 5, 8, 9, and 8.

Lastly, Figure 4.6 show that compounds 26, 35, 39, and 41 all have a relatively high absorption cross section while compound 25 exhibits an absorption on par with fluorescein.

From Figures 4.4, 4.5, and 4.6 it is clear that the best dyes are compounds 6 and 26 which both have an absorption cross section well above 800 GM in the 700 nm to 720 nm range. Interestingly, compounds 26, 35, 39, and 41 all show a cross section above 350 GM while the closely related compound 25 show an absorption of ~ 50 GM. The compounds 7, 9, and 10 also show an absorption in

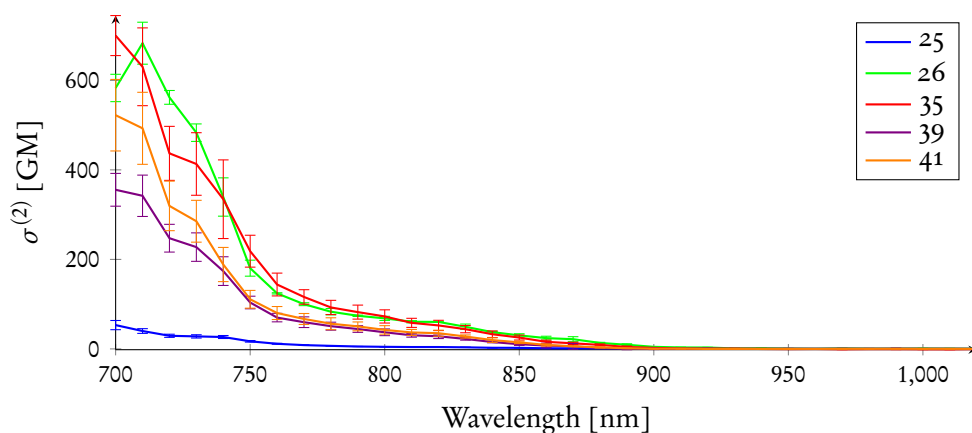


Figure 4.6: The calculated two-photon absorption cross sections of compounds 25, 26, 35, 39, and 41.

the order of 400 GM. While the results are generally good most of these novel dyes unfortunately have their peak absorption in the near-infrared range. This makes it extremely difficult to separate them spectrally from each other, but some of them, particularly compounds 6, 26, 35, 39, and 41 definitely show promise as two-photon absorbing fluorophores.

Most of the dyes measured show reasonable standard deviations, with the notable exception of compound 9 and, to a lesser extent, compounds 35 and 41. The seemingly stable correlation between cross sectional average value and standard deviation for these compounds could indicate that I am dealing with an instrumental error. The spectra of these dyes were all measured before the system was upgraded with a new quartz well plate and an AOTF, both of which are relatively new to the system. The spectra of the two Abberior dyes were all measured after these two upgrades, and indeed we see a much lower standard deviation for these spectra overall.

The physical limitations of our two-photon spectrofluorometer setup means that I was not able to probe the two-photon absorption of the dyes below 700 nm, but given that all of the novel dyes from [54] and [55] exhibit increasing absorption at decreasing wavelength it is reasonable to assume that their peak absorption lies in the 600 nm to 700 nm range. This has been supported by an unpublished theoretically calculated two-photon absorption cross section spectrum of one of the novel dyes (Jacob Kongsted, personal communication, december 2014).

4.2 STED Microscopy

During this project, I attempted to optimize the process of preparing samples for STED microscopy as well as the process of acquiring the highest quality image data

possible. This meant preparing skin samples while tweaking different parameters: fixation time, fixative, storage and sectioning temperature, incubation times and temperatures for permeabilization, staining with primary and secondary anti-bodies, and the concentrations of these solutions.

Because STED microscopy is still a very new technology there is large degree of trial and error involved in this process. The behavior and stability of fluorophores, and tissue in general, during stimulated emission has not been extensively studied yet. This is further complicated by imaging in thick tissue samples, which is inherently more difficult than thin cell culture smears, because of the increased scattering and phase shift induced by changes in refractive index in different cell structures.

In order to properly gauge the advantage gained when enabling STED it is crucial to acquire a confocal microscopic image of the chosen sample region beforehand. Parameters such as line or frame accumulation and averaging as well as pixel size, scanner speed, and laser power all had to be tweaked before we started the image acquisition. For high quality images, I would usually set the microscope to a scanner speed of 1400 Hz with 8 times line accumulation. The optimum laser intensity varied a great deal from sample to sample. To evenly compare the two technologies, pixel size is also of great importance. Our system was optimized for a pixel size of about 15 nm. The acquired image data from confocal microscopy would typically look like Figure 4.7 (left). The contrast, and thus level of detail, can be greatly enhanced by using a deconvolution algorithm. This was performed with the Huygens post-processing software supplied with the STED microscope system. The result of deconvoluting a confocal micrograph is shown in Figure 4.7 (right).

Since STED microscopy relies on two lasers working in tandem it is crucial that these are properly aligned before proceeding with image acquisition. The deexcitation of fluorophores by stimulated emission decreases the available fluorescence signal considerably, thus requiring a larger excitation laser intensity. Typically, the laser power is set to twice the power used for confocal microscopy. When comparison between STED and non-STED is needed, acquisition parameters such as line accumulation and scanner speed has to be identical between the two acquisitions. In my experiments, the STED laser intensity would usually be set to 30%. Figure 4.8 (left) shows an example of a STED micrograph. The lowered fluorescence signal results in a noisy-looking image, which is often unconvincing in regards to the benefits of using STED. Deconvoluting the image substantially enhances the level of detail and overall contrast of the STED micrograph (Figure 4.8, right).

A useful tool in quantifying the increase in resolution is comparing the point spread function of STED and confocal microscopy. In Figure 4.9, I have shown the full-size deconvoluted image of a sample recorded with and without STED in Figures 4.7 and 4.8, respectively. Together with these images, I have made a zoom of a specific area and plotted the fluorescence intensity of the profile highlighted by a white line going through the zooms. From these zooms it is evident that what would normally have been perceived as one large fluorescent spot in confocal microscopy without STED is now shown to actually be a more complex aggregate of

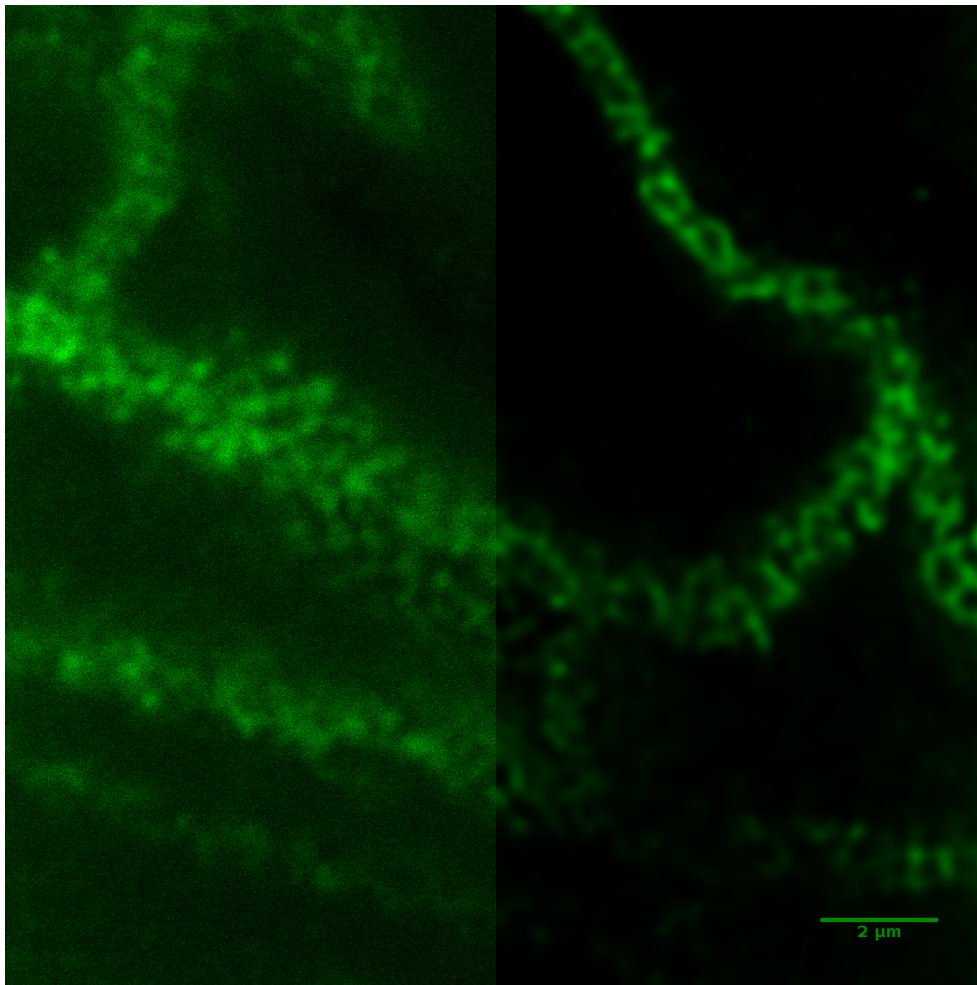


Figure 4.7: An overlay comparison of difference between contrast and level of detail before (left) and after (right) deconvolution in an image obtained through confocal microscopy. The sample being imaged is part of the epidermis of human skin. Abberior Star 488 has been used to tag the tight junction protein claudin-1.

smaller fluorescent spots sitting very close to each other. The point spread function is estimated to be around 100 nm, which is a good start for imaging in tissue. Looking at Figures 4.7 (right) and 4.8 (right) we also see what could be interpreted as clustering on the intracellular side of the apposing membranes. Because claudin-1 is a transmembrane protein that connects apposing membranes and bring them into close contact, forming a seal at the point of contact it is very likely that the binding site for the anti-body is located in the cytoplasmic part of the protein. This will separate the fluorescent spots on either side rather than having them lined up in the middle like pearls on a string.

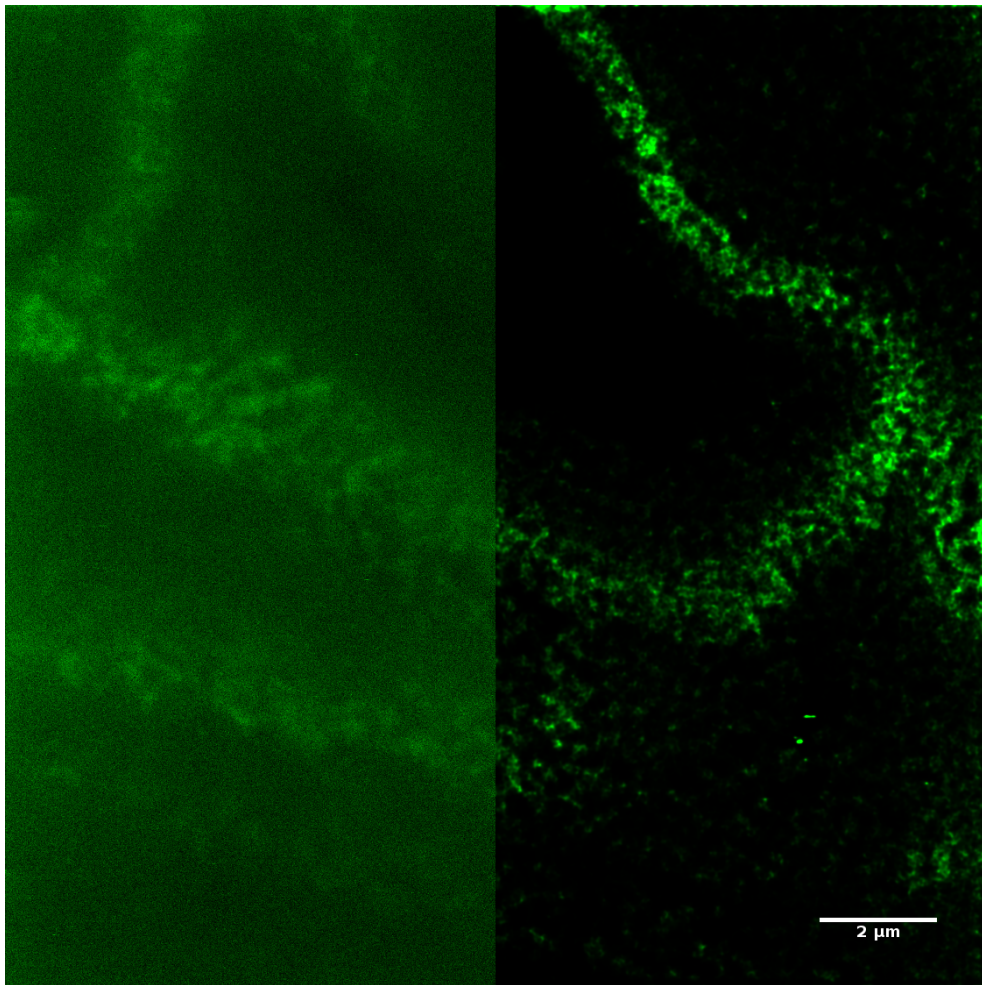


Figure 4.8: The region in Figure 4.7 imaged using STED microscopy. This figure shows an overlay comparison of the difference between the contrast and detail available before (left) and after (right) deconvolution.

To highlight the difference in quality between TEM and STED, I have included a typical electron micrograph of epidermal tight junctions, from the paper by Furuse et al. [16], in Figure 4.10. It is clear that this image has an outstanding resolution, with the bar in (d) having a length of a mere 100 nm. However, the rather unspecific contrast generation of electron microscopy means that researchers have to rely mostly on sample density to interpret the image. The ultrathin sections also do not allow for three-dimensional imaging as is possible with confocal, two-photon, and STED microscopy where the samples typically are several micrometers thick. In most cases, as it is in this case, the sample has been stained with a solution of dense molecules to provide higher contrast. Since they are rather small they can flow into very small crevices between cells and help visualize the membrane

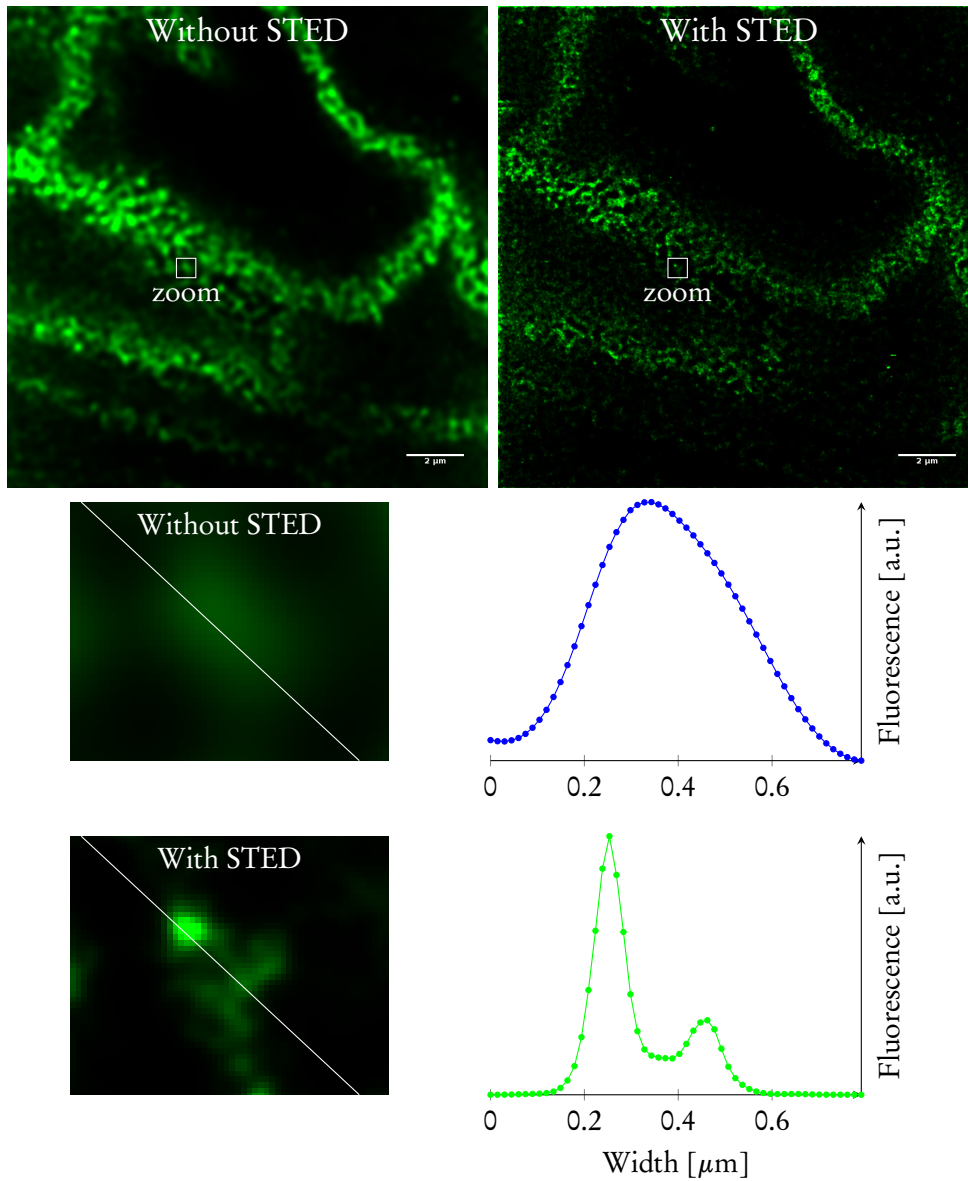


Figure 4.9: Effective point spread function of the confocal (blue) and STED (green) microscopy techniques measured on the same point-like object in the deconvoluted images of Figures 4.7 and 4.8, respectively. The top row features the unzoned micrographs while the second and third row to the right features a profile plot of the intensity along the white line in the image to the left. Second and third row correspond to confocal without and with STED, respectively.

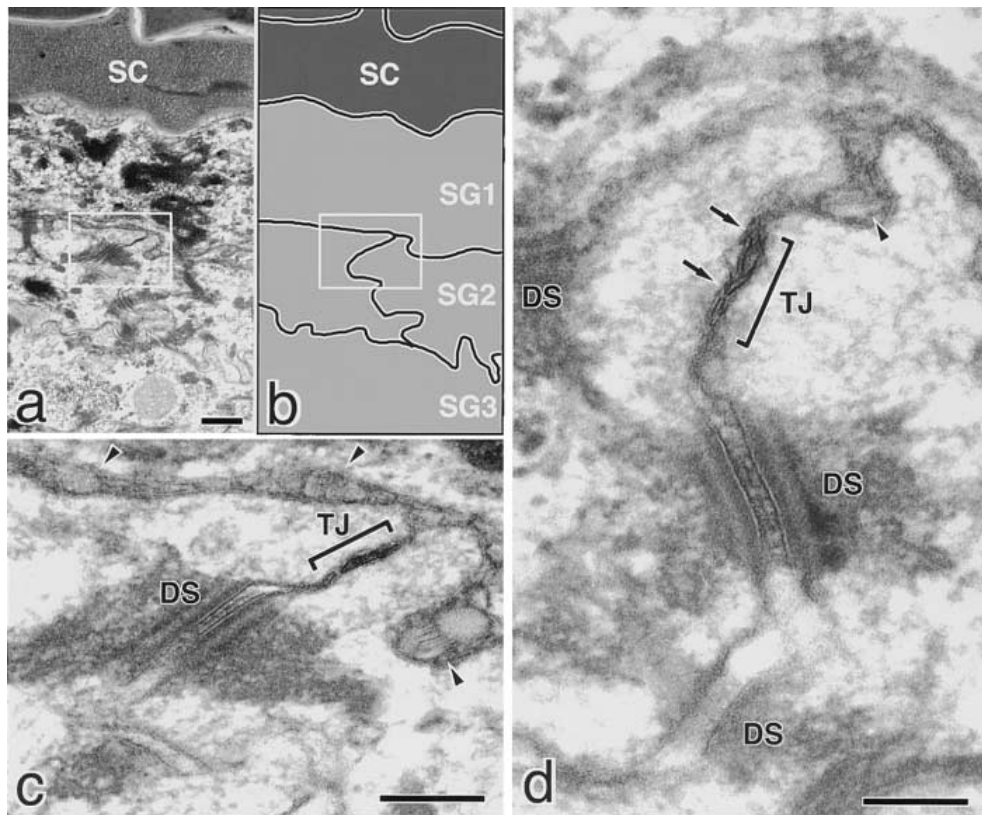


Figure 4.10: “Ultrathin section electron microscopic images of wild-type epidermis. (a and b) Low power electron micrograph (a) of the stratum corneum (SC) and the first through third layers of stratum granulosum (SG₁, SG₂, and SG₃) and a corresponding schematic drawing (b). (c) A boxed area in a and b where occludin was expected to be concentrated was enlarged. Typical TJ (TJ) was detected just above desmosome (DS). (d) Another example of the TJ–desmosome complex observed at the most apical region of the lateral membranes of granular cells in the second layer. Lipid lamellar bodies (arrowheads). Kissing points of TJs (arrows). Bars: (a) 400 nm; (c) 200 nm; (d) 100 nm.” Figure and caption is from [16, Fig. 5]

borders. Regions that are shown to be extra dark has thus been hypothesized to be the location of these tight junctions, and the thickness of the dark streak has generally been used to define the distance between the apposing membranes.

Figure 4.11 illustrates the applicability of STED in the generation of 3D images to better visualize the spatial distribution of fluorophores in samples. In this image, which has the stratum corneum beginning in the right-hand part, we see a high degree of co-localization between claudin-1 and desmoglein-1 in the lower

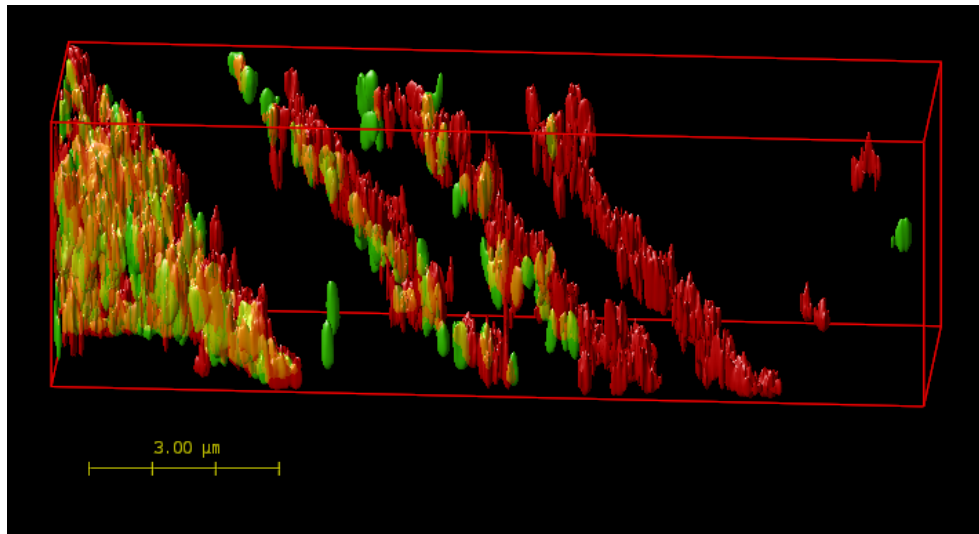


Figure 4.11: 3D image generated from a deconvoluted Z stack of a human epidermal tissue sample stained against claudin-1 (green) and desmoglein-1 (red). It is clear that the proteins are arranged in layers that continuously decrease in separation, and that claudin get scarcer as we approach stratum corneum on the right.

layers of the epidermis. However, as we continue towards the stratum corneum, there is a substantial decrease in claudin-1 while desmoglein-1 continue to be well-represented. This confirms prior work in the field [13, 16] where claudin-1 is shown to be predominantly located in the strata below stratum corneum. Desmoglein-1, which is a structural constituent of both desmosomes and corneodesmosomes is found throughout the tissue.

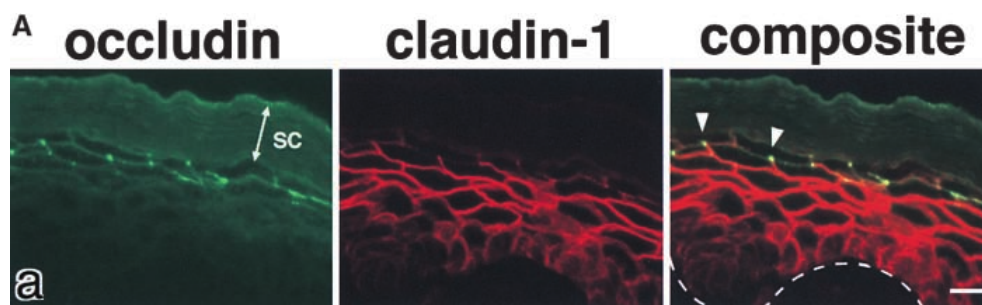


Figure 4.12: Confocal micrograph of occludin (green, left) and claudin-1 (red, middle) in mice skin and a composite of the two images (right). This image shows that the spatial distribution of claudin-1 is delimited by the stratum corneum, but otherwise present throughout the tissue. Bars, 20 μm. Image adapted from [16]

Figure 4.12 illustrates the standard definition achievable with confocal microscopy. The middle image shows a micrograph labeled against claudin-1, and we see the same degree of labeling as we do in e.g. Figure 4.8. Here, there is a clearly noticeable difference in the level of detail, compared to the STED images shown above, underlining the usefulness of this new technology.

4.2.1 Photostability

In order to determine how prone the dyes are to bleaching, I recorded a series of time-lapse microscopy images and measured quantified the mean photon count in a bright area of each series. The results are shown for confocal and STED microscopy in Figure 4.13. To gain a better understanding of how STED microscopy affects bleaching, I recorded both a time-lapse image with the excitation laser set to the high output typically needed for STED imaging without the STED laser activated for both Abberior Star dyes as well as a time-lapse with regular STED microscopy settings.

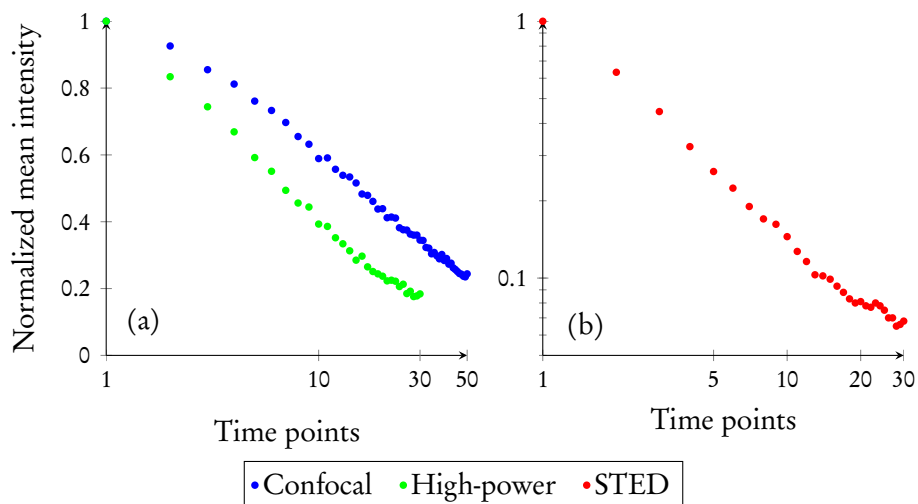


Figure 4.13: Plots of the normalized intensity at selected areas over time in tissue stained with Abberior Star 440SX. (a) is semilogarithmic; (b) is doublelogarithmic. Confocal (blue) is excited with a laser intensity suitable for regular confocal microscopy; High-power (green) is excited with a laser intensity usually reserved for STED imaging; STED (red) is excited with the same laser intensity as high-power, but in addition the STED laser is also activated.

What can be seen is that for Abberior Star 440SX, STED imaging reduces the fluorescence signal with a rate that can be fitted as a power law (Figure 4.13(b)) while disabling STED results in exponential decay. For normal confocal operation the decay rate is slightly lower than the high-power exponential decay. The power

law relation would not be possible as long as the transition rates between each molecular state are linear. Therefore it is likely that, given an extended time-lapse of perhaps 100 or even 200 frames would have revealed the true exponential nature of the response.

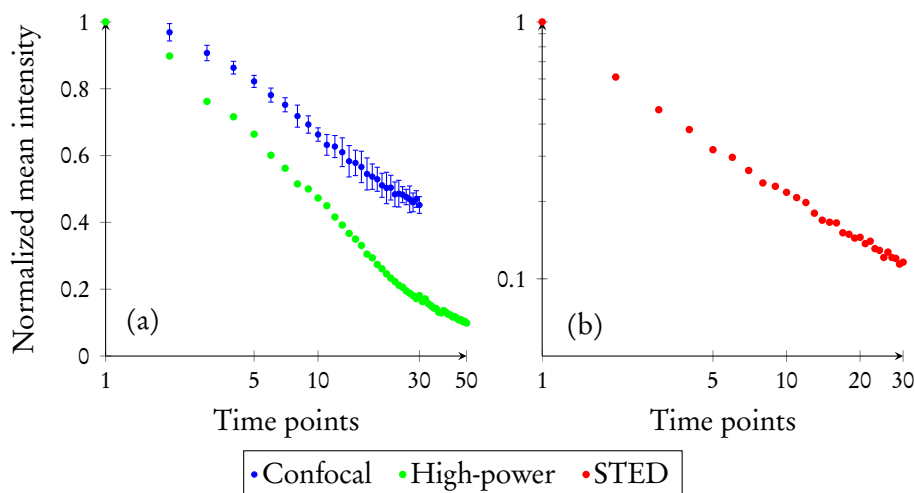


Figure 4.14: Plots of the normalized intensity at selected areas over time in tissue stained with Abberior Star 488. (a) is semilogarithmic; (b) is double-logarithmic. Confocal (blue) is excited with a laser intensity suitable for regular confocal microscopy; High-power (green) is excited with a laser intensity usually reserved for STED imaging; STED (red) is excited with the same laser intensity as high-power, but in addition, the STED laser is also activated.

The photostability of Abberior Star 488 under normal confocal microscopy conditions is slightly better than that of AS 440SX. To further demonstrate the reproducibility, I have made several measurements for the case of regular confocal imaging with identical settings, which produce only very small deviations. For high-power illumination the two dyes actually have almost completely equal rate of bleaching. Turning on the STED laser makes a significant difference, however. Where the difference in intensity between the two dyes for normal confocal operation was about 23 % after 30 frames of exposure, repeating the experiment with the STED laser activated resulted in the Abberior Star 440SX being 41 % less intense after 30 frames. The Abberior Star 488 is thus a much more suitable STED microscopy dye.

The explanation for the increased bleaching during STED microscopy might prove to be found in the triplet state. Since absorption and emission by interaction with a photon from an electromagnetic field differs only in the transition direction, it is plausible that when the AS 440SX ends in the T_1 triplet state, the STED laser excites it up into a higher triplet state, giving the molecule enough energy to cause

photochemical changes that ultimately destroys its fluorescence ability.

Conclusion and Perspective

During my project, I have succeeded in creating a fully operational and almost completely automatic two-photon spectrofluorometer capable of measuring a theoretical maximum of 96 unique dyes in a single run and perform spectral measurements of each dye in the full range of 700 nm to 1020 nm. The system has a very low instrumental error and is relatively easy to operate.

By combining the data acquired from the two-photon spectrofluorometer with absorbance and fluorescence measurement data, I successfully created a script in Matlab that fully quantifies the two-photon absorption cross section by calculating the value for a specific wavelength using already available two-photon absorption cross section of commercial dyes as reference data. Using this system, I determined the two-photon absorption cross section of 14 newly developed dyes, and the calculated cross section spectra were used to ascertain the efficacy of the dyes in TPDM. The results of my analyses were published in [54] and [55] where some of the dyes being reported were shown to have very promising two-photon properties when compared to traditional dyes [19]. Indeed, many of the dyes show cross sections well above 200 GM in the 700 nm to 720 nm range, and compound 6, in particular, has a two-photon absorption of 1000 GM at 740 nm, a generally impressive magnitude. The two commercial dyes, Abberior Star 440SX and 488, also showed between good and high two-photon absorption with the AS 440SX being comparable to Coumarin 485 in spectral profile and magnitude while the AS 488 is similar to rhodamine 6G in magnitude and spectral profile. For the AS 440SX there is a significant shift towards higher wavelengths in the two-photon absorption cross section compared to the Coumarins while for the AS 488 the only noticeable shift is in the absorbance spectrum.

Even though the current setup has a very impressive degree of reproducibility and runs close to fully automated it is important to remember that the two-photon spectrofluorometer alone is not enough to calculate the two-photon absorption

cross section spectra. If the setup was retro-fitted with a light source capable of operating in an interval ranging from 300 nm and up to 700 nm it would then be possible to also measure the one-photon fluorescence spectrum on the same system which in the end would greatly reduce systematic errors. It is not sensible, however, to add functionality *ad infinitum* since evaporation of dye solvents becomes an increasing problem with increased time consumption per experiment. Of course it is also relevant to consider decreasing integration time during acquisition of two-photon fluorescence spectra.

Based on the results from my two-photon absorption cross section calculations, I predicted that Abberior Star 440SX and 488 would exhibit a larger degree of spectral separation of excitation at 860 nm and 1010 nm, respectively. Combining TPTEM with STED promise to yield fluorescence micrographs with both superior depth penetration and lateral resolution. So far this has been demonstrated, but spectral unmixing was used to improve the color separation [61]. In our lab, a similar setup is currently under construction and is expected to be finished and running in a few months time, at which point we expect to provide two-color two-photon STED images without the aid of spectral unmixing.

Using the Leica STED microscope on tissue already show very promising results. I was able to create the first ever STED image of a skin tissue sample and in the process achieve a lateral resolution of 65 nm to 100 nm, which is up to four times smaller than comparable regular confocal resolution conditions. From the micrographs acquired using confocal and STED microscopy it is also evident that the signal to noise ratio can be increased significantly post-acquisition by running the images through software capable of deconvolution such as the Huygens Professional software. This can turn a relatively grainy image into a high-quality image with very well-defined boundaries which gives access to previously obscured details and thus increases the potential for this technology even further.

Furthermore, I was able to acquire a 3D 2-color z-stack STED image which clearly show the differentiation between the tight junction protein claudin-1 and the desmosomal protein desmoglein-1 that has been reported by other researchers [16, 13, 12]. The high quality achievable when generating 3D images from the STED micrographs also give substantial merit to this technology. I was able to clearly show individual protein clusters lining the cell walls in an area where the sloping is very high. The potential for resolving cellular structures and pathways with dimension as low as 20 nm in three dimensions coupled with deep tissue penetration of TPTEM promise to bridge the gap between optical and electron microscopy.

A key problem to be aware of, when doing STED microscopy, is bleaching. It is well-known that fluorophores tend to bleach during prolonged exposure of the excitation laser light. But the STED laser tends to enhance this effect dramatically over relatively short time scales. This indicates that during the deexcitation pulse, in addition to stimulate emission of excited fluorophores, the STED laser pulse also excites the fluorophores which have ended in the T_1 state, into a higher triplet state, where the fluorophores might become stuck, loose an electron or undergo a chemical reaction that renders it non-fluorescent. This hypothesis would have

to be tested using theoretical calculations of the transition rate from T_1 to $T_{n>1}$ along with estimates of the transition rates for all the normal transitions involved in fluorescence. Comparing the theoretical estimates to the experimental data should provide the answer to this problem with relative ease.

Because of the very high intensity of the STED laser it is also necessary to carefully consider the power level used in STED imaging. On several occasions, I actually transferred enough energy into my samples that they exhibited explosive expansion in areas up to a few square micrometers. Though this was most likely due to absorption and non-radiative release of the build-up energy, this is still a serious matter that needs to be addressed properly in order to avoid destroying potentially precious samples.

In summary, the setup that we created is one of only a few in the world with such capabilities, and it really shows great promise for future applications. The feat of taking a high-quality superresolved image in biological tissue has not been done previously, and the results here also show that stimulated emission depletion in conjunction with two-photon excitation microscopy will soon become an invaluable tool.

Bibliography

- [1] Howard R. Petty. Fluorescence microscopy: Established and emerging methods, experimental strategies, and applications in immunology. *Microscopy Research and Technique*, 70(8):687–709, August 2007. ISSN 1059910X, 10970029. doi: 10.1002/jemt.20455. URL <http://doi.wiley.com/10.1002/jemt.20455>.
- [2] M. Minsky. Memoir on inventing the confocal scanning microscope. *Scanning*, 10(4):128–138, 1988. ISSN 01610457. doi: 10.1002/sca.4950100403. URL <http://doi.wiley.com/10.1002/sca.4950100403>.
- [3] W Denk, J. Strickler, and W. Webb. Two-photon laser scanning fluorescence microscopy. *Science*, 248(4951):73–76, April 1990. ISSN 0036-8075, 1095-9203. doi: 10.1126/science.2321027. URL <http://www.sciencemag.org/cgi/doi/10.1126/science.2321027>.
- [4] Fritjof Helmchen and Winfried Denk. Deep tissue two-photon microscopy. *Nature Methods*, 2(12):932–940, December 2005. ISSN 1548-7091, 1548-7105. doi: 10.1038/nmeth818. URL <http://www.nature.com/doi/10.1038/nmeth818>.
- [5] E. Abbe. Beiträge zur Theorie des Mikroskops und der mikroskopischen Wahrnehmung: I. Die Construction von Mikroskopen auf Grund der Theorie. *Archiv für Mikroskopische Anatomie*, 9(1):413–418, December 1873. ISSN 0176-7364. doi: 10.1007/BF02956173. URL <http://link.springer.com/10.1007/BF02956173>.
- [6] E. Betzig, G. H. Patterson, R. Sougrat, O. W. Lindwasser, S. Olenych, J. S. Bonifacino, M. W. Davidson, J. Lippincott-Schwartz, and H. F. Hess. Imaging Intracellular Fluorescent Proteins at Nanometer Resolution. *Science*, 313(5793):1642–1645, September 2006. ISSN 0036-8075, 1095-9203. doi: 10.1126/science.

1127344. URL <http://www.sciencemag.org/cgi/doi/10.1126/science.1127344>.
- [7] M. G. L. Gustafsson. Nonlinear structured-illumination microscopy: Wide-field fluorescence imaging with theoretically unlimited resolution. *Proceedings of the National Academy of Sciences*, 102(37):13081–13086, September 2005. ISSN 0027-8424, 1091-6490. doi: 10.1073/pnas.0406877102. URL <http://www.pnas.org/cgi/doi/10.1073/pnas.0406877102>.
- [8] Michael J Rust, Mark Bates, and Xiaowei Zhuang. Sub-diffraction-limit imaging by stochastic optical reconstruction microscopy (STORM). *Nature Methods*, 3(10):793–796, October 2006. ISSN 1548-7091, 1548-7105. doi: 10.1038/nmeth929. URL <http://www.nature.com/doi/10.1038/nmeth929>.
- [9] Stefan W. Hell and Jan Wichmann. Breaking the diffraction resolution limit by stimulated emission: stimulated-emission-depletion fluorescence microscopy. *Optics Letters*, 19(11):780, June 1994. ISSN 0146-9592, 1539-4794. doi: 10.1364/OL.19.000780. URL <http://www.opticsinfobase.org/abstract.cfm?URI=ol-19-11-780>.
- [10] Mikhail Drobizhev, Nikolay S Makarov, Shane E Tillo, Thomas E Hughes, and Aleksander Rebane. Two-photon absorption properties of fluorescent proteins. *Nature Methods*, 8(5):393–399, May 2011. ISSN 1548-7091, 1548-7105. doi: 10.1038/nmeth.1596. URL <http://www.nature.com/doi/10.1038/nmeth.1596>.
- [11] Luis A. Bagatolli, Tiziana Parasassi, Gerardo D. Fidelio, and Enrico Gratton. A Model for the Interaction of 6-Lauroyl-2-(N,N-dimethylamino)naphthalene with Lipid Environments: Implications for Spectral Properties. *Photochemistry and Photobiology*, 70(4):557–564, October 1999. ISSN 0031-8655, 1751-1097. doi: 10.1111/j.1751-1097.1999.tb08251.x. URL <http://doi.wiley.com/10.1111/j.1751-1097.1999.tb08251.x>.
- [12] Ehrhardt Proksch, Johanna M. Brandner, and Jens-Michael Jensen. The skin: an indispensable barrier. *Experimental Dermatology*, 17(12):1063–1072, December 2008. ISSN 09066705, 16000625. doi: 10.1111/j.1600-0625.2008.00786.x. URL <http://doi.wiley.com/10.1111/j.1600-0625.2008.00786.x>.
- [13] Johanna M. Brandner, Marek Haftek, and Carien M. Niessen. Adherens Junctions, Desmosomes and Tight Junctions in Epidermal Barrier Function. *The Open Dermatology Journal*, 4(1):14–20, January 2010. ISSN 18743722. doi: 10.2174/1874372201004010014. URL <http://benthamopen.com/openaccess.php?todj/articles/V004/SI0001TODJ/14TODJ.htm>.
- [14] J.M. Brandner, S. Kief, E. Wladykowski, P. Houdek, and I. Moll. Tight Junction Proteins in the Skin. *Skin Pharmacology and Physiology*, 19(2):71–

- 77, 2006. ISSN 1660-5535, 1660-5527. doi: 10.1159/000091973. URL <http://www.karger.com/doi/10.1159/000091973>.
- [15] M. Furuse. Occludin: a novel integral membrane protein localizing at tight junctions. *The Journal of Cell Biology*, 123(6):1777–1788, December 1993. ISSN 0021-9525, 1540-8140. doi: 10.1083/jcb.123.6.1777. URL <http://www.jcb.org/cgi/doi/10.1083/jcb.123.6.1777>.
- [16] M. Furuse, M. Hata, K. Furuse, Y. Yoshida, A. Haratake, Y. Sugitani, T. Noda, A. Kubo, and S. Tsukita. Claudin-based tight junctions are crucial for the mammalian epidermal barrier: a lesson from claudin-1-deficient mice. *The Journal of Cell Biology*, 156(6):1099–1111, March 2002. ISSN 0021-9525, 1540-8140. doi: 10.1083/jcb.200110122. URL <http://www.jcb.org/cgi/doi/10.1083/jcb.200110122>.
- [17] J Brandner. Organization and formation of the tight junction system in human epidermis and cultured keratinocytes. *European Journal of Cell Biology*, 81(5): 253–263, May 2002. ISSN 01719335. doi: 10.1078/0171-9335-00244. URL <http://linkinghub.elsevier.com/retrieve/pii/S0171933504702289>.
- [18] Y. Yoshida, Kazumasa Morita, Akira Mizoguchi, Chizuka Ide, and Yoshiaki Miyachi. Altered expression of occludin and tight junction formation in psoriasis. *Archives of Dermatological Research*, 293(5):239–244, May 2001. ISSN 0340-3696, 1432-069X. doi: 10.1007/s004030100221. URL <http://link.springer.com/10.1007/s004030100221>.
- [19] Nikolay S. Makarov, Mikhail Drobizhev, and Aleksander Rebane. Two-photon absorption standards in the 550-1600 nm excitation wavelength range. *Optics Express*, 16(6):4029, March 2008. ISSN 1094-4087. doi: 10.1364/OE.16.004029. URL <http://www.opticsinfobase.org/abstract.cfm?URI=oe-16-6-4029>.
- [20] H. H. Jaffe and Albert L. Miller. The fates of electronic excitation energy. *Journal of Chemical Education*, 43(9):469, September 1966. ISSN 0021-9584, 1938-1328. doi: 10.1021/ed043p469. URL <http://pubs.acs.org/doi/abs/10.1021/ed043p469>.
- [21] Mordechai Bixon. Intramolecular Radiationless Transitions. *The Journal of Chemical Physics*, 48(2):715, 1968. ISSN 00219606. doi: 10.1063/1.1668703. URL <http://scitation.aip.org/content/aip/journal/jcp/48/2/10.1063/1.1668703>.
- [22] E. A. Gastilovich, N. V. Korol'kova, and V. G. Klimenko. Rate constants of nonradiative intersystem crossing transition $S_1(\pi\pi^*) \rightsquigarrow T_1(\pi\pi^*)$ in molecules of aromatic compounds with heteroatoms. *Optics and Spectroscopy*, 109(1):72–84, July 2010. ISSN 0030-400X, 1562-6911. doi:

- 10.1134/S0030400X10070131. URL <http://link.springer.com/10.1134/S0030400X10070131>.
- [23] Maria Göppert-Mayer. Über Elementarakte mit zwei Quantensprüngen. *Annalen der Physik*, 401(3):273–294, 1931. ISSN 00033804, 15213889. doi: 10.1002/andp.19314010303. URL <http://doi.wiley.com/10.1002/andp.19314010303>.
- [24] Robert W. Boyd. *Nonlinear optics*. Academic Press, Amsterdam ; Boston, 3rd ed edition, 2008. ISBN 9780123694706.
- [25] Barry R. Masters and Peter T. C. So, editors. *Handbook of biomedical nonlinear optical microscopy*. Oxford University Press, New York, 2008. ISBN 9780195162608.
- [26] Chris Xu and Watt W. Webb. Multiphoton Excitation of Molecular Fluorophores and Nonlinear Laser Microscopy. In Joseph R. Lakowicz, editor, *Topics in Fluorescence Spectroscopy*, pages 471–540. Springer US, Boston, MA, 2002. ISBN 978-0-306-45553-7, 978-0-306-47070-7. URL http://link.springer.com/10.1007/0-306-47070-5_11.
- [27] W. Kaiser and C. Garrett. Two-Photon Excitation in CaF_2 : Eu^{2+} . *Physical Review Letters*, 7(6):229–231, September 1961. ISSN 0031-9007. doi: 10.1103/PhysRevLett.7.229. URL <http://link.aps.org/doi/10.1103/PhysRevLett.7.229>.
- [28] A. E Siegman. *Lasers*. University Science Books, Mill Valley, Calif., 1986. ISBN 9780935702118 0935702113 0198557132 9780198557135 0685055957 9780685055953.
- [29] A. Einstein. Strahlungs-Emission und Absorption nach der Quantentheorie. *Deutsche Physikalische Gesellschaft*, 18:318–323, 1916.
- [30] A Einstein. Quantum theory of radiation. *PHYSIKALISCHE ZEITSCHRIFT*, 18:121–128, 1917.
- [31] A. Schawlow and C. Townes. Infrared and Optical Masers. *Physical Review*, 112(6):1940–1949, December 1958. ISSN 0031-899X, 1536-6065. doi: 10.1103/PhysRev.112.1940. URL <http://link.aps.org/doi/10.1103/PhysRev.112.1940>.
- [32] David Bardell. The Biologists' Forum: The invention of the microscope. *BIOS*, 75(2):78–84, May 2004. ISSN 0005-3155. doi: 10.1893/0005-3155(2004)75<78:TIO(TM)>2.0.CO;2. URL <http://www.bioone.org/doi/abs/10.1893/0005-3155%282004%2975%3C78%3ATIOTM%3E2.0.CO%3B2>.

- [33] R. W. Wijnaendts Resandt, H. J. B. Marsman, R. Kaplan, J. Davoust, E. H. K. Stelzer, and R. Stricker. Optical fluorescence microscopy in three dimensions: microtomoscopy. *Journal of Microscopy*, 138(1):29–34, April 1985. ISSN 00222720. doi: 10.1111/j.1365-2818.1985.tb02593.x. URL <http://doi.wiley.com/10.1111/j.1365-2818.1985.tb02593.x>.
- [34] V. Wilke. Optical scanning microscopy-The laser scan microscope. *Scanning*, 7(2):88–96, 1985. ISSN 01610457. doi: 10.1002/sca.4950070204. URL <http://doi.wiley.com/10.1002/sca.4950070204>.
- [35] J. G. White. An evaluation of confocal versus conventional imaging of biological structures by fluorescence light microscopy. *The Journal of Cell Biology*, 105(1):41–48, July 1987. ISSN 0021-9525, 1540-8140. doi: 10.1083/jcb.105.1.41. URL <http://www.jcb.org/cgi/doi/10.1083/jcb.105.1.41>.
- [36] Winfried Denk and Karel Svoboda. Photon Upmanship: Why Multiphoton Imaging Is More than a Gimmick. *Neuron*, 18(3):351–357, March 1997. ISSN 08966273. doi: 10.1016/S0896-6273(00)81237-4. URL <http://linkinghub.elsevier.com/retrieve/pii/S0896627300812374>.
- [37] B.R. Masters, P.T. So, and E. Gratton. Multiphoton excitation fluorescence microscopy and spectroscopy of in vivo human skin. *Biophysical Journal*, 72(6):2405–2412, June 1997. ISSN 00063495. doi: 10.1016/S0006-3495(97)78886-6. URL <http://linkinghub.elsevier.com/retrieve/pii/S0006349597788866>.
- [38] Michael W. Davidson and Mortimer Abramowitz. Optical Microscopy. In Joseph P. Hornak, editor, *Encyclopedia of Imaging Science and Technology*. John Wiley & Sons, Inc., Hoboken, NJ, USA, January 2002. ISBN 0471443395, 9780471443391. URL <http://doi.wiley.com/10.1002/0471443395.img074>.
- [39] C.E. Shannon. Communication In The Presence Of Noise. *Proceedings of the IEEE*, 86(2):447–457, February 1998. ISSN 0018-9219, 1558-2256. doi: 10.1109/JPROC.1998.659497. URL <http://ieeexplore.ieee.org/lpdocs/epic03/wrapper.htm?arnumber=659497>.
- [40] Stefan W Hell. Toward fluorescence nanoscopy. *Nature Biotechnology*, 21(11):1347–1355, November 2003. ISSN 1087-0156. doi: 10.1038/nbt895. URL <http://www.nature.com/doifinder/10.1038/nbt895>.
- [41] Lawrence F Drummy, Junyan Yang, and David C Martin. Low-voltage electron microscopy of polymer and organic molecular thin films. *Ultramicroscopy*, 99(4):247–256, June 2004. ISSN 03043991. doi: 10.1016/j.ultramic.2004.01.011. URL <http://linkinghub.elsevier.com/retrieve/pii/S0304399104000117>.

- [42] Marcus Dyba and Stefan Hell. Focal Spots of Size $\lambda/23$ Open Up Far-Field Fluorescence Microscopy at 33 nm Axial Resolution. *Physical Review Letters*, 88(16), April 2002. ISSN 0031-9007, 1079-7114. doi: 10.1103/PhysRevLett.88.163901. URL <http://link.aps.org/doi/10.1103/PhysRevLett.88.163901>.
- [43] Volker Westphal and Stefan Hell. Nanoscale Resolution in the Focal Plane of an Optical Microscope. *Physical Review Letters*, 94(14), April 2005. ISSN 0031-9007, 1079-7114. doi: 10.1103/PhysRevLett.94.143903. URL <http://link.aps.org/doi/10.1103/PhysRevLett.94.143903>.
- [44] M. G. Farquhar. JUNCTIONAL COMPLEXES IN VARIOUS EPITHELIA. *The Journal of Cell Biology*, 17(2):375–412, May 1963. ISSN 0021-9525, 1540-8140. doi: 10.1083/jcb.17.2.375. URL <http://www.jcb.org/cgi/doi/10.1083/jcb.17.2.375>.
- [45] B.R. Stevenson and D.L. Paul. The molecular constituents of intercellular junctions. *Current Opinion in Cell Biology*, 1(5):884–891, October 1989. ISSN 09550674. doi: 10.1016/0955-0674(89)90054-9. URL <http://linkinghub.elsevier.com/retrieve/pii/0955067489900549>.
- [46] Gülistan Meşe, Gabriele Richard, and Thomas W White. Gap Junctions: Basic Structure and Function. *Journal of Investigative Dermatology*, 127(11):2516–2524, November 2007. ISSN 0022-202X, 1523-1747. doi: 10.1038/sj.jid.5700770. URL <http://www.nature.com/doi/10.1038/sj.jid.5700770>.
- [47] Daniel A. Goodenough and David L. Paul. Beyond the gap: functions of unpaired connexon channels. *Nature Reviews Molecular Cell Biology*, 4(4):285–295, April 2003. ISSN 14710072, 14710080. doi: 10.1038/nrm1072. URL <http://www.nature.com/doi/10.1038/nrm1072>.
- [48] Soichiro Yamada, Sabine Pokutta, Frauke Drees, William I. Weis, and W. James Nelson. Deconstructing the Cadherin-Catenin-Actin Complex. *Cell*, 123(5):889–901, December 2005. ISSN 00928674. doi: 10.1016/j.cell.2005.09.020. URL <http://linkinghub.elsevier.com/retrieve/pii/S0092867405009748>.
- [49] N. K. Wessells, B. S. Spooner, J. F. Ash, M. O. Bradley, M. A. Luduena, E. L. Taylor, J. T. Wrenn, and K. M. Yamada. Microfilaments in Cellular and Developmental Processes. *Science*, 171(3967):135–143, January 1971. ISSN 0036-8075, 1095-9203. doi: 10.1126/science.171.3967.135. URL <http://www.sciencemag.org/cgi/doi/10.1126/science.171.3967.135>.
- [50] David Garrod and Martyn Chidgey. Desmosome structure, composition and function. *Biochimica et Biophysica Acta (BBA) - Biomembranes*, 1778(3):572–587, March 2008. ISSN 00052736. doi: 10.1016/j.bbamem.2007.07.014. URL <http://linkinghub.elsevier.com/retrieve/pii/S0005273607002751>.

- [51] J. Schweizer, P. E. Bowden, P. A. Coulombe, L. Langbein, E. B. Lane, T. M. Magin, L. Maltais, M. B. Omary, D. A.D. Parry, M. A. Rogers, and M. W. Wright. New consensus nomenclature for mammalian keratins. *The Journal of Cell Biology*, 174(2):169–174, July 2006. ISSN 0021-9525, 1540-8140. doi: 10.1083/jcb.200603161. URL <http://www.jcb.org/cgi/doi/10.1083/jcb.200603161>.
- [52] Marek Haftek, Marie-Hélène Teillon, and Daniel Schmitt. Stratum corneum, corneodesmosomes and ex vivo percutaneous penetration. *Microscopy Research and Technique*, 43(3):242–249, November 1998. ISSN 1059-910X, 1097-0029. doi: 10.1002/(SICI)1097-0029(19981101)43:3 < 242::AID-JEMT6 > 3.0.CO;2-G. URL <http://doi.wiley.com/10.1002/%28SICI%291097-0029%2819981101%2943%3A3%3C242%3A%3AAID-JEMT6%3E3.0.CO%3B2-G>.
- [53] L Gonzalezmariscal. Tight junction proteins. *Progress in Biophysics and Molecular Biology*, 81(1):1–44, January 2003. ISSN 00796107. doi: 10.1016/S0079-6107(02)00037-8. URL <http://linkinghub.elsevier.com/retrieve/pii/S0079610702000378>.
- [54] Anita Janiga, Dominika Bednarska, Bjarne Thorsted, Jonathan Brewer, and Daniel T. Gryko. Quadrupolar, emission-tunable π -expanded 1,4-dihydropyrrolo[3,2-b]pyrroles – synthesis and optical properties. *Organic & Biomolecular Chemistry*, 12(18):2874, 2014. ISSN 1477-0520, 1477-0539. doi: 10.1039/c4ob00143e. URL <http://xlink.rsc.org/?DOI=c4ob00143e>.
- [55] Maciej Krzeszewski, Bjarne Thorsted, Jonathan Brewer, and Daniel T. Gryko. Tetraaryl-, Pentaaryl-, and Hexaaryl-1,4-dihydropyrrolo[3,2-b]pyrroles: Synthesis and Optical Properties. *The Journal of Organic Chemistry*, 79(7):3119–3128, April 2014. ISSN 0022-3263, 1520-6904. doi: 10.1021/jo5002643. URL <http://pubs.acs.org/doi/abs/10.1021/jo5002643>.
- [56] Arthur Edelstein, Nenad Amodaj, Karl Hoover, Ron Vale, and Nico Stuurman. Computer Control of Microscopes Using μ Manager. In Frederick M. Ausubel, Roger Brent, Robert E. Kingston, David D. Moore, J.G. Seidman, John A. Smith, and Kevin Struhl, editors, *Current Protocols in Molecular Biology*. John Wiley & Sons, Inc., Hoboken, NJ, USA, October 2010. ISBN 0471142727, 9780471142720. URL <http://doi.wiley.com/10.1002/0471142727.mb1420s92>.
- [57] Jonathan Brewer, Maria Bloksgaard, Jakub Kubiak, Jens Ahm Sørensen, and Luis A Bagatolli. Spatially Resolved Two-Color Diffusion Measurements in Human Skin Applied to Transdermal Liposome Penetration. *Journal of Investigative Dermatology*, 133(5):1260–1268, May 2013. ISSN 0022-202X, 1523-1747. doi: 10.1038/jid.2012.461. URL <http://www.nature.com/doi/10.1038/jid.2012.461>.

- [58] Johannes Schindelin, Ignacio Arganda-Carreras, Erwin Frise, Verena Kaynig, Mark Longair, Tobias Pietzsch, Stephan Preibisch, Curtis Rueden, Stephan Saalfeld, Benjamin Schmid, Jean-Yves Tinevez, Daniel James White, Volker Hartenstein, Kevin Eliceiri, Pavel Tomancak, and Albert Cardona. Fiji: an open-source platform for biological-image analysis. *Nature Methods*, 9(7):676–682, June 2012. ISSN 1548-7091, 1548-7105. doi: 10.1038/nmeth.2019. URL <http://www.nature.com/doi/10.1038/nmeth.2019>.
- [59] Gyuzel Yu. Mitronova, Vladimir N. Belov, Mariano L. Bossi, Christian A. Wurm, Lars Meyer, Rebecca Medda, Gael Moneron, Stefan Bretschneider, Christian Eggeling, Stefan Jakobs, and Stefan W. Hell. New Fluorinated Rhodamines for Optical Microscopy and Nanoscopy. *Chemistry - A European Journal*, 16(15):4477–4488, April 2010. ISSN 09476539, 15213765. doi: 10.1002/chem.200903272. URL <http://doi.wiley.com/10.1002/chem.200903272>.
- [60] Shamil Nizamov, Katrin I. Willig, Maksim V. Sednev, Vladimir N. Belov, and Stefan W. Hell. Phosphorylated 3-Heteroarylcoumarins and Their Use in Fluorescence Microscopy and Nanoscopy. *Chemistry - A European Journal*, 18(51):16339–16348, December 2012. ISSN 09476539. doi: 10.1002/chem.201202382. URL <http://doi.wiley.com/10.1002/chem.201202382>.
- [61] Philipp Bethge, Ronan Chéreau, Elena Avignone, Giovanni Marsicano, and U. Valentin Nägerl. Two-Photon Excitation STED Microscopy in Two Colors in Acute Brain Slices. *Biophysical Journal*, 104(4):778–785, February 2013. ISSN 00063495. doi: 10.1016/j.bpj.2012.12.054. URL <http://linkinghub.elsevier.com/retrieve/pii/S000634951300074X>.

Protocols & Recipes

A.1 Mowiol Recipe

Mowiol embedding media preparation protocol:

- Start with 6 g Glycerol (analytical grade)
- Add 2.4 g Mowiol 4-88 (Calbiochem #475904)
- Add 6 ml Aqua dest.
- Add 12 ml 0.2 M TRIS buffer pH 8
- Add 2.5 % DABCO (= Anti-Bleaching-Reagent 1.4-Diazabicyclo-82.2.29-octan; Fluka #33480)
- Stir for 4 h (magnetic stirrer)
- Let suspension rest for 2 h
- Incubate for 10 min at 50 °C (water bath)
- Centrifuge at 5000x g for 15 min
- Take the supernatant and freeze it in aliquots at –20 °C

2PA Cross Sectional Data

This appendix lists the tabular data for the two-photon absorption cross sections shown in Section 4.1. For convenience, the compounds without commercial names are numbered in accordance with [54] and [55].

Abberior Star 440SX			Abberior Star 488		
λ	mean $\sigma^{(2)}$	Std. Dev.	λ	mean $\sigma^{(2)}$	Std. Dev.
700	14.02	0.1	700	120.09	7.2
710	15.8	0.24	710	90.81	11.05
720	14.36	$2.85 \cdot 10^{-2}$	720	68.61	10.22
730	15.56	0.35	730	62.83	12.06
740	14.1	0.16	740	65.97	11.12
750	14.38	$9.65 \cdot 10^{-2}$	750	60.99	13.54
760	16.13	0.1	760	78.06	9.44
770	18.3	0.19	770	73.32	9.64
780	21.29	0.24	780	79.01	7.76
790	24.75	0.27	790	71.71	12.7
800	28.48	$7.02 \cdot 10^{-2}$	800	69.37	10.34
810	34.45	0.69	810	52.77	9.42
820	43.63	$4.29 \cdot 10^{-2}$	820	47.35	8.35
830	44.3	0.19	830	26.07	4.85
840	43.63	0.59	840	16.93	1.42
850	39.23	3.44	850	9.37	0.81
860	31.93	3.89	860	6.14	0.55
870	34.21	6.15	870	6.7	0.32
880	39.6	6.5	880	9.2	0.8
890	44.52	2.84	890	11.37	0.64
900	41.43	1.3	900	12.9	0.59
910	42.44	1.45	910	19.21	0.75
920	36.03	0.77	920	24.07	1.42
930	27.29	0.35	930	26.73	0.2
940	23.89	0.42	940	28.38	0.57
950	16.73	0.13	950	31.7	1.21
960	11.59	0.16	960	25.77	0.75
970	9.21	$3.26 \cdot 10^{-2}$	970	26.56	0.72
980	5.87	$7.21 \cdot 10^{-2}$	980	23.74	0.5
990	2.05	0.31	990	23.35	0.48
1,000	0.85	$2.53 \cdot 10^{-2}$	1,000	16.9	0.35
1,010	0.36	$3.31 \cdot 10^{-3}$	1,010	12.79	0.18
1,020	0.23	$1.95 \cdot 10^{-2}$	1,020	11.1	0.53

Table B.1: Tabular values of the two-photon absorption cross section for Abberior Star 440SX and 488.

Compound (4)			Compound (5)			Compound (6)		
λ	mean $\sigma^{(2)}$	Std. Dev.	λ	mean $\sigma^{(2)}$	Std. Dev.	λ	mean $\sigma^{(2)}$	Std. Dev.
700	221.04	9.46	700	9.64	1.78	700	842.94	133.41
710	223.97	35.13	710	7.7	1.61	710	911.69	115.9
720	185.56	36.41	720	5.41	1.31	720	802.39	86.03
730	248.6	83.56	730	4.89	1.06	730	1,047.7	159.7
740	317.54	89.36	740	5.04	1.03	740	1,396.45	273.98
750	252.55	76.28	750	3.29	0.74	750	940.46	143.64
760	236.57	85.66	760	2.54	0.54	760	648.43	82.44
770	207.33	85.44	770	2.07	0.47	770	451.33	40.69
780	192.77	77.5	780	1.79	0.41	780	348.31	45.38
790	172.38	69.81	790	1.58	0.37	790	265.24	38.26
800	163.96	62.27	800	1.51	0.35	800	217.09	31.9
810	144.34	49.42	810	1.43	0.33	810	185.88	28.5
820	162.13	45.89	820	1.58	0.36	820	195.13	30.72
830	125.63	34.03	830	1.31	0.35	830	165.51	25.7
840	104.77	24.77	840	1.05	0.26	840	142.64	22.85
850	94.78	17.46	850	0.92	0.26	850	131.15	21.37
860	74.54	10.54	860	0.66	0.17	860	96.38	15.89
870	74.43	8.54	870	0.61	0.17	870	90.92	15.89
880	79.77	5.07	880	0.62	0.18	880	89.17	14.97
890	77.89	4.26	890	0.53	0.17	890	75.99	13.21
900	49.47	5.82	900	0.33	$9.55 \cdot 10^{-2}$	900	53.78	8.57
910	48.96	2.19	910	0.31	$9.04 \cdot 10^{-2}$	910	47.63	7.52
920	45.76	2.04	920	0.25	$8.21 \cdot 10^{-2}$	920	33.73	5.62
930	36.56	1.19	930	0.17	$5.77 \cdot 10^{-2}$	930	20.06	3.39
940	34.79	0.43	940	0.15	$5.57 \cdot 10^{-2}$	940	13.86	2.2
950	28.45	0.41	950	0.12	$6.64 \cdot 10^{-2}$	950	9.05	1.57
960	21.45	0.18	960	$8.96 \cdot 10^{-2}$	$4.28 \cdot 10^{-2}$	960	5.11	0.91
970	19.1	0.14	970	$9.28 \cdot 10^{-2}$	$3.83 \cdot 10^{-2}$	970	3.14	0.57
980	13.47	0.32	980	$5.7 \cdot 10^{-2}$	$1.67 \cdot 10^{-2}$	980	1.6	0.4
990	8.83	0.26	990	$7.2 \cdot 10^{-2}$	$1.34 \cdot 10^{-2}$	990	0.68	0.25
1,000	4.68	$1.14 \cdot 10^{-2}$	1,000	$5.05 \cdot 10^{-2}$	$2.66 \cdot 10^{-2}$	1,000	0.22	0.14
1,010	2.74	$1.24 \cdot 10^{-2}$	1,010	$2.15 \cdot 10^{-2}$	$3.94 \cdot 10^{-2}$	1,010	$-1.5 \cdot 10^{-2}$	0.12
1,020	2.21	$9.5 \cdot 10^{-2}$	1,020	$1.17 \cdot 10^{-2}$	$2.41 \cdot 10^{-2}$	1,020	-0.11	$8.9 \cdot 10^{-2}$

Table B.2: Tabular values of the two-photon absorption cross section for compounds (4), (5) and (6).

2PA Cross Sectional Data

Compound (7)			Compound (8)			Compound (9)		
λ	mean $\sigma^{(2)}$	Std. Dev.	λ	mean $\sigma^{(2)}$	Std. Dev.	λ	mean $\sigma^{(2)}$	Std. Dev.
700	557.64	56.91	700	187.19	18.96	700	374.56	90.6
710	593.95	23.14	710	141.25	16.89	710	359.89	77.81
720	498.66	16.63	720	93.03	12.12	720	295.28	63.77
730	738.43	1.25	730	73.39	10.96	730	319.14	82.99
740	796.89	10.38	740	65.35	12.7	740	352.75	73.43
750	627.67	1.53	750	35.57	7.09	750	271.76	47.56
760	553.49	1.53	760	25.93	4.61	760	228.71	38.93
770	445.74	16.9	770	20.41	4.37	770	208.65	35.39
780	348.66	6.34	780	17.9	3.32	780	193.45	39.57
790	269.64	8.42	790	16.37	3.04	790	186.02	35.26
800	221.49	0.88	800	15.77	2.77	800	176.08	32.46
810	177.8	1.08	810	15.47	3.42	810	173.23	36.37
820	181.32	1.77	820	17.96	4.21	820	200.3	39.16
830	149.06	9.36	830	14.88	4.35	830	172.51	37.7
840	124.52	1.59	840	12.57	3.73	840	153.66	31.1
850	111.42	2.74	850	11.33	3.52	850	144.92	30.17
860	82.12	$1.63 \cdot 10^{-2}$	860	9.71	2.67	860	116.86	23.5
870	80.8	3.09	870	7.34	2.41	870	111.38	17.62
880	82.34	1.92	880	7.13	2.22	880	122.3	25.14
890	65.48	2.76	890	6.27	2	890	117.56	27.33
900	52.93	1.34	900	3.31	0.51	900	69.21	5.89
910	68.69	7.13	910	2.97	0.29	910	71.97	4.3
920	58.59	6.21	920	2.12	0.62	920	64.23	2.89
930	41.05	3.52	930	1.59	0.64	930	49.46	5.62
940	34.5	2.72	940	1.44	0.58	940	44.18	2.24
950	24.71	1.79	950	0.97	0.5	950	37.51	1.48
960	16.11	1.02	960	1.01	0.37	960	29.69	4.88
970	11.53	0.38	970	0.87	0.32	970	29.51	4.03
980	7.31	0.94	980	0.49	0.6	980	23.91	2.48
990	4.15	0.56	990	0.31	0.23	990	16.91	6.13
1,000	1.69	0.18	1,000	0.22	0.3	1,000	9.45	2.55
1,010	0.92	0.2	1,010	0.38	0.12	1,010	8.3	3.54
1,020	0.75	0.25	1,020	$7.92 \cdot 10^{-2}$	0.34	1,020	6.55	4.38

Table B.3: Tabular values of the two-photon absorption cross section for compounds (7), (8) and (9).

Compound (10)			Compound (11)			Compound (x)		
λ	mean $\sigma^{(2)}$	Std. Dev.	λ	mean $\sigma^{(2)}$	Std. Dev.	λ	mean $\sigma^{(2)}$	Std. Dev.
700	616.22	60.63	700	36.14	1.18	700	112.58	11.67
710	487.22	82.09	710	33.31	1.46	710	101.01	18.93
720	260.96	32.37	720	23.8	1.13	720	79.24	21.9
730	192.32	13.89	730	25.79	2.29	730	80.83	19.7
740	110.36	28.56	740	23.86	1.94	740	99.03	20.89
750	65.3	17.84	750	17.14	1.11	750	71.13	15.63
760	52.22	11.25	760	12.77	0.46	760	59.24	15.76
770	45.02	7.3	770	10.09	0.73	770	44.72	15.46
780	40.3	6.76	780	7.82	0.77	780	37.42	10.35
790	36.61	6.13	790	5.92	0.64	790	32.08	10.8
800	34.09	6	800	4.56	0.29	800	29.1	8
810	31.09	5.48	810	3.29	0.3	810	25.73	5.56
820	31.08	6.38	820	2.48	0.17	820	29.93	3.26
830	25.81	4.77	830	1.39	0.15	830	24.29	1.77
840	20.35	3.99	840	0.78	0.11	840	21.17	0.98
850	16.48	3.51	850	0.48	$7.76 \cdot 10^{-2}$	850	20.09	1.26
860	10.25	2.26	860	0.23	$7.62 \cdot 10^{-2}$	860	16.11	0.92
870	7.71	1.86	870	0.16	$4.73 \cdot 10^{-2}$	870	16.09	1.23
880	5.98	1.56	880	0.18	$6.27 \cdot 10^{-2}$	880	17.67	1.57
890	3.35	0.92	890	0.13	$5.98 \cdot 10^{-2}$	890	16.88	2.17
900	1.57	0.43	900	$7.39 \cdot 10^{-2}$	$2.62 \cdot 10^{-2}$	900	10.78	0.69
910	1.14	0.28	910	$7.29 \cdot 10^{-2}$	$6.6 \cdot 10^{-2}$	910	10.85	0.53
920	0.54	0.1	920	$6.96 \cdot 10^{-2}$	$3.1 \cdot 10^{-2}$	920	9.3	0.58
930	0.21	$5.1 \cdot 10^{-2}$	930	$2.36 \cdot 10^{-2}$	$5.09 \cdot 10^{-2}$	930	6.73	0.43
940	0.15	$3.94 \cdot 10^{-2}$	940	$9.92 \cdot 10^{-2}$	$4.94 \cdot 10^{-2}$	940	5.72	0.53
950	0.11	$4.62 \cdot 10^{-2}$	950	$5.76 \cdot 10^{-2}$	$1.71 \cdot 10^{-2}$	950	4.28	0.47
960	$6.21 \cdot 10^{-2}$	$2.17 \cdot 10^{-2}$	960	$9.58 \cdot 10^{-2}$	$1.59 \cdot 10^{-2}$	960	2.91	0.41
970	$6.91 \cdot 10^{-2}$	$5.96 \cdot 10^{-2}$	970	0.1	$1.79 \cdot 10^{-2}$	970	2.29	0.22
980	$5.45 \cdot 10^{-2}$	$5.81 \cdot 10^{-2}$	980	$9.1 \cdot 10^{-2}$	$1.52 \cdot 10^{-2}$	980	1.44	0.13
990	$4.02 \cdot 10^{-2}$	$3.63 \cdot 10^{-2}$	990	0.17	$7.14 \cdot 10^{-2}$	990	0.91	$9.54 \cdot 10^{-2}$
1,000	$4.69 \cdot 10^{-2}$	$4.26 \cdot 10^{-2}$	1,000	$8.31 \cdot 10^{-2}$	$4.46 \cdot 10^{-2}$	1,000	0.46	0.1
1,010	$2.2 \cdot 10^{-2}$	$4.43 \cdot 10^{-2}$	1,010	$6.87 \cdot 10^{-2}$	$3.47 \cdot 10^{-2}$	1,010	0.23	$9.41 \cdot 10^{-2}$
1,020	$2.06 \cdot 10^{-2}$	$2.7 \cdot 10^{-2}$	1,020	$4.15 \cdot 10^{-2}$	$8.41 \cdot 10^{-2}$	1,020	0.18	$7.22 \cdot 10^{-2}$

Table B.4: Tabular values of the two-photon absorption cross section for compounds (10), (11) and (x).

2PA Cross Sectional Data

Compound (25)			Compound (26)			Compound (35)		
λ	mean $\sigma^{(2)}$	Std. Dev.	λ	mean $\sigma^{(2)}$	Std. Dev.	λ	mean $\sigma^{(2)}$	Std. Dev.
700	53.22	10.28	700	583.01	30.56	700	700.09	44.7
710	39.98	5.29	710	683.04	46.89	710	630.36	86.9
720	29.33	3.52	720	562	15.39	720	436.92	60.33
730	27.98	3.69	730	483.15	19.54	730	413.17	69.9
740	26.58	3.35	740	339.39	42.81	740	334.44	87.88
750	16.96	1.74	750	180.4	17.87	750	218.32	35.63
760	11.43	1.02	760	124.1	1.41	760	143.88	25.49
770	8.48	0.52	770	99.92	3.26	770	116.07	16.23
780	6.82	0.56	780	83.12	7.09	780	92.64	15.89
790	5.38	0.12	790	74.02	1.52	790	82.23	15.66
800	4.67	0.31	800	68.26	4.64	800	72.56	14.76
810	4.18	0.17	810	60.65	2.49	810	58.23	10.15
820	4.2	0.66	820	60.31	$6.99 \cdot 10^{-2}$	820	52.45	11.49
830	3.53	0.29	830	49.45	6.09	830	44.12	8.08
840	2.52	0.47	840	37.51	1.81	840	32.81	7.31
850	2.38	0.29	850	30.27	3.65	850	25.38	5.53
860	1.41	0.1	860	24.1	4.23	860	15.85	3.71
870	1.19	0.28	870	21.68	5.63	870	12.46	2.53
880	1.39	0.15	880	13.37	1.34	880	9.01	2.05
890	1.44	0.53	890	9.24	2.24	890	4.3	2.15
900	0.33	0.49	900	4.62	0.58	900	2.29	0.35
910	0.47	0.52	910	3.25	0.57	910	0.78	0.28
920	0.13	0.71	920	3.09	0.39	920	0.58	0.13
930	0.29	0.19	930	1.09	0.13	930	0.54	0.8
940	0.45	0.41	940	1.41	0.73	940	-0.15	0.65
950	0.19	0.41	950	0.72	0.2	950	-0.52	0.42
960	0.3	0.37	960	0.28	0.24	960	-0.2	0.56
970	0.53	0.62	970	1.01	0.26	970	-0.88	0.74
980	$6.15 \cdot 10^{-2}$	0.81	980	0.57	$2.24 \cdot 10^{-2}$	980	-0.48	0.44
990	0.17	0.67	990	0.55	0.81	990	-0.49	1.04
1,000	0.33	0.2	1,000	0.84	0.56	1,000	-0.85	0.7
1,010	0.15	0.14	1,010	0.51	0.79	1,010	-0.98	0.78
1,020	$5.02 \cdot 10^{-2}$	0.21	1,020	0.42	0.79	1,020	-0.43	0.44

Table B.5: Tabular values of the two-photon absorption cross section for compounds (25), (26) and (35).

Compound (39)			Compound (41)		
λ	mean $\sigma^{(2)}$	Std. Dev.	λ	mean $\sigma^{(2)}$	Std. Dev.
700	355.5	36.62	700	522.18	79.91
710	342.11	46.2	710	492.89	80.46
720	247.36	31	720	319.52	55.35
730	227.46	31.82	730	285.26	46.74
740	173.84	32.07	740	188.56	38.19
750	103.67	14.09	750	110.87	19.86
760	69.99	9.5	760	80.17	14.52
770	59.68	11.94	770	66.92	12.21
780	50.78	8.92	780	56.29	13.25
790	44.45	7.46	790	50.36	9.9
800	37.14	7.53	800	42.44	9.5
810	30.48	4.21	810	36.79	6.71
820	28.21	5.11	820	35.06	6.79
830	22.3	2.73	830	27.71	3.53
840	15.39	1.73	840	19.68	5.06
850	10.45	2.64	850	14.64	2.74
860	7.49	5.09	860	8.87	2.53
870	5.72	6.45	870	5.84	0.72
880	2.09	1.3	880	3.3	1.09
890	0.35	2.11	890	1.45	0.66
900	0.11	1.49	900	0.5	0.42
910	0.37	0.61	910	0.53	0.51
920	0.68	0.7	920	$3.97 \cdot 10^{-2}$	0.63
930	$2.34 \cdot 10^{-2}$	0.52	930	$3.14 \cdot 10^{-2}$	0.27
940	0.34	0.54	940	$4.5 \cdot 10^{-2}$	0.4
950	0.55	0.53	950	$7.47 \cdot 10^{-2}$	0.64
960	$8.95 \cdot 10^{-2}$	0.62	960	$4.94 \cdot 10^{-2}$	$6.7 \cdot 10^{-2}$
970	0.47	0.72	970	0.21	0.51
980	0.36	0.72	980	0.16	0.4
990	0.52	1.14	990	0.26	0.26
1,000	0.28	0.47	1,000	0.14	0.12
1,010	0.34	0.45	1,010	0.17	0.26
1,020	0.19	0.47	1,020	$8.3 \cdot 10^{-3}$	0.68

Table B.6: Tabular values of the two-photon absorption cross section for compounds (39) and (41).

Lab Automation and Matlab Scripts

C.1 Automation Control for the Equipment

C.1.1 Micro-manager Script for Controlling the 2PA Cross-Section Setup

```
1 import org.micromanager.api.*;
2 import mmcorej.CharVector;
3 import java.text.DecimalFormat;
4 import java.text.NumberFormat;
5 import java.util.ArrayList;
6 import javax.swing.*;
7 import java.awt.*;
8 import java.lang.System;
9 import java.lang.Math;
10 import java.lang.*;
11 import java.util.*;
12 import java.io.*;
13 import org.micromanager.api.PositionList;
14 import org.micromanager.api.MultiStagePosition;
15
16 // clear all previous acquisitions
17 gui.closeAllAcquisitions();
18 gui.clearMessageWindow();
19 // Ready laser and AOTF plate control
20 laserPort = "COM1";
21 aotfPort = "COM5";
22 channel = 1;
23 powerOn = 1;
24 String newLine = "\n";
25 n = newLine;
26 String sendLine = "\r";
27 Float[] powerFactor = {1.0}; //{0.7, 1.0, 1.5};
28 numPowers = powerFactor.length;
29
30 Object[] choices = {"Correct, _continue",
```

```

31         "Incorrect, stop process");
32 int comp = JOptionPane.showOptionDialog(null,
33     "Please make sure that the COM ports are correct.\n"
34     + "laser port is " + laserPort + ",\n"
35     + "AOTF port is " + aotfPort + ".",
36     "Check COM ports",
37     JOptionPane.YES_NO_OPTION,
38     JOptionPane.QUESTION_MESSAGE,
39     null,
40     choices,
41     choices[0]);
42 if (comp == 1) {
43     JOptionPane.showMessageDialog(null,
44         "Please open the script to manually edit the COM port values_
45         and correct them in the Micro-Manager config file",
46         "Script terminating",
47         JOptionPane.WARNING_MESSAGE);
48 } else {
49     // file locations
50     rootDirName = "C:/acquisitionData";
51
52     // parameters
53     numAves = 1;
54     stagePause = 2000;
55     exposureTime = 59900;
56     intervalFrame = 60300;
57     stabilizePause = 60000;
58
59     float[][] wlPower = {
60         {700, 710, 720, 730, 740, 750, 760, 770, 780, 790,
61         800, 810, 820, 830, 840, 850, 860, 870, 880, 890,
62         900, 910, 920, 930, 940, 950, 960, 970, 980, 990,
63         1000, 1010, 1020},//[0][x] - wavelength
64         //{135.00, 134.00, 133.00, 130.50, 128.00, 126.00, 124.00,
65         122.5, 121.60, 119.80,
66         //{118.00, 116.50, 115.00, 113.5, 112.00, 111.00, 110.00, 109.00,
67         108.00, 106.00,
68         //{104.00, 103.00, 102.00, 100.00, 98.00, 97.00, 96.00, 95.00,
69         94.00, 94.00, 94.00},//[1][x] frequency
70         {135.00, 134.00, 133.00, 130.50, 128.00, 126.00, 124.00, 122.5,
71         121.60, 119.80,
72         {118.00, 116.50, 115.00, 113.5, 112.00, 111.00, 110.00, 109.00,
73         108.00, 106.00,
74         {104.00, 103.00, 102.00, 100.00, 101.50, 100.00, 99.00, 97.50,
75         97.00, 96.50,
76         {95.00, 94.50, 94.00},//[1][x] frequency
77         {0.4, 0.4, 0.6, 0.4, 0.5, 0.6, 0.7, 0.7, 0.7, 0.7,
78         0.8, 0.8, 0.8, 0.8, 0.9, 0.9, 0.9, 0.9, 0.9, 0.9, 1.0,
79         1.2, 1.2, 1.2, 1.3, 1.5, 1.5, 1.5, 1.2, 1.2, 1.2,
80         1.8, 1.8, 2.0},//[2][x] intensity
81         {-6.6883, -5.874, -5.32989, -5.11026, -5.00663, -4.88149,
82         -4.78434, -4.61359, -4.58284, -4.61130,

```

```
77     -4.72077, -4.74054, -4.80032, -4.85861, -4.89991, -4.9871,  
78         -5.0153, -5.07397, -5.13365, -5.35701,  
79     -5.80038, -5.999, -5.856, -6.267, -6.89397, -6.99919, -6.38841,  
80         -6.64077, -7.964796, -8.08169,  
81     -7.12945, -6.998096, -7.40} //[3][x] intercept  
82     };  
83     float slope = 0.2178697119;  
84     defaultStart = "700";  
85     defaultEnd = "1020";  
86     defaultStep = "10";  
87     JPanel wavelengthPanel = new JPanel();  
88     wavelengthPanel.setLayout(new GridBagLayout());  
89     GridBagConstraints c = new GridBagConstraints();  
90  
91     JLabel labelInfo = new JLabel("<HTML>Please_input_the_starting_and<BR>ending  
92         _wavelengths_for_this_experiment<BR></HTML>");  
93     c.fill = GridBagConstraints.HORIZONTAL;  
94     c.gridx = 0;  
95     c.gridy = 0;  
96     c.gridwidth = 4;  
97     wavelengthPanel.add(labelInfo, c);  
98  
99     JLabel labelStart = new JLabel("<HTML>Start:<HTML>");  
100     Insets insets = new Insets(15,0,10,0);  
101     c.gridx = 1;  
102     c.gridy = 1;  
103     c.weightx = 0.5;  
104     c.gridwidth = 1;  
105     wavelengthPanel.add(labelStart, c);  
106  
107     JTextField startField = new JTextField(defaultStart,5);  
108     //c.fill = GridBagConstraints.HORIZONTAL;  
109     insets = new Insets(15,0,10,0);  
110     c.gridx = 2;  
111     c.gridy = 1;  
112     c.weightx = 0.5;  
113     wavelengthPanel.add(startField, c);  
114  
115     JLabel labelEnd = new JLabel("<HTML>End:</HTML>");  
116     c.fill = GridBagConstraints.HORIZONTAL;  
117     insets = new Insets(15,0,0,0);  
118     c.gridx = 1;  
119     c.gridy = 2;  
120     c.weightx = 0.5;  
121     wavelengthPanel.add(labelEnd, c);  
122  
123     JTextField endField = new JTextField(defaultEnd,5);  
124     //c.fill = GridBagConstraints.HORIZONTAL;  
125     insets = new Insets(15,0,0,0);  
126     c.gridx = 2;  
127     c.gridy = 2;  
128     c.weightx = 0.5;
```

```

128 wavelengthPanel.add(endField, c);
129
130 labelStep = new JLabel("<HTML>Step:</HTML>");
131 c.fill = GridBagConstraints.HORIZONTAL;
132 insets = new Insets(15,0,0,0);
133 c.gridx = 1;
134 c.gridy = 3;
135 c.weightx = 0.5;
136 wavelengthPanel.add(labelStep, c);
137
138 JTextField stepField = new JTextField(defaultStep,5);
139 //c.fill = GridBagConstraints.HORIZONTAL;
140 insets = new Insets(15,0,0,0);
141 c.gridx = 2;
142 c.gridy = 3;
143 c.weightx = 0.5;
144 wavelengthPanel.add(stepField, c);
145
146
147 int result = JOptionPane.showConfirmDialog(null,
148     wavelengthPanel,
149     "Select_wavelengths",
150     JOptionPane.OK_CANCEL_OPTION);
151 if (result == JOptionPane.OK_OPTION) {
152     wlStart = Integer.parseInt(startField.getText());
153     wlEnd = Integer.parseInt(endField.getText());
154     wlStep = Integer.parseInt(stepField.getText());
155     print("Start_value:_ " + wlStart);
156     print("End_value:_ " + wlEnd);
157     print("Step_value:_ " + wlStep);
158     gui.sleep(1000);
159 }
160
161 // Ask user if laser is already running
162 Object[] options = {"Yes",
163     "No"};
164 int startChoice = JOptionPane.showOptionDialog(null,
165     "Is_the_laser_turned_on?",
166     "Laser_control",
167     JOptionPane.YES_NO_OPTION,
168     JOptionPane.QUESTION_MESSAGE,
169     null,
170     options,
171     options[0]);
172
173 String[] startOptions = {"Laser_is_already_running._Moving_wl_to_
174     start_position.",
175     "Laser_will_now_be_turned_on."};
176 gui.message(startOptions[startChoice] + "_(" + startChoice + ")");
177
178 // Ask user if laser should stay on after experiment is done
179 Object[] options = {"Turn_off",
180     "Keep_running"};
181 int laserChoice = JOptionPane.showOptionDialog(null,

```

```

181     "Should_the_laser_be_turned_off"
182     + "after_this_experiment?",
183     "Laser_control",
184     JOptionPane.YES_NO_OPTION,
185     JOptionPane.QUESTION_MESSAGE,
186     null,
187     options,
188     options[0]);
189
190 String[] choice = {"Laser_will_be_turned_off_after_tests",
191     "Laser_will_be_kept_running"};
192 gui.message(choice[laserChoice] + "_" + laserChoice + "");
193
194 // Method for writing to the COM port
195 sendCommand(String comPort, String command) {
196     CharVector m = new CharVector();
197     for (char i : command) {
198         m.add(i);
199     }
200     mmc.writeToSerialPort(comPort, m);
201 }
202
203 // Method for reading from COM port
204 String readBuffer(String comPort, boolean doPrint) {
205     Thread.sleep(200);
206     str1 = "BLANK";
207     answer = mmc.readFromSerialPort(comPort);
208     if (answer.capacity() > 0) {
209         for(i=0; i<answer.capacity(); i++){
210             if(str1 == "BLANK") {
211                 str1 = "" + answer.get(i);
212             } // you have to add the "" otherwise adds decimal
                value
213
214             else {
215                 str1 = "" + str1 + (char)answer.get(i);
216                 str2 = str1.trim();
217             }
218         } // end loop
219         if (doPrint == true) {
220             print(str2);
221             return str2;
222         } else {
223             return str2;
224         }
225     }
226
227 //Set AOTF to internal mode
228 sendCommand(aotfPort, "IO\r");
229
230 // If the user says no, turn on laser
231 if (startChoice == 1) {
232     mmc.setSerialPortCommand(laserPort, "READ:PCTW?", "\r");
233     String pctLAns = readBuffer(laserPort, false);

```

```

234     pctReady = "100.00%";
235     print (pctReady);
236     if (pctLAns.equals (pctReady)) {
237         gui.clearMessageWindow();
238         print (pctLAns);
239     } else {
240         while (!pctLAns.equals (pctReady)) {
241             gui.clearMessageWindow();
242             print (pctLAns);
243             mmc.setSerialPortCommand (laserPort, "READ:PCTW?", "\r");
244             String pctLAns = readBuffer (laserPort, false);
245         }
246     }
247     mmc.setSerialPortCommand (laserPort, "WAV_800", "\r");
248     mmc.setSerialPortCommand (laserPort, "READ:WAV?", "\r");
249     String nextLAns = readBuffer (laserPort, false);
250     while (!nextLAns.equals ("800nm")) {
251         gui.clearMessageWindow();
252         print ("Moving_laser_to_800nm");
253         print ("Current_wavelength:_ " + nextLAns);
254         gui.sleep (500);
255         mmc.setSerialPortCommand (laserPort, "READ:WAV?", "\r");
256         nextLAns = readBuffer (laserPort, false);
257     }
258     mmc.setSerialPortCommand (laserPort, "PLAS:AHIS?", "\r");
259     checkNum = readBuffer (laserPort, false);
260     print (checkNum);
261     laserReady = false;
262     while (laserReady == false) {
263         switch (checkNum.charAt (0)) {
264             case '1':
265                 laserReady = true;
266                 print ("Laser_is_ready_(Status_code:_ " + checkNum.
                charAt (0) + ")");
267                 break;
268             case '3':
269                 Thread.sleep (5000);
270                 mmc.setSerialPortCommand (laserPort, "PLAS:AHIS?",
                "\r");
271                 checkNum = readBuffer (laserPort, false);
272                 print ("Laser_stabilizing_(Status_code:_ " +
                checkNum.charAt (0) + ")");
273                 laserReady = false;
274                 break;
275             case '5':
276                 mmc.setSerialPortCommand (laserPort, "ON", "\r");
277                 mmc.setSerialPortCommand (laserPort, "PLAS:AHIS?",
                "\r");
278                 checkNum = readBuffer (laserPort, false);
279                 laserReady = false;
280                 break;
281             default: break;
282         }
283     }

```

```

284 }
285
286 // Tune laser to start wavelength
287 mmc.setSerialPortCommand(laserPort, "SHUT_1", "\r");
288 mmc.setSerialPortCommand(laserPort, "READ:WAV?", "\r");
289 String testAns = readBuffer(laserPort, false);
290 String versAns = wlStart + "nm";
291 if (!testAns.equals(versAns)) {
292     mmc.setSerialPortCommand(laserPort, "WAV_" + wlStart, "\r");
293     mmc.setSerialPortCommand(laserPort, "READ:WAV?", "\r");
294     laserResponse = readBuffer(laserPort, false);
295     while (!laserResponse.equals(versAns)) {
296         gui.clearMessageWindow();
297         mmc.setSerialPortCommand(laserPort, "READ:WAV?", "\r");
298         laserResponse = readBuffer(laserPort, false);
299         print("Moving_laser_to_" + wlStart);
300         print("Current_wavelength:_" + laserResponse);
301         gui.sleep(500);
302     }
303     print("Waiting_for_laser_to_stabilize");
304     for (int time = 60; time > 0; time--) {
305         gui.clearMessageWindow();
306         print("Waiting_for_laser_to_stabilize");
307         print(time + "_seconds_remaining");
308         gui.sleep(1000);
309     }
310 }
311
312 // display time and date using toString()
313 Date beginDate = new Date();
314 gui.clearMessageWindow();
315 print("Experiment_started_at_" + beginDate);
316
317 // Save measurement initiation timestamp
318 wlNum = (wlEnd - wlStart)/wlStep + 1;
319 beginning = System.currentTimeMillis();
320 mmc.setAutoShutter(true);
321 // Acquire position list from Multi-D acq. (Remember to load position
    list first)
322 PositionList pl = gui.getPositionList();
323 numFrames = numAverages * wlNum;
324 String[] acqs = new String[pl.getNumberOfPositions()];
325 intervalRep = ((intervalFrame + stagePause) * pl.getNumberOfPositions
    ()) * numPowers + stabilizePause;
326 mmc.setExposure(exposureTime);
327 print("Each_wl_scan_will_take_approx:_" + (intervalRep/60000) + "."
    + (intervalRep%60000) + "_minutes_" + intervalRep + "_ms");
328
329 DecimalFormat df = new DecimalFormat("#.00");
330 xStep = wlStep/10; // Correlates the wlStep to index numbers
331 imageNr = 0;
332
333 for (int wlCur = wlStart; wlCur <= wlEnd; wlCur += wlStep) {
334     startTime = System.currentTimeMillis();

```

```

335 String acqName = "dummyname" + wlcur;
336 gui.openAcquisition(acqName, rootDirName, // (String name, String
    rootDir,
337     numFrames, 1, numPowers, //int nrFrames, int nrChannels,
    int nrSlices,
338     pl.getNumberOfPositions(), false, false); // int
    nrPositions, boolean show, boolean save)
339
340 for (int wlTest = 700, x = 0; wlTest <= wlEnd; wlTest += wlStep,
    x += xStep) {
341     if(wlTest == wlCur) {
342         for (int samplePos=0; samplePos < pl.getNumberOfPositions
            ()); samplePos++) {
343             acqs[samplePos] = pl.getPosition(samplePos).getLabel
                ();
344             MultiStagePosition.goToPosition(pl.getPosition(
                samplePos), mmc);
345             for (int p = 0; p < numPowers; p++) {
346                 float powerDbm = (Math.log(wlPower[2][x]*0.2*
                    powerFactor[p]) - wlPower[3][x])/slope;
347                 fullC = "L" + channel + "F" + df.format(wlPower
                    [1][x]) + "D" + df.format(powerDbm) + "0l\r";
348                 print("channel:_ " + channel
                    + ",_frequency:_ " + df.format(wlPower[1][x])
349                     + ",_power_(dBm):_" + df.format(powerDbm*
350                         powerFactor[p]));
351                 sendCommand(aotfPort, fullC);
352                 readBuffer(aotfPort, true);
353                 gui.sleep(stagePause);
354
355                 // create acquisition and set options
356                 for (int i=0; i<numAves; i++) {
357                     now = System.currentTimeMillis();
358                     gui.message("Acquiring_sample_" + (samplePos
                        + 1)
                        + "_at_position_" + acqs[samplePos]
359                         + "_at_" + wlCur
360                         + "nm_and_power_step_" + (p+1));
361                     print("acqName:_ " + acqName + n + "frames:_ "
                        + numFrames + n
362                         + "image_nr.:" + imageNr);
363                     gui.snapAndAddImage(acqName, i, 0, p,
                        samplePos);
364                     imageNr++;
365                     itTook = System.currentTimeMillis() - now;
366                     Date date = new Date();
367                     print("Time_stamp:_ " + date);
368                     if (itTook < intervalFrame)
369                         gui.sleep(intervalFrame - itTook);
370                 }
371             }
372         }
373     }
374     totalTime = (System.currentTimeMillis() - startTime);

```

```
375         gui.message("Total_time:_" + (totalTime/1000) + "." + (
376             totalTime%1000)
377             + "_seconds_" + totalTime + "_ms");
378         // Change laser wavelength
379         wlNext = wlCur + wlStep;
380         command = "WAV_" + wlNext;
381         if (wlCur < wlEnd) {
382             mmc.setSerialPortCommand(laserPort, command, "\r");
383             mmc.setSerialPortCommand(laserPort, "WAV?", "\r");
384             laserResponse = readBuffer(laserPort, false);
385             print("Current_wavelength:_" + laserResponse);
386             // Insert laser stabilizing time
387             if (totalTime < intervalRep) {
388                 gui.sleep(intervalRep - totalTime);
389             }
390         }
391     }
392     gui.closeAcquisition(acqName);
393 }
394 mmc.setSerialPortCommand(laserPort, "SHUT_0", "\r");
395 sendCommand(aotfPort, "I1\r");
396 if (laserChoice == 0) {
397     mmc.setSerialPortCommand(laserPort, "OFF", "\r");
398 }
399
400 Date date = new Date();
401 // display time and date using toString()
402 print("Experiment_finished_at_" + date);
403 gui.message("Elapsed_time_" + ((System.currentTimeMillis() -
404     beginning)/60000) + "_minutes.");
```

Script C.1: Automation script for microscope, shutter, AOTF and laser. Allows for serial irradiation of multiple samples at several wavelengths and intensities.


```
47
48 Set Sheet1 = CreateObject("WinX32.ExpSetupUI")
49 Dim Page4: Set Page4 = Sheet1.GetPageObj(1)
50     Page4.SetFileAccess EXPFA_OVERWRITE ' Set to External Sync
51     Page4.AutoIncrementEnable False ' Auto Increment filename =
        True
52     ' Page4.AutoIncrementValue 1 ' Set AutoIncrement Current Value
53     Page4.SetAutoSaveOption EXPAS_AUTO ' Set to Automatically save
        file after each run
54
55
56 For w = wlstart To wlend Step wlstep 'change step size'
57     For s = 1 To smax
58         For i = 1 To imax
59             Set Sheet1 = CreateObject("WinX32.ExpSetupUI")
60             Set Page4 = Sheet1.GetPageObj(1)
61             Page4.SetDataFilePathAndName savepath & savedate,
                filename & w & "-" & i & "-1-" & s ' Path, Filename
62
63             Set Page4 = Nothing
64             Set Sheet1 = Nothing
65             Dim Doc1: Set Doc1 = ExpVB.Start2() ' Start Acquisition
66             ExpVB.WaitForExperiment ' Wait for collection to complete
67         Next
68     Next
69 Next
70 End Sub : Main ' finish and run this script
```

Script C.2: Spectrofluorometer and WinSpec/32 software control script for standard data collection in conjunction with C.1.1.

C.2 MATLAB® Scripts

C.2.1 Calculation of Dye Concentration

```

1 % Calculate concentration of samples
2 %clear all
3 function [conc,maxAbs] = concentration(sample,dilution);
4 % Molar extinction coefficients for references
5 MECref = [38500;106000;116000;75000;75000];
6 refidx = {'PER', 'RB', 'R6G', 'FLU','oldFLU'};
7 % Molar extinction coefficients for AJ sample series
8 MECAJ = [70450;67048;78043;45152;71042;64264;54000;33000;62000];
9 AJidx = {'AJ281', 'AJ332', 'AJ345', 'AJ328', 'AJ346', 'AJ341', 'AJ111',
          'AJ116', 'AJ344'};
10 % Molar extinction coefficient for MK sample series
11 MKidx = {'MK143','MK145','MK147','MK153','MK154'};
12 MECMK = [39791;39693;32931;36188;42598];
13 MECST = [30800;86000];
14 STidx = {'ST440','ST488'};
15 Midx = [refidx,AJidx,MKidx,STidx];
16 MEC = [MECref;MECAJ;MECMK;MECST];
17 % Import sample data
18
19 %sample = 'FLU'; % The sample data to be analyzed
20 %dilution = '1A3'; % The sample dilution to be analyzed
21 for n = 1:1
22 name = ['/home/bjarne/Universitet/Dyes/Absorption/2015/',sample,'-',
          dilution,mat2str(n),'.SP']; % Create filename
23 S = importdata(name, '\t',86); % Import data
24 dataS = S.data; % copy data from cell S to matrix dataS;
25 dataAll(:,n) = dataS(:,2);
26 end
27 dataM = mean(dataAll,2);
28 SMEC = MEC(strmatch(sample,Midx)); % Find the correct molar extinct.
          coeff.
29 maxAbs = max(dataM(:,1)); % Locate the maximum absorption
30 conc = maxAbs./sMEC; % Calculate concentration

```

Script C.6: MATLAB® function designed to calculate dye concentration from absorption spectra

C.2.2 Calculation of 2PA Cross-Section of Dyes

```

1 clear all
2 close all
3 % Define experiment date, filename, sample and reference names and
  indices
4 % Samplegroup is the filename prefix that designates the different
  samples
5 % in each experiment run. Usually named after sample positions in
  sample
6 % holder
7 exwl = (700:10:1020);
8 %date = '131216'; samplegroup = 'r6g-per-rb-flu'; samples = {'R6G','
  PER','RB','FLU'}; wlc = [524,520,550,520];
9 %date = '131118'; samplegroup = 'aj111-aj116-aj328-aj332-aj341-flu';
  samples = {'AJ111','AJ116','AJ328','AJ332','AJ341','FLU'}; wlc =
  [510,520,520,540,520];
10 %date = '131119'; samplegroup = 'aj281-aj345-aj346-flu-mk143';
  samples = {'AJ281','AJ345','AJ346','MK143','FLU'}; wlc =
  [540,540,510,540];
11 %date = '131121'; samplegroup = 'mk145-mk147-mk153-mk154-flu';
  samples = {'MK145','MK147','MK153','MK154','FLU'}; wlc =
  [530,520,520,520];
12 %date = '131122'; samplegroup = 'aj111-aj116-aj328-aj332-aj341-flu';
  samples = {'AJ111','AJ116','AJ328','AJ332','AJ341','FLU'}; wlc =
  [510,520,540,540,520];
13 %date = '131125'; samplegroup = 'aj116-aj328-aj332-aj346-mk143-flu';
  samples = {'AJ116','AJ328','AJ332','AJ346','MK143','FLU'}; wlc =
  [540,540,550,540,545];
14 %date = '131126'; samplegroup = 'aj111-mk145-mk147-mk153-mk154-flu';
  samples = {'AJ111','MK145','MK147','MK153','MK154','FLU'}; wlc =
  [510,530,520,520,520];
15 %date = '131202'; samplegroup = 'mk145-mk147-mk153-mk154-flu';
  samples = {'MK145','MK147','MK153','MK154','FLU'}; wlc =
  [530,520,520,520];
16 %date = '131203'; samplegroup = 'mk145-mk147-mk153-mk154-flu';
  samples = {'MK145','MK147','MK153','MK154','FLU'}; wlc =
  [530,520,520,520];
17 %date = '131203-1'; samplegroup = 'mk145-mk147-mk153-mk154-flu';
  samples = {'MK145','MK147','MK153','MK154','FLU'}; wlc =
  [530,520,520,520];
18 %date = '131204'; samplegroup = 'aj116-aj328-aj341-aj346-mk143-flu';
  samples = {'AJ116','AJ328','AJ341','AJ346','MK143','FLU'}; wlc =
  [540,540,520,540,530];
19 %date = '131205'; samplegroup = 'aj116-aj328-aj341-aj346-mk143-flu';
  samples = {'AJ116','AJ328','AJ341','AJ346','MK143','FLU'}; wlc =
  [540,540,520,540,530];
20 %date = '131205-1'; samplegroup = 'aj116-aj328-aj341-aj346-mk143-flu
  '; samples = {'AJ116','AJ328','AJ341','AJ346','MK143','FLU'}; wlc
  = [540,540,520,560,530];
21 %date = '131206'; samplegroup = 'aj111-aj281-aj332-aj345-flu';
  samples = {'AJ111','AJ281','AJ332','AJ345','FLU'}; wlc =
  [510,540,540,540];

```

```

22 %date = '131206-1'; samplegroup = 'aj111-aj281-aj332-aj345-flu';
    samples = {'AJ111','AJ281','AJ332','AJ345','FLU'}; wlc =
    [510,540,540,540];
23 %date = '131209'; samplegroup = 'aj111-aj281-aj332-aj345-flu';
    samples = {'AJ111','AJ281','AJ332','AJ345','FLU'}; wlc =
    [510,540,540,540]; exwl = (700:10:900);
24 %date = '131210'; samplegroup = 'aj111-aj281-aj332-aj345-flu';
    samples = {'AJ111','AJ281','AJ332','AJ345','FLU'}; wlc =
    [510,540,540,540]; exwl = (700:10:900);
25 %date = '140123'; samplegroup = 'flu-aj344-aj344-aj344'; samples = {'
    FLU','AJ344','AJ344','AJ344'}; wlc = [520,520,520,520]; exwl =
    (700:10:1020); savedate = {'140123','140123-1','140123-2'};
26 %date = '140124'; samplegroup = 'aj344-aj344-flu-flu'; samples = {'
    AJ344','AJ344','oldFLU','FLU'}; wlc = [520,520,520,520]; exwl =
    (700:10:1020); savedate =
    {'140124','140124-1','140124','140124'};
27 %date = '140129'; samplegroup = 'aj344-aj344-aj344-aj345-flu';
    samples = {'AJ344','AJ344','AJ344','AJ345','FLU'}; wlc =
    [520,520,520,540]; exwl = (700:10:1020); savedate =
    {'140129','140129-1','140129-2','140129'};
28 %date = '140130'; samplegroup = 'aj344-aj345-flu'; samples = {'AJ344
    ','AJ345','FLU'}; wlc = [520,540]; exwl = (700:10:1020); savedate
    = {'140130','140130'};
29 %date = '140131'; samplegroup = 'aj344-aj344-aj344-flu'; samples = {'
    AJ344','AJ344','AJ344','FLU'}; wlc = [520,520,520]; exwl =
    (700:10:1020); savedate = {'140131','140131-1','140131-2'};
30 %date = '150115'; samplegroup = 'FLU-ST440-ST488-R6G'; samples = {'
    FLU','ST440','ST488','R6G'}; wlc = [520,525,530,540]; exwl =
    (700:10:1020); savedate = {'150115','150115','150115','150115'};
31 %date = '150116'; samplegroup = 'FLU-ST440-ST488-R6G'; samples = {'
    FLU','ST440','ST488','R6G'}; wlc = [520,525,530,540]; exwl =
    (700:10:1020); savedate = {'150116','150116','150116','150116'};
32 %date = '150123'; samplegroup = 'FLU-ST440-ST488-R6G'; samples = {'
    FLU','ST440','ST488','R6G'}; wlc = [520,525,530,540]; exwl =
    (700:10:1020); savedate = {'150123','150123','150123','150123'};
33 date = '150124'; samplegroup = 'FLU-FLU-ST440-ST440-ST488-ST488-R6G-
    R6G'; samples = {'FLU','FLU','ST440','ST440','ST488','ST488','R6G
    ','R6G'}; wlc = [520,520,525,525,530,530,540,540]; exwl =
    (700:10:1020); savedate = {'150124','150124-1','150124','150124-1
    ','150124','150124-1','150124','150124-1'};
34 refname = 'FLU';
35 %ref = 4;
36 ref = find(strncmp(samples,refname,3),1); % Reference index as above
37 showlegend = 0;
38
39 colorspecs = distinguishable_colors(33);
40 set(gcf,'DefaultAxesColorOrder',colorspecs);
41
42 wlnum = length(exwl);
43 % Define equation variables
44 %powerS = [2.0 2.0 2.0 2 2 2 2]; % Laser power used on sample
45 %powerR = [2.0 2.0 2.0 2 2 2 2]; % Laser power used on reference
46 savepath = '/home/bjarne/Universitet/Dyes/2P_Results/';
47 multisave = '/home/bjarne/Universitet/Dyes/2P_Results/Spectra/';

```

```

48 loadpath = '/home/bjarne/Universitet/Dyes/2P_fluorometer/';
49 floadpath = '/home/bjarne/Universitet/Dyes/Fluorimeter/2015/';
50
51 % Quantum yield for references
52 refidx = {'PER', 'RB', 'R6G', 'FLU','oldFLU'};
53 Qyref = [0.9;0.7;0.95;0.79;0.79];
54 % Quantum yield for AJ sample series
55 QyAJ = [0.22;0.34;0.37;0.16;0.53;0.0164;0.88;0.17;0.42];
56 AJidx = {'AJ281', 'AJ332', 'AJ345', 'AJ328', 'AJ346', 'AJ341', 'AJ111',
          'AJ116','AJ344'};
57 % Quantum yield for MK sample series
58 QyMK = [0.3;0.57;0.63;0.64;0.48];
59 MKidx = {'MK143','MK145','MK147','MK153','MK154'};
60 % Quantum yield for Abberior Star dyes
61 STidx = {'ST440','ST488'};
62 QyST = [0.82;0.96];
63 % Concatenate QY for all dyes
64 QySidx = [refidx,AJidx,MKidx,STidx];
65 QyS = [Qyref;QyAJ;QyMK;QyST];
66
67 % Import table values for references
68 R = importdata('dyes.ref','\t');
69 Rper = R.data(:,1:2); % Perylene table values
70 Rflu = [R.data(:,1),R.data(:,3)]; % Fluorescein table values
71 Rr6g = [R.data(:,1),R.data(:,4)]; % Rhodamine 6G table values
72 Rrb = [R.data(:,1),R.data(:,5)]; % Rhodamine B table values
73 rFlu = importdata('fluorescein.ref','\t');
74 refvals = [Rper(:,2),Rrb(:,2),Rr6g(:,2),rFlu.data(:,2)];
75
76 % Sample and reference data paameters
77 dilution = '1'; % Range 1—4
78 %intensity = '1'; % 1: unfiltered; 2: Optical density filter 0.1;
79           % 3: OD 0.3; 4: OD 0.5
80 intnmb = 1; % Number of different intensities
81     wllS = zeros(350,length(samples)-1);
82     signalS = zeros(350,length(samples)-1);
83     wllR = zeros(350,length(samples)-1);
84     signalR = zeros(350,length(samples)-1);
85 test = 0;
86 for s = samples;
87     test=test+1;
88     sam = test;
89     if strcmp(s,refname) == 0
90         samplename = samples{sam};
91         for x = 1:intnmb
92             intensity = mat2str(x);
93             for n = 1:wlnum
94                 w = mat2str(exwl(1,n));
95                 name=[loadpath,date,'/',samplegroup,'-',w,'-',intensity,'
                        -',dilution,'-',mat2str(sam),'.txt'];
96                 S = importdata(name,'\t');
97                 scn = max(S(:,3));
98                 pix = length(S)/scn;
99                 dataS(1:scn*pix,1:4)=S(1:scn*pix,1:4);

```

```

100         % Define matrices for wavelengths and signal intensity
101         wLS = dataS(1:pix,1);
102         signalS = dataS(1:pix,4);
103
104         % Insert all datapoints separately into wavelength and
           signal mtrices
105         for m = 1:scn-1
106             wLS = cat(2,wLS,dataS(m*pix+1:(m+1)*pix,1));
107             signalS = cat(2,signalS,dataS(m*pix+1:(m+1)*pix,4));
108         end
109         % Calculate mean values and std. deviation for signal
           data
110         sigm(:,n) = mean(signalS,2);
111         sigstd(:,n) = std(signalS,1,2);
112     end
113     sigmI(:, :, x) = sigm(:, :);
114     sigstdI(:, :, x) = sigstd(:, :);
115 end
116 % Collect mean and std. dev. in IS matrix and create plot of all
           scans
117 IS = [sigmI,sigstdI];
118
119 % Import reference data
120 for x = 1:intnmb
121     intensity = mat2str(x);
122     for n = 1:wlnum
123         w = mat2str(exwl(1,n));
124         name=[loadpath,date,'/',samplegroup,'-',w,'-',intensity,'
           -',dilution,'-',mat2str(ref),' .txt'];
125         S = importdata(name,'\t');
126         dataR(1:scn*pix,1:4)=S(1:scn*pix,1:4);
127         % Define matrices for wavelengths and signal intensity
128         wLR = dataR(1:pix,1);
129         signalR = dataR(1:pix,4);
130
131         % Insert all datapoints separately into wavelength and
           signal matrices
132         for m = 1:scn-1
133             wLR = cat(2,wLR,dataR(m*pix+1:(m+1)*pix,1));
134             signalR = cat(2,signalR,dataR(m*pix+1:(m+1)*pix,4));
135         end
136         % Calculate mean values and std. deviation for signal
           data
137         sigm(:,n) = mean(signalR,2);
138         sigstd(:,n) = std(signalR,1,2);
139     end
140     sigmI(:, :, x) = sigm(:, :);
141     sigstdI(:, :, x) = sigstd(:, :);
142 end
143 % Collect mean and std. dev. in IR matrix and create plot of all
           scans
144 IR = [sigmI,sigstdI];
145
146 % Create a compined plot of sample and reference scans

```

```

147     h = figure(1);
148     for n = 1:wlnum
149         for x = 1:intnmb
150             errorbar(wlR(:,1), IR(:,n,x), IR(:,n+wlnum,x));
151             hold all
152             errorbar(wlS(:,1), IS(:,n,x), IS(:,n+wlnum,x));
153         end
154     end
155     title(['Plot_of_2P_fluorescence_spectra_for_samples_', samplename,
156           '_and_', refname])
157     hold off
158     set(h, 'Units', 'Centimeters');
159     pos = get(h, 'Position');
160     set(h, 'PaperPositionMode', 'Auto', 'PaperUnits', 'Centimeters', '
161           PaperSize', [pos(3), pos(4)]);
162     print(h, [savepath, savedate{sam}, '/', samplename, '-and-', refname, '-
163           spectra.pdf'], '-dpdf');
164
165     % Import 1P fluorescense sample data
166     name=[floadpath, samplename, '-Em.ifx'];
167     oneS = importdata(name, '\t', 25);
168     data1PS = oneS.data(:,1:2);
169     l = 350 - length(data1PS(:,1));
170     prew1S = data1PS(:,1);
171     presignalS = data1PS(:,2);
172     w11S(:,sam) = wextend('l', 'zpd', prew1S, l, 'r');
173     signal1S(:,sam) = wextend('l', 'zpd', presignalS, l, 'r');
174     emS = [w11S, signal1S];
175
176     % Import 1P fluorescence reference data
177     nameR=[floadpath, 'FLU-Em.ifx'];
178     oneR = importdata(nameR, '\t', 25);
179     data1PR(:,1:2) = oneR.data(:,1:2);
180     prew1R = data1PR(:,1);
181     presignalR = data1PR(:,2);
182     L = 350 - length(data1PR);
183     w11R(:,sam) = wextend('l', 'zpd', prew1R, L, 'r');
184     signal1R(:,sam) = wextend('l', 'zpd', presignalR, L, 'r');
185     emR = [w11R, signal1R];
186     %clear data1PS;
187
188     % Find index numbers for the wavelength used to compare data
189     indS(sam) = find(wlS(:,1)>wlC(sam), 1, 'first');
190     indR(sam) = find(wlR(:,1)>wlC(sam), 1, 'first');
191     ind1S(sam) = find(w11S(:,sam)>wlC(sam), 1, 'first');
192     ind1R(sam) = find(w11R(:,sam)>wlC(sam), 1, 'first');
193     int1S(sam) = trapz(w11S((ind1S(sam)-1):(ind1S(sam)+1),sam),
194                       signal1S((ind1S(sam)-1):(ind1S(sam)+1),sam));
195     int1R(sam) = trapz(w11R((ind1R(sam)-1):(ind1R(sam)+1),sam),
196                       signal1R((ind1R(sam)-1):(ind1R(sam)+1),sam));
197
198     for x = 1:intnmb
199         for n = 1:wlnum
    
```

```

195         intS(n, sam, x) = trapz(wlS((indS(sam)-1):(indS(sam)+1),1),
                                IS((indS(sam)-1):(indS(sam)+1),n,x));
196         intR(n, sam, x) = trapz(wlR((indR(sam)-1):(indR(sam)+1),1),
                                IR((indR(sam)-1):(indR(sam)+1),n,x));
197
198         % Integrate over the entire spectrum and calculate the
           % fractional Quantum
199         % Yield of the sample and reference
200         AS(sam) = trapz(signallS(:,sam));
201         AR(sam) = trapz(signallR(:,sam));
202         QySfrac(sam) = int1S(sam)./AS(sam).*QyS(strmatch(
           samplename,QySidx));
203         QyRfrac(sam) = int1R(sam)./AR(sam).*QyS(strmatch(refname,
           QySidx));
204         for r=1:wlnum
205             indx=find(Rflu(:,1)==exwl(r), 1, 'first');
206             refS(r,x)=refvals(indx,strmatch(refname,refidx));
207             %refS(r,x)=rFlu(indx,2);
208         end
209     end
210 end
211 % Find the excitation wavelength table values and the 2PA values
           % associated
212 % with the wavelengths: Rr6g, Rflu, Rrb, Rper
213
214 [CS, ] = concentration(samplename,dilution);
215 [CR, ] = concentration(refname,dilution);
216
217 % Calculate 2PA values for the sample at each exciation
           % wavelength
218 h = figure(2);
219 for x = 1:intnmb
220     for n = 1:wlnum
221         twoPCS(n, sam, x)=(intS(n, sam, x).*CR.*QyRfrac(sam).*refS(n,
           x))./(intR(n, sam, x).*CS.*QySfrac(sam));
222     end
223     plot(exwl',twoPCS(:,sam,x))
224     hold all
225 end
226
227 title(['Plot_of_2PA_Cross-section_for_',samplename])
228 hold off
229 set(h,'Units','Centimeters');
230 pos = get(h,'Position');
231 set(h,'PaperPositionMode','Auto','PaperUnits','Centimeters','
           PaperSize',[pos(3),pos(4)]);
232 print(h,[savepath,savedate{sam},'/',samplename,'-2PA.pdf'],'-dpdf
           ');
233
234 dlmwrite([savepath,savedate{sam},'/',samplename,'-using-',refname
           ,'-2PA-cross-section.csv'],[exwl',twoPCS(:,sam)],'\t');
235 % Calculate 2PA values for the sample at each exciation
           % wavelength
236 for x = 1:intnmb

```

```

237         for n = 1:wlnum
238             twoPCS(n,sam,x)=(intS(n,sam,x).*CR.*QyRfrac(sam).*refS(n,
                x)./(intR(n,sam,x).*CS.*QySfrac(sam)));
239         end
240     end
241     h = figure(3);
242     if intnmb > 1
243         mean2PA = mean(twoPCS,3);
244         plot(exwl,mean2PA(:,sam),'DisplayName',samplename)
245     else
246         plot(exwl,twoPCS(:,sam,x),'DisplayName',samplename)
247     hold all
248     title(['Plot_of_2PA_Cross-sections_from_', savedate{sam}])
249     set(h,'Units','Centimeters');
250     pos = get(h,'Position');
251     set(h,'PaperPositionMode','Auto','PaperUnits','Centimeters','
        PaperSize',[pos(3),pos(4)]);
252     end
253     end
254 end
255 legend('show');
256 print(h,[multisave,date,'/',savedate{sam}],'-2PA.pdf','-dpdf');

```

Script C.7: MATLAB® script for calculating 2PA Cross-Section of dye from 2P fluorescence spectra and known reference values of widely used fluorescent dyes

C.2.3 Combination of Results from Script C.2.2

```

1 clear all
2
3 % Define experiment date, filename, sample and reference names and
  indices
4 %dates = {'131122','131126','131206','131206-1','131209','131210'};
  samples = {'AJ111'};
5 %dates = {'131122','131125','131204','131205','131205-1'}; samples =
  {'AJ116','AJ328'};
6 %dates = {'131206','131206-1','131209','131210'}; samples = {'AJ281
  ','AJ345'};
7 %dates = {'131122','131125','131206','131206-1','131209','131210'};
  samples = {'AJ332'};
8 %dates = {'131122','131204','131205','131205-1'}; samples = {'AJ341
  '};
9 %dates = {'131125','131204','131205','131205-1'}; samples = {'AJ346
  ','MK143'};
10 %dates = {'131121','131126','131202','131203','131203-1'}; samples =
  {'MK145','MK147','MK153','MK154'};
11 %dates =
  {'140123','140123-1','140123-2','140124','140124-1','140129','140129-1','140129-2','140130'};
  samples = {'AJ344'};
12 %dates = {'150116','150123','150124','150124-1'}; samples = {'ST440
  '};
13 dates = {'150116','150123','150124','150124-1'}; samples = {'ST488'};
14
15 z = size(dates);
16 %sample = 5; % Sample index according to well position/samplegroup
17 %samplename = 'AJ341';
18 refname = 'FLU';
19 samplesuffix = ['-using-',refname,'-2PA-cross-section.csv'];
20 showlegend = 1;
21
22 % Define equation variables
23 %powerS = [2.0 2.0 2.0 2 2 2 2]; % Laser power used on sample
24 %powerR = [2.0 2.0 2.0 2 2 2 2]; % Laser power used on reference
25 loadpath = '/home/bjarne/Universitet/Dyes/2P_Results/';
26 savepath = '/home/bjarne/Universitet/Dyes/2P_Results/2PASpectra/';
27
28 colorspecs = distinguishable_colors(33);
29 set(gcf,'DefaultAxesColorOrder',colorspecs);
30 % Sample and reference data parameters
31 %intensity = '1'; % 1: unfiltered; 2: Optical density filter 0.1;
32 % 3: OD 0.3; 4: OD 0.5
33 for sam = 1:length(samples)
34     for n = 1:z(2)
35         name=[loadpath,dates{n},'/',samples{sam},samplesuffix];
36         S = importdata(name,'\t');
37         pix = length(S);
38         dataS(1:pix,1:2)=S(1:pix,1:2);
39         % Define matrices for wavelengths and signal intensity
40         exwl = dataS(:,1);
41         twoPA(:,n) = dataS(:,2);

```

```

42     end
43     results = num2cell(cat(2,exwl,twoPA));
44     header = ['wl',dates];
45     headres = cat(1,header,results);
46     cell2csv([savepath,samples{sam}),'-using-',refname,'-2PA-cross-
           sections.csv'],headres,'\t');
47     % Calculate 2PA values for the sample at each excitation
           wavelength
48     h = figure(1);
49     for x = 1:z(2)
50         plot(exwl,twoPA(:,x),'DisplayName',dates{x})
51         hold all
52     end
53     title(['Plot_of_2PA_Cross-sections_from_', samples{sam}])
54     set(h,'Units','Centimeters');
55     if showlegend == 1
56         legend('show');
57     end
58     pos = get(h,'Position');
59     set(h,'PaperPositionMode','Auto','PaperUnits','Centimeters','
           PaperSize',[pos(3),pos(4)]);
60     print(h,[savepath,samples{sam}),'-2PA.pdf'],'-dpdf');
61     close(1);
62 end

```

Script C.8: MATLAB® script for combining 2PA Cross-Sections for each dye in plots and tables sorted by date and dye name